Operando X-ray Photoelectron Spectroscopic Study on Electrode Reactions of Positive and Negative Electrodes in All-Solid-State Lithium-Ion Batteries during Charge/Discharge Cycles

（充放電過程における全固体リチウムイオン電池の正・負極反応に関するオペランドＸ線光電子分光研究）

Tsukasa Iwama

Graduate School of Chemical Sciences and Engineering

Hokkaido University

2025

Contents

1. Introduction

1.1. General Introduction

1.1.1. Lithium-ion batteries

Lithium-ion batteries (LIBs) commercialized by SONY in 1991 are widely used in a variety of the portable electronic devices, such as laptops and mobile phones.[1] In recent years, their applications have been expanding into larger-scale devices, including electric vehicles (EVs) and stationary energy storages. Further improvements of energy density, power density, and durability are strongly desired for the high-performance next-generation batteries.[2, 3]

LIBs generally consist of an anode, cathode, electrolyte, and separator as shown in Figure 1-1. In commercial LIBs, graphite and lithium cobalt oxide ($LiCoO_2$) are widely used as anode and cathode materials, respectively. During the battery operation, Li^+ ions are shuttled between the anode and cathode via the electrolyte— from the cathode to the anode during charging and in the reverse direction during the discharging of the battery.[4] These electrochemical reactions at the cathode with $LiCoO_2$ and the anode with graphite are as follows:

$$LiCoO_2 \leftrightarrows Li_{1-x}CoO_2 + xLi^+ + xe^- \quad (1)$$

$$6C + xLi^+ + xe^- \rightleftarrows Li_xC_6 \quad (2)$$

The electrolytes require superior chemical, thermal, and electrochemical stability for LIBs with high safety and cyclability, as well as high ionic conductivity for LIBs with high power density.[4-7] In liquid-type LIBs, lithium hexafluorophosphate ($LiPF_6$) dissolved in a mixture of organic solvents, such as polypropylene carbonate (PC) and ethylene carbonate (EC) is widely used as liquid electrolytes.[8] The separator, typically porous polyolefin membranes, provides electrical insulation between the anode and cathode while allows Li^+ ions to transport in the electrolyte phase and through the separator.[4, 9]

Various important physicochemical phenomena are taking place in the cell, such as decomposition of molecules contained in electrolytes,[10, 11] ion transfer at the electrolyte/electrode interfaces and in electrolytes,[12] changes in electrochemical potential of Li^+ ions at the electrolyte/electrode interfaces,[7, 13-15] and changes of crystal structure and electronic state accompanied with redox reactions and Li^+ ion insertion.[16-19] Since those various phenomena significantly affect the cell performance and durability, to dates, tremendous efforts have been dedicated to understanding their mechanism.

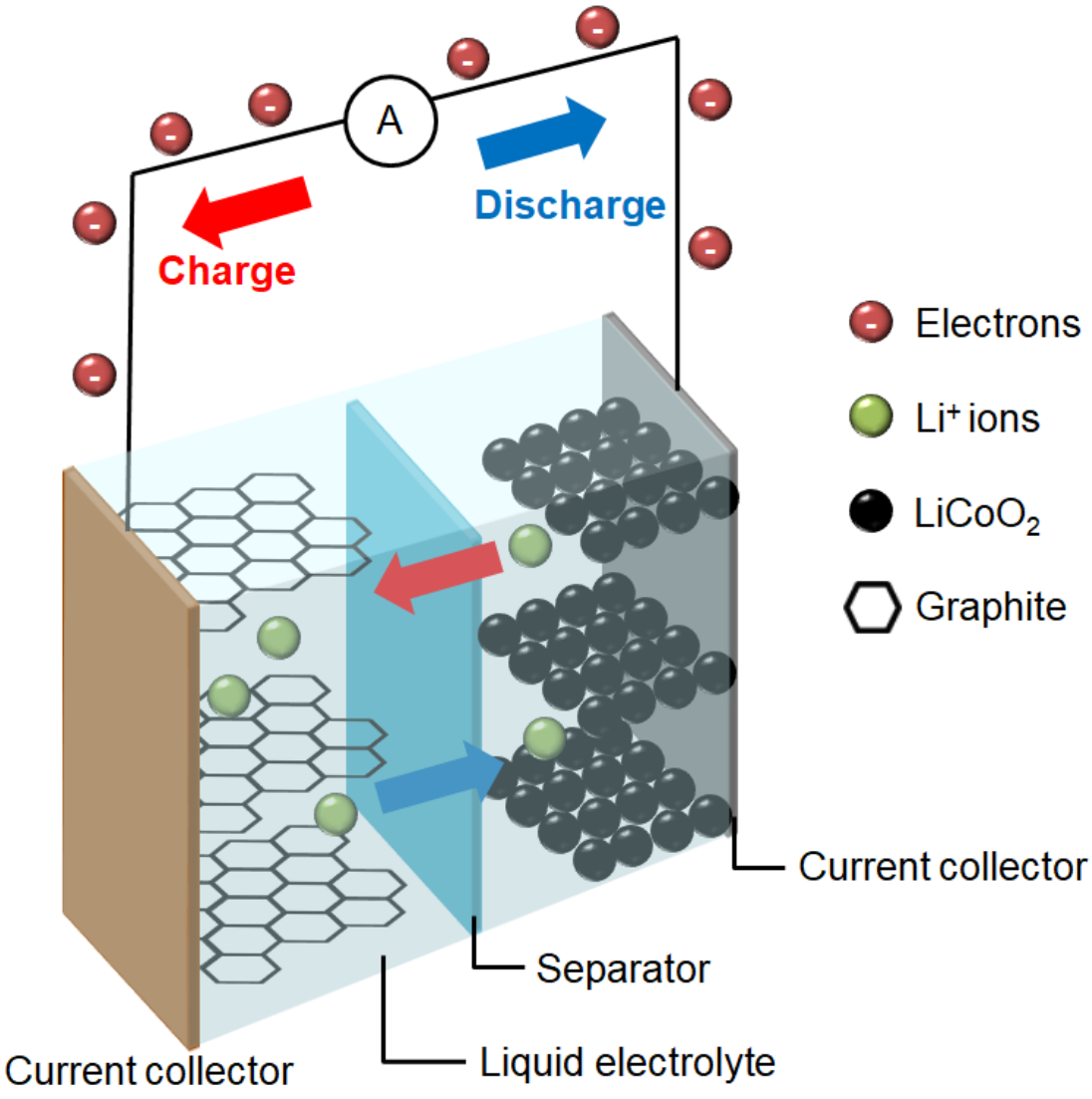

Figure 1-1. A schematic view of liquid-type lithium-ion batteries. Redrawn under Creative Common License CC BY 4.0.[20]

1.1.2. All-solid-state lithium-ion batteries

All-solid-state LIBs (ASSBs) are promising next-generation rechargeable batteries because they ensure safety and reliability by replacing the flammable organic liquid electrolytes used in conventional LIBs with nonflammable inorganic solid electrolytes. In addition, as only Li^+ ions are mobile in the solid electrolytes, undesired side reactions of components in electrolytes can be avoided at the electrode surfaces, leading to the long-lived and high-rate batteries.[21]

A variety of solid electrolytes have been developed to achieve high ionic conductivity that is an essential factor for ASSBs with high-rate performance.[22] There are two types of solid electrolytes; sulfide-based and oxide-based solid electrolytes. Sulfide-based solid electrolytes have relatively high plasticity that allows us to bound with electrode materials by mechanical press at relatively low temperature.[23] Among the sulfide-based solid electrolytes, Li_2S-P_2S_5 glass ceramics[24, 25] and $Li_{10}GeP_2S_{12}$ (LGPS)[26, 27] show ionic conductivity of 10^{-2} S/cm at room temperature, comparable to that of organic liquid electrolyte. Because of those processability and high ionic conductivity, commercialization of sulfide-based ASSBs are expected for electric vehicles in 2028.[28, 29] However, sulfide-based ASSBs still have safety issues because sulfide-based solid electrolytes can react with water in air to produce toxic gases.[30-32]

On the other hand, the oxide-based ASSBs ensure higher safety because oxide-based solid electrolytes are relatively stable under atmosphere. To date, a wide variety of oxide-based solid electrolytes have been developed. In 1976, Hong and Goodenough developed a oxide-based Na^+ ion conductor ($Na_{1+x}Zr_2Si_xP_{3-x}O_{12}$) and named Na^+ super-ionic conductor (NASICON) because of their very high ionic conductivity of 10^{-3} S/cm.[33] Although NASICON-type Li^+-ion conductors such as $LiZr_2(PO_4)_3$, synthesized by substituting Na^+ ions with Li^+ ions show very low Li^+-ion conductivity, $LiTi_2(PO_4)_3$ (LTP) have substantially improved ionic conductivity of 10^{-7} – 10^{-5} S/cm.[34] Furthermore, the ionic conductivity of $Li_{1+x}Ti_{2-x}Al_x(PO_4)_3$ (LATP) synthesized by substituting Ti^{4+} ions of LTP with Al^{3+} ions reaches 7×10^{-4} S/cm.[35]

Perovskite-type oxide-based solid electrolytes ($Li_{3x}La_{2/3-x}TiO_3$ (LLTO)) first developed by Belous et al.[36] and later modified by Inaguma et al.[37] also show relatively high ionic conductivity of 10^{-5} S/cm, especially for the specific composition, $Li_{0.34}La_{0.51}TiO_{2.94}$.

Thangadurai and Weppner developed garnet-type oxide-based solid electrolytes ($Li_7La_3Zr_2O_{12}$ (LLZO)) with very high ionic conductivity of 10^{-4} S/cm.[38, 39] Although it has very high ionic conductivity even in their pioneering work, their ionic conductivity was further improved to 10^{-3} S/cm by substituting Zr^{4+} ions with Ta^{5+} or Nb^{5+} ions or Li^+ ions with Al^{3+} or Ga^{3+} ions.[40-42]

Total ionic conductivity of ASSBs is composed not only of bulk ionic conductivity of each component but also those of grain boundaries and electrode/solid electrolyte interfaces.[34, 43-46] Unlike sulfide-based solid electrolytes that can be joined with electrode materials by mechanical press, co-sintering at high temperatures is a commonly used technique to join the electrode materials and non-plastic oxide-based solid electrolytes and to eliminate the grain boundaries of each material. However, co-sintering often causes undesired side reactions induced by mutual elemental diffusion, resulting in the formation of highly resistive interfacial layers[47-49] and/or complete decomposition of those substances.[50, 51] Thus, improvement of manufacturing process is essential to construct the highly ion conducting electrode/solid electrolyte interfaces.[23 47-49]

ASSBs are divided into two groups: thin-film type and bulk type. In the thin-film type ASSBs, cathode, solid electrolyte and anode thin films are prepared on a substrate by vapor deposition techniques, such as sputtering and pulsed laser deposition (PLD) and thus ideal electrode/solid electrolyte can be prepared without co-sintering that might cause side reactions.[23, 52] Thin-film type ASSBs are basically a subject of fundamental research because very expensive vacuum equipment is required to prepare the cells and mass loading of electrodes are restricted. However, they are expected to be used for microelectronic devices, such as medical devices and sensors, due to its excellent capacity

retention over thousands of cycles.[45, 53]

On the other hand, the bulk-type batteries consist of composite electrodes prepared on solid electrolyte sheet by mechanical press and/or co-sintering process. Bulk-type ASSBs are favorable for large-scale devices, such as electric vehicles (EVs) and stationary energy-storage devices because bulk-type ASSBs with high mass loading are fabricated at reasonable cost.[54]

1.2. Cathodes

$LiCoO_2$ (LCO) is one of the typically used cathode materials in conventional LIBs due to its relatively high theoretical capacity of 274 mAh g^{-1} and superior cycle performance.[55, 56] Its practical capacity is limited to around 140 mAh g^{-1} because of the irreversible structural change.[57]

To date, various types of cathodes, such as $LiNiO_2$ (LNO),[58-60] $LiNi_{0.33}Mn_{0.33}Co_{0.33}O_2$ (NMC),[60, 61] and $LiNi_{0.8}Co_{0.15}Al_{0.05}O_2$ (NCA),[62] $LiMn_2O_4$,[63-65] and $LiFePO_4$ (LFP)[66] have been developed to reduce production cost and/or enhance electrochemical performance of cathodes, such as cycle performance, electrochemical stability, and practical capacity (Figure 1-3).[67]

LNO have a similar theoretical capacity density of 275 mAh g^{-1} to that of LCO and is advantageous for its lower cost compared with those of LCO.[67] However, the challenge

of LNO is synthetic route; Ni^{2+} ions tend to substitute Li^{+} ion , namely cation mixing, due to their similar ionic radii.[58, 68, 69]

$LiMn_2O_4$ also has an advantage of lower cost although its practical capacity is rather small, 120 mAh g^{-1},[63] and capacity fading is also a severe problem especially at elevated temperatures.[65, 70]

NMC and NCA were developed for suppressing cation mixing by substituting Ni^{3+} ions with Co^{3+} and/or Al^{3+} ions,[71] and are currently used as cathodes with high practical capacity density (~200 mAh g^{-1}) for application in EVs.[67, 72]

LFP also has advantages of lower cost and less toxicity, and showed practical capacity of 165 mAh g^{-1}.[66, 67, 73] In addition, LFP has superior thermal stability and cyclability owing to the robust structure of PO_4^{3-}. However, this structural robustness leads to low ionic diffusivity and poor electronic conductivity.[74]

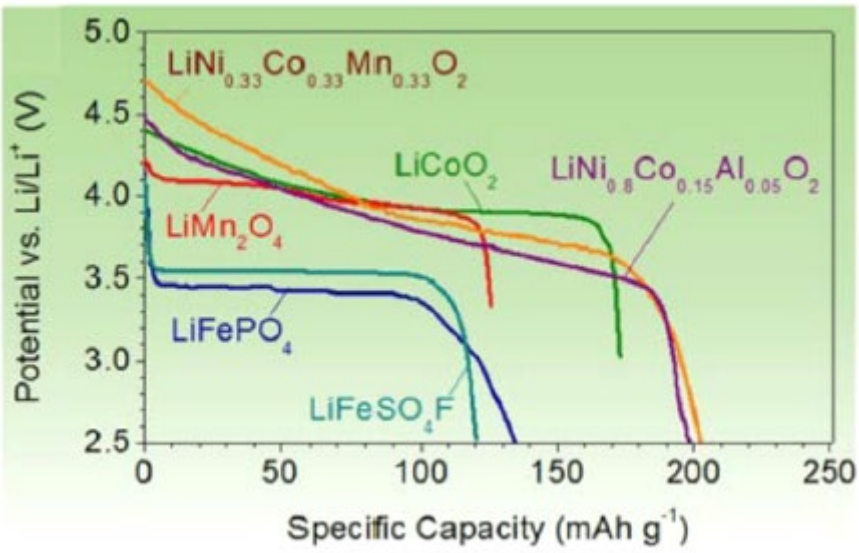

Figure 1-2. Typical discharge profiles of various type of cathodes. Reprinted under Creative Common License CC BY-NC-ND 3.0.[67]

1.2.1. $LiCoO_2$ cathodes

$LiCoO_2$ (LCO) discovered by Prof. John B. Goodenough in 1980 is an intercalation-type cathode.[61] In the course of charging, oxidation of Co^{3+} ions to Co^{4+} ions occurs, simultaneously with the extraction of Li^+ ions into the electrolyte for charge neutralization (see equation (1) in Section 1.1.1).[18] LCO exhibits relatively high theoretical capacity density of 274 mAh g^{-1} under operation in 4.7 – 5.0 V *vs*. Li^+/Li.[55, 56] However, the practical capacity density is limited to around 140 mAh g^{-1} under the operation at 4.2 V or less positive because the high-voltage charging often results in rapid capacity fading due to the irreversible structural change.[57] Tremendous efforts have been devoted to clarify the reaction mechanism[10, 16, 17, 19, 50, 75-92] and optimize the combination of

materials,[7, 11, 12, 93-99] composition of electrolytes,[22, 24, 40-42, 100-102] and design of cells,[96, 103-106] as briefly documented below.

1.2.1.1. Reaction overviews

Co^{3+} ions in the pristine state of LCO are oxidized to Co^{4+} ions accompanied by Li^+ ions extraction under charging (see equation (1) in Section 1.1.1).[18] In contrast, Co^{4+} ions are reduced to Co^{3+} ions under discharging accompanied by Li^+ ions insertion to the LCO. Figure 1-3 (a) and (b) show the galvanostatic charge/discharge potential profiles and corresponding differential capacity plot for a LCO electrode.[107] The potential curve during charging shows three plateau regions, a, b, and c up to 4.2 V where half of Li^+ ions are extracted from the LCO to form $Li_{0.5}CoO_2$. The corresponding crystal structure changes of LCO was shown in Figure 1-4.[17, 108] In the pristine stage, H1 structure where CoO_2 layer and Li layer with edge-shared CoO_6 and LiO_6 octahedra, respectively, pile up alternately along c-axis. In the pristine state of LCO, the five 3d orbitals of Co^{3+} ions split into three low-energy t_{2g} (d_{xy}, d_{yz}, and d_{xz}) and two high-energy e_g ($d_{x^2-y^2}$ and d_{z^2}) orbitals, and e_g orbitals are hybridized with O 2p orbitals to form bonding e_g and antibonding e_{g^*} orbitals. In addition, 4s and 4p orbitals of Co^{3+} ions are hybridized with O 2p orbitals to form bonding a_{1g} a_{1g} and t_{1u} orbitals, and antibonding a_{1g^*} and t_{1u^*} orbitals, according to crystal field theory,[17, 109] as shown in Figure 1-6 (b). Because six

electrons in 3d orbitals of Co^{3+} ions occupy the t_{2g} orbitals to form low-spin state, the bandgap of LCO corresponds to the energy difference between t_{2g} and e_{g^*} of 2.7 eV, as shown in Figure 1-5 (a), indicating semiconducting properties of LCO.[17]

The plateau regions, a, b, and c, correspond to the transformations from H1 to H2 phase where the lattice gradually expands along c-axis due to increase of electrostatic repulsion between CoO_2 layers, from H2 to M1 phase where the lattice continuously expands along c-axis, and eventually has largest c-axis value throughout a series of phase transition of LCO, and from M1 to H3 phase where c-axis length rapidly decreases take place, respectively.[17] The semiconducting properties of LCO change to metallic properties due to the electron delocalization within CoO_2 layers.[17, 110] When the electrode potential of LCO is 4.2 V or less positive including the plateau region a, b, and c, electrons are extracted from t_{2g} states corresponding to valence band maximum (VBM) of LCO, resulting in Co^{3+} ions oxidation to Co^{4+} ions, confirmed by x-ray photoelectron spectroscopy (XPS).[111, 112] On the other hand, O 2p states including hybridized states with Co 3d, 4s, and 4p are almost unchanged, indicating that charge compensation caused by delithiation only involves t_{2g} states in the electrode potential of LCO is 4.2 V or less positive, confirmed by x-ray absorption spectra (XAS)[111] and theoretical calculation using Hartree-Fock model.[113, 114]

Two additional plateaus d and e appear up to 4.7 V where all of Li^+ ions are extracted from the LCO, corresponding to the transformations from H3 to H1-3 phase and from H1-3 to O1 phase as shown in Figure 1-4.[17, 107] H1-3 phase is composed of CoO_2 layers piled up with two kinds of interlayers alternately; one is H3-type with an interlayer distance of 4.8 Å, and the other is O1-type with an interlayer distance of 4.2 Å.[17, 19] While the difference in CoO_2 interlayer distance in the transformation from H1 to H3 phase is less than 2%, that in the transformation from H3 to O1 phase exceeds 10%.[17] Such drastic structural changes cause the electrode capacity fading.[17, 19] Ohnishi et al. attributed the increase of charge-transfer resistance under high-voltage charging to the formation of H1-3 phase by electrochemical impedance spectroscopy (EIS) measurements coupled with *in-situ* x-ray diffraction (XRD).[19] Under the subsequent discharging, although the H1-3 phase disappeared, the resistance did not revert to the original value corresponding to the charge-transfer resistance in the pristine LCO, implying that H1-3 phase impede ionic diffusion to reduce the electrode kinetics of LCO charged at high voltage, and the transformation from H3 to H1-3 phase causes irreversible increase in the electrode resistance and capacity fading.[17] In addition, Jiang et al. confirmed the formation of stripe-defects and the transition from original layered structure to the spinel structure by scanning transmission electron microscopy (STEM) with high angle annular dark field

detection (STEM-HAADF), after the continuous cycling with the cut off voltage of 4.7 V.[85] Thus, under the high-voltage operation, the capacity of LCO rapidly decreases with the number of cycles as shown in Figure 1-6.[19] When the electrode potential of LCO is 4.2 V or more positive, the t_{2g} states cross the top of O 2p bands due to the upshift of O 2p band induced by hybridization between Co 3d states and O 2p band, leading to hole transfer from t_{2g} states to O 2p states. Thus, LCO rapidly degrades due to the oxidation of O^{2-} under the high voltage operation.[111]

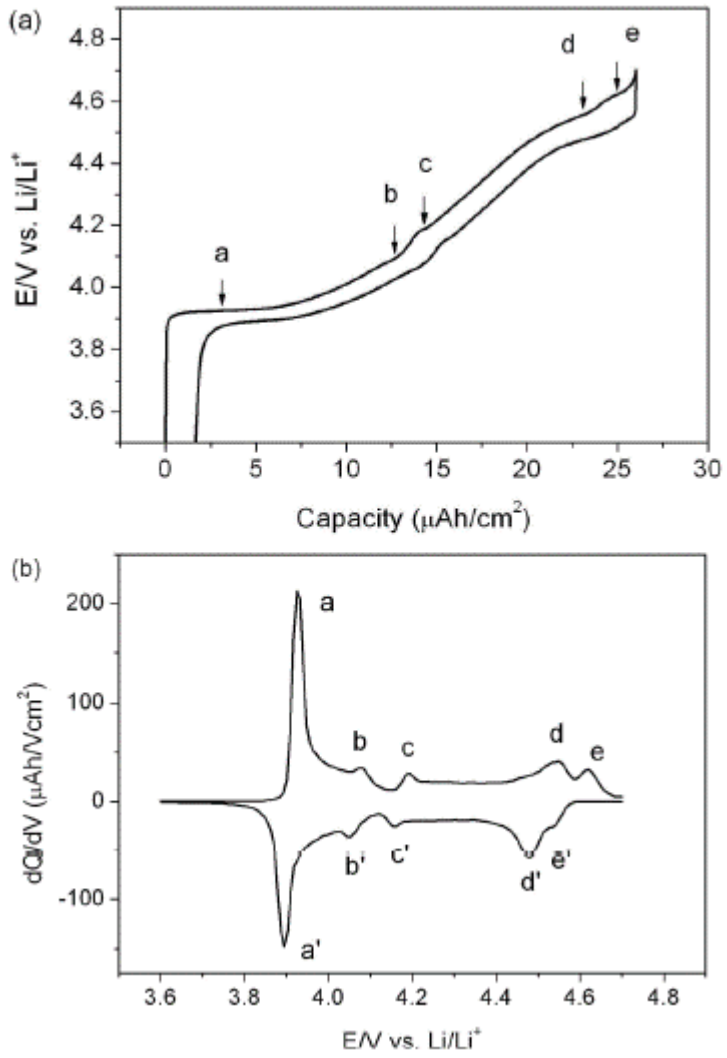

Figure 1-3. (a) Potential profiles of a thin-film $LiCoO_2$ using $LiCoO_2$/Li cell. (b) Corresponding differential capacity (d*Q*/d*V*) curves in a potential range of 3.0 – 4.7 V. (The electrolyte is a solution of 1 M $LiPF_6$ dissolved in EC/DEC 1:2 (by weight).) Reprinted from Reference.[107] Copyright © The Korean Physical Society.

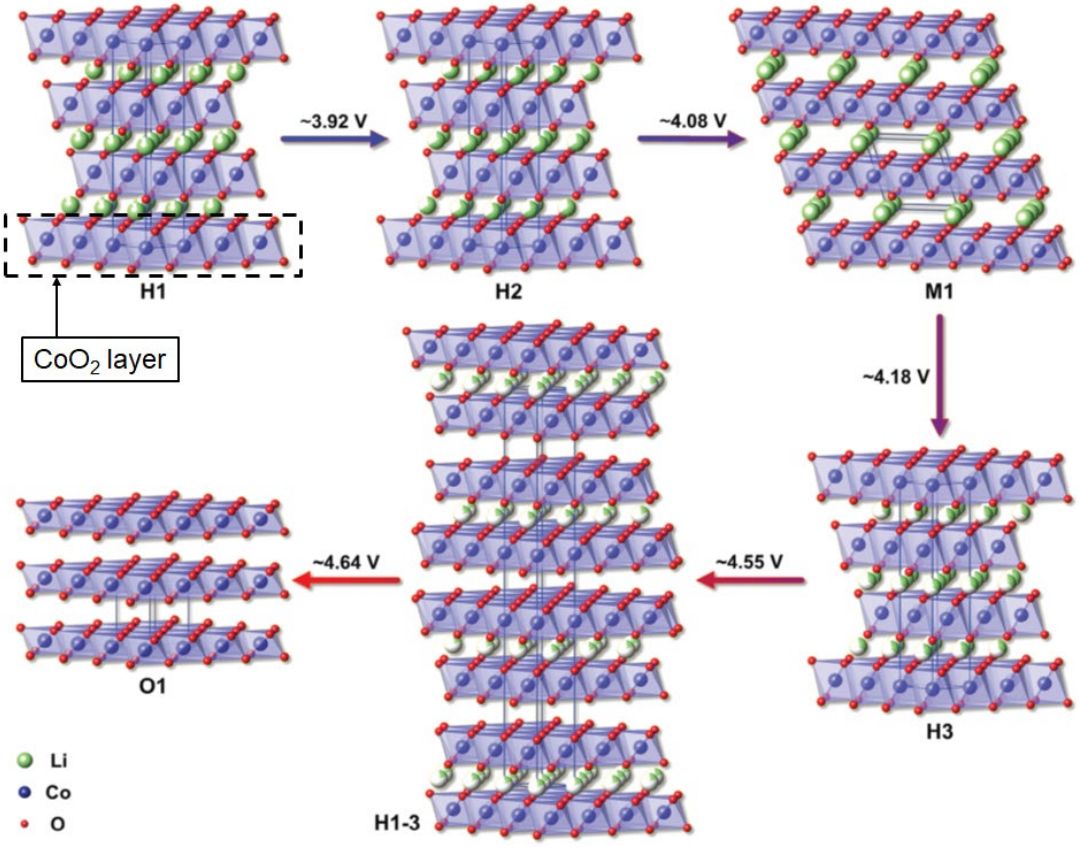

Figure 1-4. Schematic illustrations of a series of transformations of LCO during charging process. Reproduced and modified with permission from © 2023 Wiley-VCH GmbH.[17]

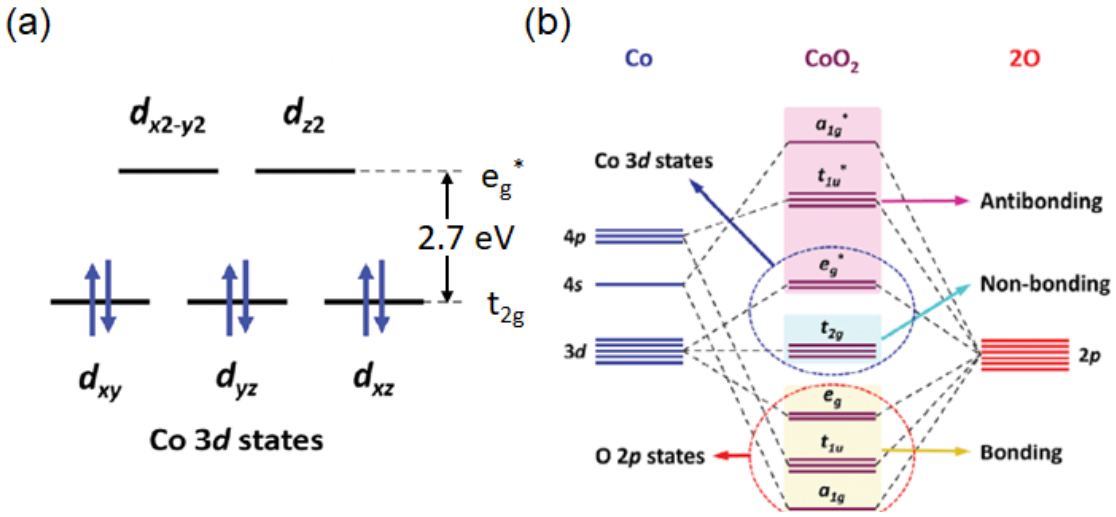

Figure 1-5. (a) Schematic electronic configuration of Co^{3+} 3d states. Molecular orbital diagram for CoO_2 in an octahedral environment. Reproduced and modified with permission from © 2023 Wiley‐VCH GmbH.[17]

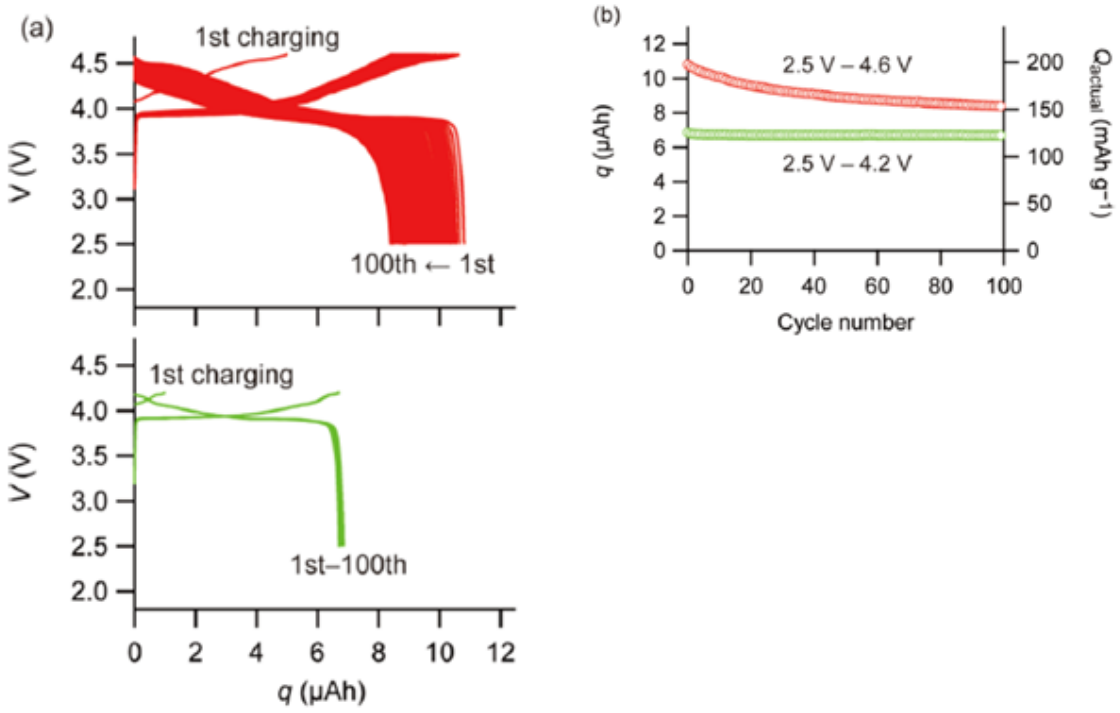

Figure 1-6. Cycling performance. (a) Charge/discharge curves of the LCO thin-film batteries in a potential range from 2.5 – 4.2 V (green) and 4.6 V (red). (b) The discharge capacities (q) plotted against the cycle number. The observed capacities in the left vertical axis are converted to specific capacities based on the actual mass for the electrode reactions (Q_{actual}) on the right vertical axis. Reprinted under Creative Common License CC-BY 4.0.[19]

1.3. Anodes

Graphite is one of the most widely used anode materials in conventional liquid-type LIBs. The theoretical capacity density of a graphite anode is estimated to be around 372 mAh g^{-1} according to the equation (2) shown in Section 1.1.1.[115, 116] Li^+ ions are reductively inserted into the interlayer of graphite to form Li_xC_6 during charging, while Li^+ ions are oxidatively extracted from Li_xC_6 during discharging. Due to its very negative redox potential close to that of deposition/dissolution of lithium (~ 0.1 V vs. Li^+/Li), very large operation voltage ~4 V can be achieved in combination with typical cathodes such as LCO.[115, 116]

In the initial cycles, Li salts, organic solvents and other additives contained in electrolyte solutions are reductively decomposed at the anode surface because of its very negative potential, to form a solid electrolyte interphase (SEI). SEI has Li^+-ion conductivity and electronic resistivity that allow Li^+ ions to access the surface of electrode materials in anode with preventing continuous decomposition of electrolyte solutions.[117]

Recently, Li-alloy-based anode materials, such as P (2596 mAh g^{-1}), Sn (960 mAh g^{-1}), Ge (1570 mAh g^{-1}), Si (4200 mAh g^{-1}) have also been subjects of research because of their extremely high theoretical capacity density toward the high-performance next-generation batteries (Figure 1-7).[118]

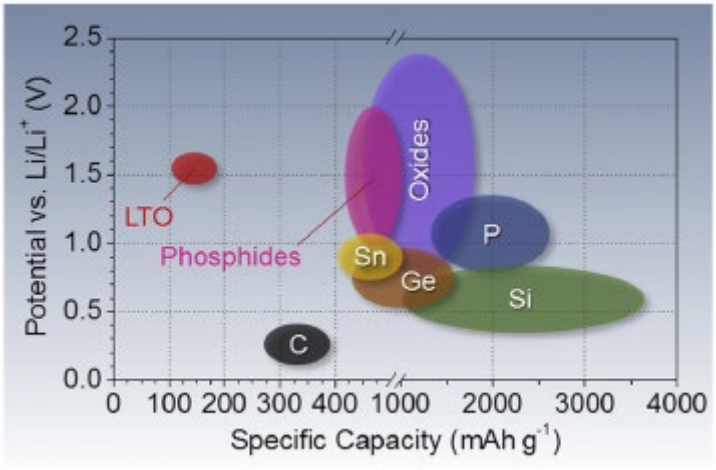

Figure 1-7. Approximate range of average discharge potentials and specific capacity of various intercalation-type and Li-alloy-based anodes. Reprinted under Creative Common License CC BY-NC-ND 3.0.[67]

1.3.1. Si anodes

Research related with Si as a Li-alloy-based anode material was started by San-Cheng Lai,[119] Ram A. Sharma,[120] and Randall N. Seefurth[121] in 1970s. In the course of lithiation, amorphous lithium silicide (Li_xSi) forms due to the lithiation of amorphous Si (a-Si) and transforms to the crystalline phases such as $Li_{12}Si_7$, Li_7Si_{13}, $Li_{13}Si_4$ coexisting with amorphous Li_xSi. Eventually, crystalline $Li_{22}Si_5$ ($Li_{4.4}Si$) forms at a theoretical capacity of 4200 mAh g^{-1} at ~400°C,[122] while the crystalline $Li_{15}Si_4$ (c-$Li_{3.75}Si$) is the final product at a theoretical capacity density of 3579 mAh g^{-1} at room temperature according to the following equation.[123, 124]

$$Si + xLi^+ + xe^- \rightleftarrows Li_xSi \quad (3)$$

The redox potential for the litiation/delithiation of Si is very negative, ~0.35 V vs. Li^+/Li. Although it is slightly more positive than that of graphite, still very high operation voltage ~3.9 V can be achieved in combination with typical cathodes such as LCO. However, Si undergoes considerable (~300%) volume expansion/contraction initiated by crystal structure changes during electrochemical cycles, which causes pulverization of Si particles and other irreversible structural changes, leading to rapid capacity fading.[21, 67, 125] Thus, understanding and controlling those physicochemical events are the biggest challenge for the effective use of Si in LIBs.

SEIs also form at the surface of Si due to the decomposition of electrolyte solutions.[126] However, the SEIs on the Si surface can be mechanically damaged by considerable volume changes during the charge/discharge cycles, and new SEIs form at the exposed Si surfaces. Such continuous formation/decomposition of SEIs causes consumption of electrolyte solutions, formation of excessively thick and resistive SEI and capacity fade.[67]

1.3.1.1. Reaction overviews

In the initial stage of lithiation, lithiation of Si occurs to form Li_xSi. Then, reversible lithiation and delithiation of Li_xSi occur (see equation (3) in section 1.3.1). Figure 1-8 shows representative example of galvanostatic lithiation/delithiation dQ/dV curves for a-Si in a-Si/Li half-cell in a potential range of 0.005 to 1.0 V.[91, 127] It is noted that, in this

figure, a lithium foil is used as a counter electrode for the half cell. In the initial stage of lithiation, the electrode potential steeply drops from 1.0 to 0.3 V and a broad doublet peak appears at around 0.24 – 0.29 V. Li insertion into a-Si gradually proceeds while breaking down the Si matrix, and then a-Si transforms into $Li_{2.0}Si$ (a-$Li_{2.0}Si$) at around 0.24 – 0.29 V where small Si clusters composed of dimer, trimer, and isolated Si exist.[128-132] Then, a dQ/dV peak appears at approximately 0.09 V, corresponding to further lithiation of a-$Li_{2.0}Si$. According to the charge integration, amorphous $Li_{3.5}Si$ (a-$Li_{3.5}Si$) where most of Si exist as isolated Si, forms at the end of this peak.[132] Only in the first lithiation cycle,[128, 131] a dQ/dV peak appears at 0.05 V. This peak was attributed to the crystallization of a-$Li_{3.5}Si$ to c-$Li_{3.75}Si$ where all Si exist as isolated Si, by XRD,[133, 134] electron diffraction (ED),[121, 135, 136] and nuclear magnetic resonance (NMR).[137, 138]

In the subsequent delithiation, a dQ/dV peak appears at 0.25 V where delithiation from a-$Li_{3.5}Si$ preferentially occur up to the composition of a-$Li_{2.0}Si$. A sharp intense peak and broad peak appear at around 0.5 V. Broad one is assignable to the delithiation from a-Li_xSi ($x < 2.0$), and the other to the amorphization of c-$Li_{3.75}Si$.[128] The sharp intense peak and broad peak correspond to the delithiation of c-$Li_{3.75}Si$ and a-$Li_{2.0}Si$ to form a-Li_xSi ($x < 2.0$), respectively.[138, 139] In addition, the sharp intense peak was only observed in the first delithiation, as is the case of the first lithiation.

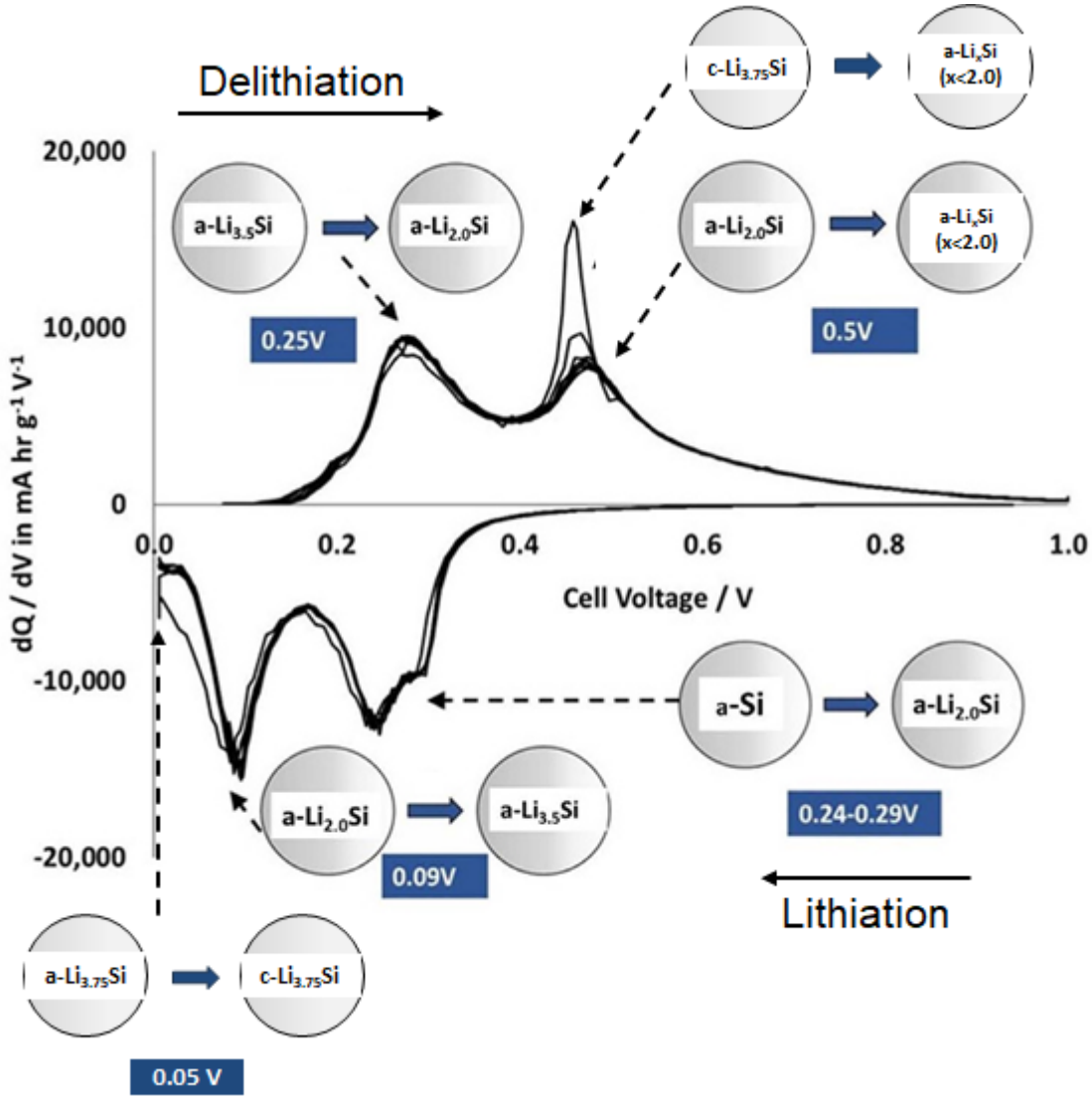

Figure 1-8. Differential capacity (d*Q*/d*V*) curves for a-Si/Li half-cell in the two to ten cycles and the potential range of 0.005 – 1.0 V. (The electrolyte used was EC/EMC (3:7), with 15 wt % FEC and 3 wt % VC.) Reproduced and modified under Creative Commons.[128]

1.3.2. SiO_x anodes

Silicon oxide (SiO_x) has been attracting wide attention because it has cycle performance superior to pure Si, at the sacrifice of intrinsic capacity density of pure Si.[140] SiO_x-based anodes exhibit very large irreversible capacity loss in the first cycle due to the Li consumption by formation of electrochemically inactive species such as Li_2O and Li silicates ($Li_2Si_2O_5$, $Li_6Si_2O_7$, and Li_4SiO_4).[140-143] These inactive species are considered to contribute to the improvement of cycle performance by acting as buffer layers of the volume changes.[140, 141, 144, 145]

The relationship of oxygen content x in SiO_x and cycle performance was systematically investigated by Haruta et al using SiO_x thin-film anodes in liquid electrolytes.[141] Figure 1-9 (a) and (b) show discharge capacity and Coulombic efficiency with respect to the cycle number for SiO_x (x = 0.02, 0.21, 0.48, 1.09, and 1.78).[141] Initial capacity density clearly depends on oxygen content x in SiO_x; it is almost constant, ~80 μAh cm^{-2} for oxygen-poor SiO_x thin films in the range of oxygen content x = 0.02 – 0.48. When oxygen-rich SiO_x thin films with the oxygen content x = 1.09 and 1.78 were used, however, capacity density decreased up to 60 and 40 μAh cm^{-2}, respectively. Thus, higher oxygen content in SiO_x brings about smaller capacity density. There is a trade-off between initial capacity and capacity retention. Although the initial capacities of oxygen-rich SiO_x thin

films are smaller, their capacity retention is much higher for $SiO_{1.78}$, $SiO_{1.09}$, and other oxygen-poor SiO_x (x = 0.02, 0.21 and 0.48) in that order.

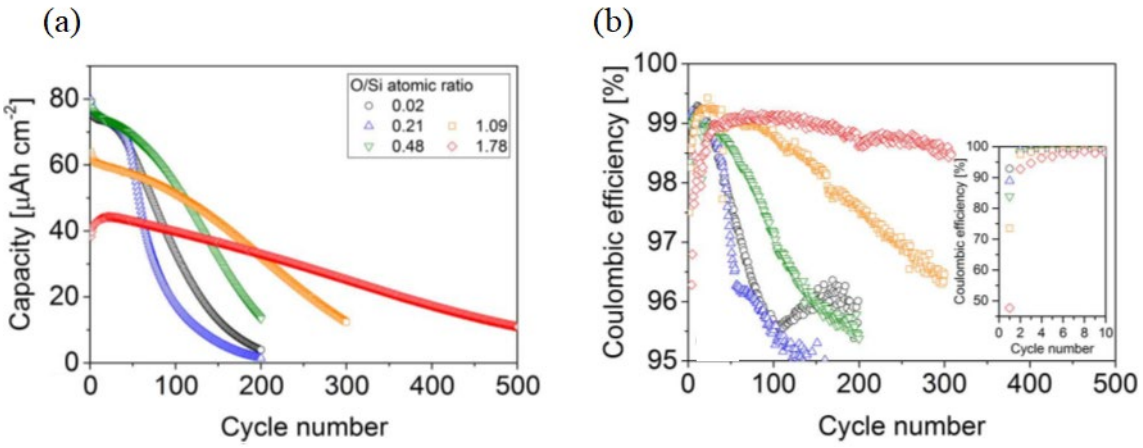

Figure 1-9. (a) Discharge capacity and (b) Coulombic efficiency of SiO_x thin films with different oxygen contents. (The electrolyte is a solution of 1 M $LiPF_6$ dissolved in EC/DEC 3:7 (by volume). Reprinted with permission from © 2019 The Electrochemical Society.[141]

In the liquid-type LIBs, SEIs also form at the surface of SiO_x anode.[140] However, the volume change can be effectively suppressed for oxygen-rich SiO_x (x >1) as compared with oxygen-poor SiO_x and pure Si, leading to improve of capacity retention.[141]

Miyazaki et al. also investigated the effects of introducing oxygen into a-Si thin films on their cycle performance and reversible capacities using ASSB configurations.[140] Oxygen-poor a-$SiO_{0.4}$ thin-film exhibited reversible capacity more than 2800 mAh g^{-1} and low capacity fading rate of 0.06% during the first 100 cycles (Figure 1-10).[140] One of

the reasons for the excellent cycle performance is that successive growth of SEIs is effectively suppressed using solid electrolytes in contrast to using liquid electrolytes because of the wide electrochemical potential window of solid electrolytes. Thus, the introduction of smaller amount of oxygen into a-Si thin film is sufficient for ASSB with excellent cycle performance.[140]

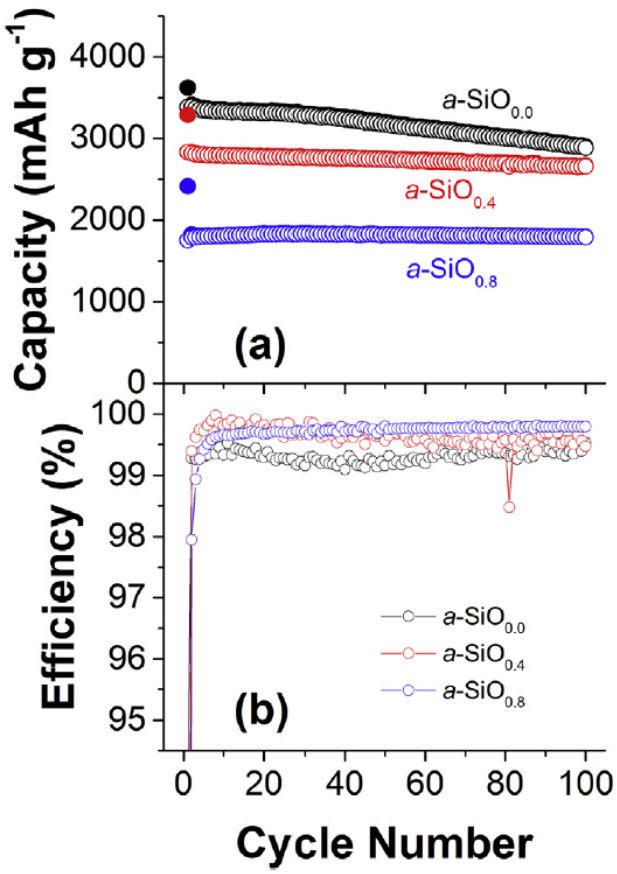

Figure 1-10. Cycle performances of 300-nm-thick a-$SiO_{0.0}$ (black), a-$SiO_{0.4}$ (red), and a-$SiO_{0.8}$ (blue) thin films at a current density of 0.1 mA cm^{-2}: (a) Charging and discharging capacities and (b) coulombic efficiencies as a function of cycle number. The filled circles in (a) indicate the charging capacities, and the open circles in the panel indicate the discharging capacities. Reprinted with permission from © 2016 Elsevier B.V. All rights reserved.[140]

1.3.2.1. Reaction overviews

Figure 1-11 shows galvanostatic lithiation/delithiation potential profiles in the first cycle and cyclic voltammograms (CVs) in the first and second cycles for amorphous SiO_x (a-SiO_x) thin film with different oxygen contents (x = 0.02, 0.21, 0.48, 1.09, and 1.78) in a-SiO_x/Li half-cell in a potential range of 0.02 to 1.0 V, respectively.[141] CVs provide information similar to dQ/dV curves as can be seen from the equation (4):[146]

$$\frac{I}{\frac{dV}{dt}} = \frac{\frac{d(It)}{dt}}{\frac{dV}{dt}} = \frac{\frac{dQ}{dt}}{\frac{dV}{dt}} = \frac{dQ}{dV} \quad (4)$$

where I is current and dV/dt is a sweep rate.

In the first lithiation, except for $SiO_{1.78}$, all the SiO_x (x = 0.02, 0.21, 0.48, and 1.08) show two peaks at ~0.07 V and ~0.24 V in their CVs. Similar peaks are observed at 0.09 V and around 0.24 – 0.29 V for amorphous Si as shown in Figure 1-8, attributed to the formation of a-$Li_{3.5}Si$ from a-$Li_{2.0}Si$ and a-$Li_{2.0}Si$ from a-$Li_{x<2.0}Si$, respectively. These peaks are observed in the second cycles, suggesting the originating phenomena are reversible. In addition, these electrochemical responses are most pronounced for the one with smallest oxygen content, $SiO_{0.02}$. Thus, it is considered that those SiO_x with relatively small oxygen contents undergoes the formation of a-$Li_{3.5}Si$ via the a-$Li_{2.0}Si$ and its phase transformation. In contrast, $SiO_{1.78}$ shows only a broad peak at around 0.07 V probably due to its very high electronic/ionic resistivity. $SiO_{0.21}$, $SiO_{0.48}$, and $SiO_{1.09}$ show

additional sharp peak at around 0.4 – 0.6 V. These peaks disappear in the second lithiation cycle, suggesting that the peaks are due to the formation of irreversible species such as lithium silicates ($Li_2Si_2O_5$, Li_2SiO_3, and Li_4SiO_4) and Li_2O.

In the first and second delithiation, all the SiO_x show two anodic peaks at ~0.46 V and ~0.27 V. The features are reversible and similar to those of pure Si electrode shown in Figure 1-8, suggesting the occurrence of delithiation from a-$Li_{3.5}Si$ to a-$Li_{2.0}Si$ and a-$Li_{2.0}Si$ to a-$Li_{x<2.0}Si$. It is noted that the features of $SiO_{1.78}$ are somewhat smaller and distorted, implying that larger amount of Li^+ ions were consumed to form Li_4SiO_4 and Li_2O in comparison with other SiO_x ($SiO_{0.02,}$ $SiO_{0.21}$, $SiO_{0.48,}$ and $SiO_{1.09}$) affects the incompletion of lithiation because of its high ionic/electronic resistivity. lithium silicates should be although cathodic peaks corresponding to the formation of irreversible species are not observed in the CVs due to high ionic/electronic resistivity of $SiO_{1.78}$

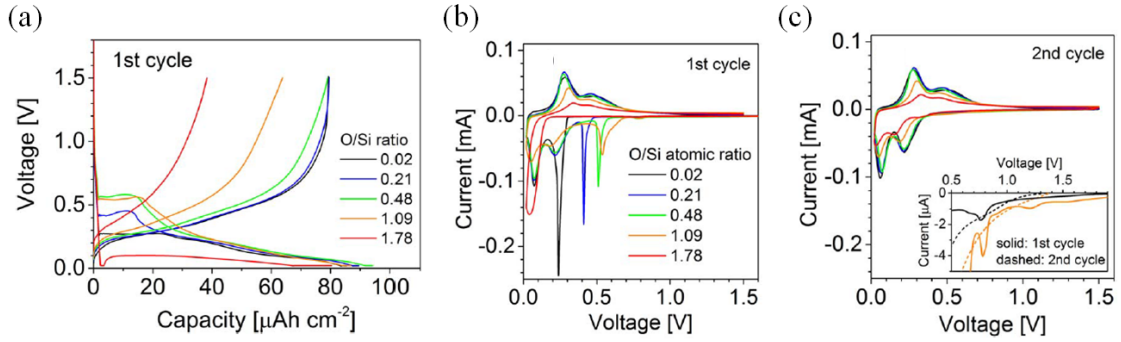

Figure 1-11. (a) Charge and discharge curves in the first cycle for SiO_x thin films of different oxygen contents (x = 0.02, 0.21, 0.48, 1.09 and 1.78) in 1 M $LiPF_6$/EC+DEC. Cyclic voltammograms of SiO_x films of different oxygen contents in (b) the first and (c) the second cycles (The electrolyte is a solution of 1 M $LiPF_6$ dissolved in EC/DEC 3:7 (by volume). Inset of (c) shows a magnification of the potential range of 0.5 to 1.9 V. Reprinted with permission from © 2019 The Electrochemical Society.[141]

1.4. Objective and outline

The objective of this thesis is to elucidate the electrochemical reactions of $LiCoO_2$ (LCO) cathodes under high-voltage operations and origin of superior cycle performance of SiO_x anodes in an all-solid-state lithium-ion battery configuration. Electrochemical reactions of LCO and SiO_x were systematically investigated from elemental composition, oxidation states of the electrodes during lithiation/delithiation processes.

Although LCO has superior theoretical capacity density and cycle performance among cathode materials, expanding operating voltage induces the irreversible structural changes,

as mentioned in Section 1.2.1.1.[17, 19, 85] Understanding the electrochemical reactions including such undesired irreversible processes is essential for improving the achievable capacity density and developing new high-capacity materials.

As mentioned in Section 1.3.2, although reversible capacity and capacity retention are a trade-off, one can optimize the SiO_x composition and obtain the guideline for designing long-lived and high-capacity cells through the clarification of lithiation/delithiation mechanisms.[140]

In conventional liquid-type LIB configuration, various important physicochemical phenomena are taking place in the cell, such as decomposition of molecules contained in electrolytes, ion transfer at the electrolyte/electrode interfaces and in electrolytes occur. In ASSB configuration, however, the decomposition of electrolyte solutions and formation of SEI can be avoided. In addition, electrochemical reactions can be driven in UHV, and powerful surface analysis techniques can be applied without any special spectroelectrochemical cells. Therefore, both the LCO cathode and SiO_x anode were deposited on a garnet-type oxide-based solid electrolytes, $Li_{6.6}La_3Zr_{1.6}Ta_{0.4}O_{12}$ (LLZT), in ASSBs configurations.

An operando hard x-ray photoelectron spectroscopy (HAXPES) apparatus enabling angle-resolved measurements under bias applications without disassembling the batteries

and exposing them to air was developed using a laboratory-based HAXPES apparatus equipped with a Cr-Kα source to analyze the fundamental properties of electrodes during charge/discharge cycles.

This thesis is composed of seven chapters as follows.

Chapter 2. Experimental

The experimental details such as preparation of all-solid-state test cells composed of either LCO or amorphous SiO_x/$Li_{6.6}La_3Zr_{1.6}Ta_{0.4}O_{12}$ (LLZT)/Li metal configurations and the characterization techniques used in the present study are described

Chapter 3. Instrumentation

A laboratory-based HAXPES apparatus equipped with a Cr-Kα source enabling bias-application to a sample and angle-resolved measurements was developed. Then, those functions were demonstrated using reference samples. We denote this measurement system as *operando* HAXPES system.

Chapter 4. Electrochemical Reactions of $LiCoO_2$-Li_3BO_3 Composite Cathodes

First, the electrode reactions of a $LiCoO_2$-Li_3BO_3/LLZT/Li-configurated $LiCoO_2$ and Li_3BO_3 under charge/discharge cycles in a potential range of 3.0 – 4.2 V were observed using *operando* HAXPES system as a demonstration using an all-solid-state cell. Then, the electrode reactions of $LiCoO_2$ under charge/discharge cycles with different voltage

range were investigated. Irreversible oxidation of Co^{3+} ions and O^{2-} anions of $LiCoO_2$ under high-voltage operations caused capacity fading.

Chapter 5. Static and dynamic analysis of lithiation/delithiation of amorphous-SiO*x* thin-film anodes

The continuous lithiation/delithiation of the amorphous-SiO_x thin-film electrode on the LLZT solid electrolyte were investigated using *in-situ* XPS previously developed in our laboratory.[125, 147, 148] The lithiation/delithiation mechanisms of SiO_x anodes and the role of electrochemically inactive species such as Li_2O and Li silicates formed as a result of Li insertion to SiO_x were discussed.

Finally, the present results and the overall thesis are summarized in **Chapter 6.**

References

(1) Sekai, K.; Azuma, H.; Omaru, A.; Fujita, S.; Imoto, H.; Endo, T.; Yamamura, K.; Nishi, Y. Lithium-ion rechargeable cells with $LiCoO_2$ and carbon electrodes. *J. Power Sources* **1993**, *43-44*, 241-244. DOI: 10.1016/0378-7753(93)80120-E.

(2) Moslehi, K.; Kumar, R. A Reliability Perspective of the Smart Grid. *IEEE Transactions on Smart Grid* **2010**, *1* (1), 57-64. DOI: 10.1109/tsg.2010.2046346.

(3) Tuballa, M. L.; Abundo, M. L. A review of the development of Smart Grid technologies. *Renewable and Sustainable Energy Reviews* **2016**, *59*, 710-725. DOI: 10.1016/j.rser.2016.01.011.

(4) Huang, X. Separator technologies for lithium-ion batteries. *J. Solid State Electrochem.* **2010**, *15* (4), 649-662. DOI: 10.1007/s10008-010-1264-9.

(5) Yamada, Y.; Usui, K.; Chiang, C. H.; Kikuchi, K.; Furukawa, K.; Yamada, A. General observation of lithium intercalation into graphite in ethylene-carbonate-free superconcentrated electrolytes. *ACS Appl Mater Interfaces* **2014**, *6* (14), 10892-10899. DOI: 10.1021/am5001163 From NLM PubMed-not-MEDLINE.

(6) Wiemers-Meyer, S.; Jeremias, S.; Winter, M.; Nowak, S. Influence of Battery Cell Components and Water on the Thermal and Chemical Stability of LiPF6 Based Lithium Ion Battery Electrolytes. *Electrochim. Acta* **2016**, *222*, 1267-1271. DOI: 10.1016/j.electacta.2016.11.100.

(7) Zhu, Y.; He, X.; Mo, Y. Origin of Outstanding Stability in the Lithium Solid Electrolyte Materials: Insights from Thermodynamic Analyses Based on First-Principles Calculations. *ACS Appl Mater Interfaces* **2015**, *7* (42), 23685-23693. DOI: 10.1021/acsami.5b07517.

(8) Li, M.; Lu, J.; Chen, Z.; Amine, K. 30 Years of Lithium-Ion Batteries. *Adv. Mater.*

2018, e1800561. DOI: 10.1002/adma.201800561 From NLM Publisher.

(9) Francis, C. F. J.; Kyratzis, I. L.; Best, A. S. Lithium-Ion Battery Separators for Ionic-Liquid Electrolytes: A Review. *Adv. Mater.* **2020**, *32* (18), e1904205. DOI: 10.1002/adma.201904205 From NLM PubMed-not-MEDLINE.

(10) Zhuang, Z.; Wang, J.; Jia, K.; Ji, G.; Ma, J.; Han, Z.; Piao, Z.; Gao, R.; Ji, H.; Zhong, X.; et al. Ultrahigh-Voltage $LiCoO_2$ at 4.7 V by Interface Stabilization and Band Structure Modification. *Adv. Mater.* **2023**, *35* (22), e2212059. DOI: 10.1002/adma.202212059 From NLM PubMed-not-MEDLINE.

(11) Ihrig, M.; Finsterbusch, M.; Laptev, A. M.; Tu, C. H.; Tran, N. T. T.; Lin, C. A.; Kuo, L. Y.; Ye, R.; Sohn, Y. J.; Kaghazchi, P.; et al. Study of $LiCoO_2$/$Li_7La_3Zr_2O_{12}$:Ta Interface Degradation in All-Solid-State Lithium Batteries. *ACS Appl Mater Interfaces* **2022**, *14* (9), 11288-11299. DOI: 10.1021/acsami.1c22246 From NLM PubMed-not-MEDLINE.

(12) Wei, C.; Yu, C.; Chen, S.; Chen, S.; Peng, L.; Wu, Y.; Li, S.; Cheng, S.; Xie, J. Unraveling the $LiNbO_3$ coating layer on battery performances of lithium argyrodite-based all-solid-state batteries under different cut-off voltages. *Electrochim. Acta* **2023**, *438*. DOI: 10.1016/j.electacta.2022.141545.

(13) Nomura, Y.; Yamamoto, K.; Hirayama, T.; Ouchi, S.; Igaki, E.; Saitoh, K. Direct Observation of a Li-Ionic Space-Charge Layer Formed at an Electrode/Solid-Electrolyte Interface. *Angew. Chem. Int. Ed. Engl.* **2019**, *58* (16), 5292-5296. DOI: 10.1002/anie.201814669 From NLM PubMed-not-MEDLINE.

(14) Yamamoto, K.; Iriyama, Y.; Asaka, T.; Hirayama, T.; Fujita, H.; Fisher, C. A.; Nonaka, K.; Sugita, Y.; Ogumi, Z. Dynamic visualization of the electric potential in an all-solid-state rechargeable lithium battery. *Angew. Chem. Int. Ed. Engl.*

2010, *49* (26), 4414-4417. DOI: 10.1002/anie.200907319 From NLM PubMed-not-MEDLINE.

(15) Hausbrand, R.; Becker, D.; Jaegermann, W. A surface science approach to cathode/electrolyte interfaces in Li-ion batteries: Contact properties, charge transfer and reactions. *Prog. Solid State Chem.* **2014**, *42* (4), 175-183. DOI: 10.1016/j.progsolidstchem.2014.04.010.

(16) Seong, W. M.; Yoon, K.; Lee, M. H.; Jung, S. K.; Kang, K. Unveiling the Intrinsic Cycle Reversibility of a $LiCoO_2$ Electrode at 4.8-V Cutoff Voltage through Subtractive Surface Modification for Lithium-Ion Batteries. *Nano Lett.* **2019**, *19* (1), 29-37. DOI: 10.1021/acs.nanolett.8b02902 From NLM PubMed-not-MEDLINE.

(17) Lin, C.; Li, J.; Yin, Z. W.; Huang, W.; Zhao, Q.; Weng, Q.; Liu, Q.; Sun, J.; Chen, G.; Pan, F. Structural Understanding for High-Voltage Stabilization of Lithium Cobalt Oxide. *Adv. Mater.* **2023**, e2307404. DOI: 10.1002/adma.202307404 From NLM Publisher.

(18) Ohzuku, T.; Ueda, A. Solid-State Redox Reactions of $LiCoO_2$ (R3m) for 4 Volt Secondary Lithium Cells. *J. Electrochem. Soc.* **1994**, *141*, 2972.

(19) Ohnishi, T.; Mitsuishi, K.; Takada, K. In Situ X-ray Diffraction of $LiCoO_2$ in Thin-Film Batteries under High-Voltage Charging. *ACS Applied Energy Materials* **2021**, *4* (12), 14372-14379. DOI: 10.1021/acsaem.1c03046.

(20) Or, T.; Gourley, S. W. D.; Kaliyappan, K.; Yu, A.; Chen, Z. Recycling of mixed cathode lithium‐ion batteries for electric vehicles: Current status and future outlook. *Carbon Energy* **2020**, *2* (1), 6-43. DOI: 10.1002/cey2.29.

(21) Cervera, R. B.; Suzuki, N.; Ohnishi, T.; Osada, M.; Mitsuishi, K.; Kambara, T.;

Takada, K. High performance silicon-based anodes in solid-state lithium batteries. *Energy Environ. Sci.* **2014**, *7* (2), 662-666. DOI: 10.1039/c3ee43306d.

(22) Wang, Y.; Richards, W. D.; Ong, S. P.; Miara, L. J.; Kim, J. C.; Mo, Y.; Ceder, G. Design principles for solid-state lithium superionic conductors. *Nat Mater* **2015**, *14* (10), 1026-1031. DOI: 10.1038/nmat4369 From NLM PubMed-not-MEDLINE.

(23) Baek, S.-W.; Lee, J.-M.; Kim, T. Y.; Song, M.-S.; Park, Y. Garnet related lithium ion conductor processed by spark plasma sintering for all solid state batteries. *J. Power Sources* **2014**, *249*, 197-206. DOI: 10.1016/j.jpowsour.2013.10.089.

(24) Seino, Y.; Ota, T.; Takada, K.; Hayashi, A.; Tatsumisago, M. A sulphide lithium super ion conductor is superior to liquid ion conductors for use in rechargeable batteries. *Energy Environ. Sci.* **2014**, *7* (2), 627-631. DOI: 10.1039/c3ee41655k.

(25) Yamane, H.; Shibata, M.; Shimane, Y.; Junke, T.; Seino, Y.; Adams, S.; Minami, K.; Hayashi, A.; Tatsumisago, M. Crystal structure of a superionic conductor, $Li_7P_3S_{11}$. *Solid State Ionics* **2007**, *178* (15-18), 1163-1167. DOI: 10.1016/j.ssi.2007.05.020.

(26) Kamaya, N.; Homma, K.; Yamakawa, Y.; Hirayama, M.; Kanno, R.; Yonemura, M.; Kamiyama, T.; Kato, Y.; Hama, S.; Kawamoto, K.; et al. A lithium superionic conductor. *Nature Materials* **2011**, *10* (9), 682-686. DOI: 10.1038/nmat3066.

(27) Kuhn, A.; Duppel, V.; Lotsch, B. V. Tetragonal $Li_{10}GeP_2S_{12}$ and Li_7GePS_8 – exploring the Li ion dynamics in LGPS Li electrolytes. *Energy & Environmental Science* **2013**, *6* (12). DOI: 10.1039/c3ee41728j.

(28) *全固体量産へ出光・トヨタがタッグ　「実現力」で狙う世界標準*. 2023. https://toyotatimes.jp/toyota_news/1046.html?padid=ag478_from_newsroom (accessed 2024 6/26).

(29) *出光とトヨタ、バッテリーEV用全固体電池の量産実現に向けた協業を開始*. 2023. https://global.toyota/jp/newsroom/corporate/39898897.html (accessed 2024 6/26).

(30) Muramatsu, H.; Hayashi, A.; Ohtomo, T.; Hama, S.; Tatsumisago, M. Structural change of Li_2S–P_2S_5 sulfide solid electrolytes in the atmosphere. *Solid State Ionics* **2011**, *182* (1), 116-119. DOI: 10.1016/j.ssi.2010.10.013.

(31) Sahu, G.; Lin, Z.; Li, J.; Liu, Z.; Dudney, N.; Liang, C. Air-stable, high-conduction solid electrolytes of arsenic-substituted Li4SnS4. *Energy Environ. Sci.* **2014**, *7* (3), 1053-1058. DOI: 10.1039/c3ee43357a.

(32) Kondo, S.; Takada, K.; Yamamura, Y. New lithium ion conductors based on Li_2S-SiS_2 system. *Solid State Ionics* **1992**, *53-56*, 1183-1186. DOI: 10.1016/0167-2738(92)90310-L.

(33) Goodenough, J. B.; Hong, H. Y.-P.; Kafalas, J. A. FAST Na^+ - ION TRANSPORT IN SKELETON STRUCTURES. *Mater. Res. Bull.* **1976**, *11* (2). DOI: 10.1016/0025-5408(76)90077-5.

(34) Ren, Y.; Chen, K.; Chen, R.; Liu, T.; Zhang, Y.; Nan, C. W.; Vyas, B. Oxide Electrolytes for Lithium Batteries. *J. Am. Ceram. Soc.* **2015**, *98* (12), 3603-3623. DOI: 10.1111/jace.13844.

(35) Aono, H.; Sugimoto, E.; Sadaoka, Y.; Imanaka, N.; Adachi, G.-y. Ionic Conductivity of Solid Electrolytes Based on Lithium Titanium Phosphate. *J. Electrochem. Soc.* **1990**, *137*, 1023. DOI: 10.1149/1.2086597.

(36) Belous, A. G.; Novitskaya, G. N.; Polyanetskaya, S. V.; Y. I. Gornikov. Study of Complex Oxides with the Composition $La_{2/3-x}Li_{3x}TiO_3$. *Inorg. Mater.* **1987**, *23*,

412.

(37) Inaguma, Y.; Liquan, C.; Itoh, M.; Nakamura, T.; Uchida, T.; Ikuta, H.; Wakihara, M. HIGH IONIC CONDUCTIVITY IN LITHIUM LANTHANUM TITANATE. *Solid State Commun.* **1993**, *86*, 689-693. DOI: 10.1016/0038-1098(93)90841-A.

(38) Thangadurai, V.; Kaack, H.; Weppner, W. J. F. Novel Fast Lithium Ion Conduction in Garnet‐Type $Li_5La_3M_2O_{12}$ (M = Nb, Ta). *J. Am. Ceram. Soc.* **2004**, *86* (3), 437-440. DOI: 10.1111/j.1151-2916.2003.tb03318.x.

(39) Murugan, R.; Thangadurai, V.; Weppner, W. Fast Lithium Ion Conduction in Garnet-Type Li7La3Zr2O12. *Angew. Chem. Int. Ed.* **2007**, *46* (41), 7778-7781. DOI: 10.1002/anie.200701144.

(40) Hayashi, N.; Watanabe, K.; Ohnishi, T.; Takada, K.; Shimanoe, K. Impact of intentional composition tuning on the sintering properties of Ca–Bi co-doped $Li_7La_3Zr_2O_{12}$ for co-fired solid-state batteries. *Journal of Materials Chemistry A* **2023**, *11* (29), 15681-15690. DOI: 10.1039/d3ta00921a.

(41) Thangadurai, V.; Narayanan, S.; Pinzaru, D. Garnet-type solid-state fast Li ion conductors for Li batteries: critical review. *Chem. Soc. Rev.* **2014**, *43* (13), 4714-4727. DOI: 10.1039/c4cs00020j From NLM PubMed-not-MEDLINE.

(42) Wu, J. F.; Pang, W. K.; Peterson, V. K.; Wei, L.; Guo, X. Garnet-Type Fast Li-Ion Conductors with High Ionic Conductivities for All-Solid-State Batteries. *ACS Appl Mater Interfaces* **2017**, *9* (14), 12461-12468. DOI: 10.1021/acsami.7b00614 From NLM PubMed-not-MEDLINE.

(43) Deng, Y.; Shang, S.-J.; Mei, A.; Lin, Y.-H.; Liu, L.-Y.; Nan, C.-W. The preparation and conductivity properties of $Li_{0.5}La_{0.5}TiO_3$/inactive second phase composites. *J. Alloys Compd.* **2009**, *472* (1-2), 456-460. DOI: 10.1016/j.jallcom.2008.04.085.

(44) Inaguma, Y.; Nakashima, M. A rechargeable lithium–air battery using a lithium ion-conducting lanthanum lithium titanate ceramics as an electrolyte separator. *J. Power Sources* **2013**, *228*, 250-255. DOI: 10.1016/j.jpowsour.2012.11.098.

(45) Sakuda, A.; Hayashi, A.; Ohtomo, T.; Hama, S.; Tatsumisago, M. Bulk-Type All-Solid-State Lithium Secondary Battery with Li_2S-P_2S_5 Thin-Film Separator. *Electrochemistry* **2012**, *80* (10), 839-841. DOI: 10.5796/electrochemistry.80.839.

(46) Gockeln, M.; Glenneberg, J.; Busse, M.; Pokhrel, S.; Mädler, L.; Kun, R. Flame aerosol deposited $Li_4Ti_5O_{12}$ layers for flexible, thin film all-solid-state Li-ion batteries. *Nano Energy* **2018**, *49*, 564-573. DOI: 10.1016/j.nanoen.2018.05.007.

(47) Hikima, K.; Suzuki, K.; Taminato, S.; Hirayama, M.; Yasuno, S.; Kanno, R. Thin Film All-solid-state Battery Using Li_2MnO_3 Epitaxial Film Electrode. *Chem. Lett.* **2019**, *48* (3), 192-195. DOI: 10.1246/cl.180773.

(48) Kim, K. H.; Iriyama, Y.; Yamamoto, K.; Kumazaki, S.; Asaka, T.; Tanabe, K.; Fisher, C. A. J.; Hirayama, T.; Murugan, R.; Ogumi, Z. Characterization of the interface between $LiCoO_2$ and $Li_7La_3Zr_2O_{12}$ in an all-solid-state rechargeable lithium battery. *J. Power Sources* **2011**, *196* (2), 764-767. DOI: 10.1016/j.jpowsour.2010.07.073.

(49) Woo, J. H.; Trevey, J. E.; Cavanagh, A. S.; Choi, Y. S.; Kim, S. C.; George, S. M.; Oh, K. H.; Lee, S.-H. Nanoscale Interface Modification of $LiCoO_2$ by Al_2O_3 Atomic Layer Deposition for Solid-State Li Batteries. *J. Electrochem. Soc.* **2012**, *159* (7), A1120-A1124. DOI: 10.1149/2.085207jes.

(50) Ichihara, F.; Miyoshi, S.; Masuda, T. Co-sintering process of LiCoO(2) cathodes and NASICON-type LATP solid electrolytes studied by X-ray diffraction and X-ray absorption near edge structure. *Phys. Chem. Chem. Phys.* **2022**, *24* (42), 25878-

25884. DOI: 10.1039/d2cp01020h From NLM PubMed-not-MEDLINE.

(51) Ichihara, F.; Niitsu, K.; Tanaka, Y.; Niwa, Y.; Mitsuishi, K.; Miyoshi, S.; Ohno, T.; Masuda, T. Structural Analysis of the $LiCoPO_4$ Electrode/NASICON-Type $Li_{1.3}Al_{0.3}Ti_{1.7}(PO_4)_3$ Solid Electrolyte Interface. *The Journal of Physical Chemistry C* **2023**, *127* (31), 15043-15050. DOI: 10.1021/acs.jpcc.3c02132.

(52) Bates, J. B.; Dudney, N. J.; Lubben, D. C.; Gruzalski, G. R.; Kwak, B. S.; Yu, X.; Zuhr, R. A. Thin-film rechargeable lithium batteries. *J. Power Sources* **1995**, *54*, 58-62.

(53) Chen, R. J.; Zhang, Y. B.; Liu, T.; Xu, B. Q.; Lin, Y. H.; Nan, C. W.; Shen, Y. Addressing the Interface Issues in All-Solid-State Bulk-Type Lithium Ion Battery via an All-Composite Approach. *ACS Appl Mater Interfaces* **2017**, *9* (11), 9654-9661. DOI: 10.1021/acsami.6b16304 From NLM PubMed-not-MEDLINE.

(54) Thackeray, M. M.; Wolverton, C.; Isaacs, E. D. Electrical energy storage for transportation—approaching the limits of, and going beyond, lithium-ion batteries. *Energy & Environmental Science* **2012**, *5* (7). DOI: 10.1039/c2ee21892e.

(55) Godshall, N. A.; Raistrick, I. D.; Huggins, R. A. THERMODYNAMIC INVESTIGATIONS OF TERNARY LITHIUM-TRANSITION METAL-OXYGEN CATHODE MATERIALS. *Mater. Res. Bull.* **1980**, *15*, 561-570. DOI: 10.1016/0025-5408(80)90135-X.

(56) Lyu, Y.; Wu, X.; Wang, K.; Feng, Z.; Cheng, T.; Liu, Y.; Wang, M.; Chen, R.; Xu, L.; Zhou, J.; et al. An Overview on the Advances of $LiCoO_2$ Cathodes for Lithium‐Ion Batteries. *Advanced Energy Materials* **2020**, *11* (2). DOI: 10.1002/aenm.202000982.

(57) Whittingham, M. S. Lithium Batteries and Cathode Materials. *Chem. Rev.* **2004**,

104, 4271-4301. DOI: 10.1021/cr020731c.

(58) Yuwono, R. A.; Wang, F.-M.; Wu, N.-L.; Chen, Y.-C.; Chen, H.; Chen, J.-M.; Haw, S.-C.; Lee, J.-F.; Xie, R.-K.; Sheu, H.-S.; et al. Evaluation of $LiNiO_2$ with minimal cation mixing as a cathode for Li-ion batteries. *Chem. Eng. J.* **2023**, *456*. DOI: 10.1016/j.cej.2022.141065.

(59) Montoro, L. A.; Abbate, M.; Almeida, E. C.; Rosolen, J. M. Electronic structure of the transition metal ions in $LiCoO_2$ $LiNiO_2$ and $LiCo_{0.5}Ni_{0.5}O_2$. *Chem. Phys. Lett.* **1999**, *309*, 14-18. DOI: 10.1016/S0009-2614(99)00650-8.

(60) Ohzuku, T.; Ueda, A.; Nagayama, M. Electrochemistry and Structural Chemistry of $LiNiO_2$ (R3m) for 4 Volt Secondary Lithium Cells. *J. Electrochem. Soc.* **1993**, *140*, 1862. DOI: 10.1149/1.2220730.

(61) Mizushima, K.; Jones, P. C.; Wiseman, P. J.; Goodenough, J. B. Li_xCoO_2 ($0<x\leq1$): A NEW CATHODE MATERIAL FOR BATTERIES OF HIGH ENERGY DENSITY. *Mater. Res. Bull.* **1980**, *15*, 783-789. DOI: 10.1016/0025-5408(80)90012-4.

(62) Chen, C. H.; Liu, J.; Stoll, M. E.; Henriksen, G.; Vissers, D. R.; Amine, K. Aluminum-doped lithium nickel cobalt oxide electrodes for high-power lithium-ion batteries. *J. Power Sources* **2004**, *128* (2), 278-285. DOI: 10.1016/j.jpowsour.2003.10.009.

(63) Thackeray, M. M. Structural Considerations of Layered and Spinel Lithiated Oxides for Lithium Ion Batteries. *J. Electrochem. Soc.* **1995**, *142*, 2558. DOI: 10.1149/1.2050053.

(64) Thackeray, M. M.; Shao-Horn, Y.; Kahaian, A. J.; Kepler, K. D.; Skinner, E.; Vaughey, J. T.; Hackney, S. A. Structural Fatigue in Spinel Electrodes in High

Voltage (4 V) Li/$Li_xMn_2O_4$ Cells. *Electrochem. Solid-State Lett.* **1998**, *1*, 7. DOI: 10.1149/1.1390617.

(65) Inamoto, J.; Fukutsuka, T.; Miyazaki, K.; Abe, T. Electrochemical Surface Analysis of $LiMn_2O_4$ Thin-film Electrodes in $LiPF_6$/Propylene Carbonate at Room and Elevated Temperatures. *Electrochemistry* **2021**, *89* (1), 19-24. DOI: 10.5796/electrochemistry.20-00112.

(66) Padhi, A. K.; Nanjundaswamy, K. S.; Goodenough, J. B. Phospho‐olivines as Positive‐Electrode Materials for Rechargeable Lithium Batteries. *J. Electrochem. Soc.* **1997**, *144*, 1188. DOI: 10.1149/1.1837571.

(67) Nitta, N.; Wu, F.; Lee, J. T.; Yushin, G. Li-ion battery materials: present and future. *Mater. Today* **2015**, *18* (5), 252-264. DOI: 10.1016/j.mattod.2014.10.040.

(68) Morales, J.; Pérez-Vicente, C.; Tirado, J. L. CATION DISTRIBUTION AND CHEMICAL DEINTERCALATION OF $Li_{1-x}Ni_{1+x}O_2$. *Mater. Res. Bull.* **1990**, *25* (5), 623-630. DOI: 10.1016/0025-5408(90)90028-Z.

(69) Rougier, A.; Gravereau, P.; Delmas, C. Optimization of the Composition of the $Li_{1-z}Ni_{1+z}O_2$ Electrode Materials: Structural, Magnetic, and Electrochemical Studies. *J. Electrochem. Soc.* **1996**, *143*, 1168. DOI: 10.1149/1.1836614.

(70) Lee, M. J.; Lee, S.; Oh, P.; Kim, Y.; Cho, J. High performance $LiMn_2O_4$ cathode materials grown with epitaxial layered nanostructure for Li-ion batteries. *Nano Lett.* **2014**, *14* (2), 993-999. DOI: 10.1021/nl404430e From NLM PubMed-not-MEDLINE.

(71) Yu, Z.; Qu, X.; Wan, T.; Dou, A.; Zhou, Y.; Peng, X.; Su, M.; Liu, Y.; Chu, D. Synthesis and Mechanism of High Structural Stability of Nickel-Rich Cathode

Materials by Adjusting Li-Excess. *ACS Appl Mater Interfaces* **2020**, *12* (36), 40393-40403. DOI: 10.1021/acsami.0c12541 From NLM PubMed-not-MEDLINE.

(72) Kotal, M.; Jakhar, S.; Roy, S.; Sharma, H. K. Cathode materials for rechargeable lithium batteries: Recent progress and future prospects. *Journal of Energy Storage* **2022**, *47*. DOI: 10.1016/j.est.2021.103534.

(73) Wang, Y.; He, P.; Zhou, H. Olivine $LiFePO_4$: development and future. *Energy Environ. Sci.* **2011**, *4* (3), 805-817. DOI: 10.1039/c0ee00176g.

(74) Zhang, W.-J. Structure and performance of $LiFePO_4$ cathode materials: A review. *J. Power Sources* **2011**, *196* (6), 2962-2970. DOI: 10.1016/j.jpowsour.2010.11.113.

(75) Salagre, E.; Segovia, P.; Gonzalez-Barrio, M. A.; Jugovac, M.; Moras, P.; Pis, I.; Bondino, F.; Pearson, J.; Wang, R. S.; Takeuchi, I.; et al. Physical Delithiation of Epitaxial $LiCoO_2$ Battery Cathodes as a Platform for Surface Electronic Structure Investigation. *ACS Appl Mater Interfaces* **2023**, *15* (30), 36224-36232. DOI: 10.1021/acsami.3c06147 From NLM PubMed-not-MEDLINE.

(76) Li, Z.; Yi, H.; Ding, W.; Ren, H.; Du, Y.; Shang, M.; Zhao, W.; Chen, H.; Zhou, L.; Lin, H.; et al. Revealing the Accelerated Capacity Decay of a High‐Voltage $LiCoO_2$ upon Harsh Charging Procedure. *Adv. Funct. Mater.* **2023**. DOI: 10.1002/adfm.202312837.

(77) Zhang, J.-C.; Liu, Z.-D.; Zeng, C.-H.; Luo, J.-W.; Deng, Y.-D.; Cui, X.-Y.; Chen, Y.-N. High-voltage $LiCoO_2$ cathodes for high-energy-density lithium-ion battery. *Rare Metals* **2022**, *41* (12), 3946-3956. DOI: 10.1007/s12598-022-02070-6.

(78) Wu, Q.; Zhang, B.; Lu, Y. Progress and perspective of high-voltage lithium cobalt oxide in lithium-ion batteries. *Journal of Energy Chemistry* **2022**, *74*, 283-308.

DOI: 10.1016/j.jechem.2022.07.007.

(79) Qin, N.; Gan, Q.; Zhuang, Z.; Wang, Y.; Li, Y.; Li, Z.; Hussain, I.; Zeng, C.; Liu, G.; Bai, Y.; et al. Hierarchical Doping Engineering with Active/Inert Dual Elements Stabilizes $LiCoO_2$ to 4.6 V. *Advanced Energy Materials* **2022**, *12* (31). DOI: 10.1002/aenm.202201549.

(80) Yang, J. H.; Kim, H.; Ceder, G. Insights into Layered Oxide Cathodes for Rechargeable Batteries. *Molecules* **2021**, *26* (11). DOI: 10.3390/molecules26113173 From NLM PubMed-not-MEDLINE.

(81) Papp, J. K.; Li, N.; Kaufman, L. A.; Naylor, A. J.; Younesi, R.; Tong, W.; McCloskey, B. D. A comparison of high voltage outgassing of $LiCoO_2$, $LiNiO_2$, and Li_2MnO_3 layered Li-ion cathode materials. *Electrochim. Acta* **2021**, *368*. DOI: 10.1016/j.electacta.2020.137505.

(82) Kong, W.; Zhang, J.; Wong, D.; Yang, W.; Yang, J.; Schulz, C.; Liu, X. Tailoring Co3d and O2p Band Centers to Inhibit Oxygen Escape for Stable 4.6 V $LiCoO_2$ Cathodes. *Angew. Chem. Int. Ed. Engl.* **2021**, *60* (52), 27102-27112. DOI: 10.1002/anie.202112508 From NLM PubMed-not-MEDLINE.

(83) Hu, E.; Li, Q.; Wang, X.; Meng, F.; Liu, J.; Zhang, J.-N.; Page, K.; Xu, W.; Gu, L.; Xiao, R.; et al. Oxygen-redox reactions in LiCoO2 cathode without O–O bonding during charge-discharge. *Joule* **2021**, *5* (3), 720-736. DOI: 10.1016/j.joule.2021.01.006.

(84) Swift, M. W.; Qi, Y. First-Principles Prediction of Potentials and Space-Charge Layers in All-Solid-State Batteries. *Phys. Rev. Lett.* **2019**, *122* (16), 167701. DOI: 10.1103/PhysRevLett.122.167701 From NLM PubMed-not-MEDLINE.

(85) Jiang, Y. Y.; Qin, C. D.; Yan, P. F.; Sui, M. L. Origins of capacity and voltage

fading of $LiCoO_2$ upon high voltage cycling. *Journal of Materials Chemistry A* **2019**, *7* (36), 20824-20831. DOI: 10.1039/c9ta06579b.

(86) Long, X.-H.; Wu, Y.-R.; Zhang, N.; Yu, P.-F.; Feng, X.-F.; Zheng, S.; Fu, J.-M.; Liu, X.-S.; Liu, N.; Wang, M.; et al. Charge compensation and capacity fading in $LiCoO_2$ at high voltage investigated by soft x-ray absorption spectroscopy. *Chinese Physics B* **2018**, *27* (10). DOI: 10.1088/1674-1056/27/10/107802.

(87) Yano, A.; Shikano, M.; Ueda, A.; Sakaebe, H.; Ogumi, Z. $LiCoO_2$ Degradation Behavior in the High-Voltage Phase Transition Region and Improved Reversibility with Surface Coating. *J. Electrochem. Soc.* **2016**, *164* (1), A6116-A6122. DOI: 10.1149/2.0181701jes.

(88) Xia, H.; Lu, L.; Meng, Y. S.; Ceder, G. Phase Transitions and High-Voltage Electrochemical Behavior of $LiCoO_2$ Thin Films Grown by Pulsed Laser Deposition. *J. Electrochem. Soc.* **2007**, *154*, A337-A342. DOI: 10.1149/1.2509021.

(89) Chen, Z. H.; Dahn, J. R. Methods to obtain excellent capacity retention in $LiCoO_2$ cycled to 4.5 V. *Electrochim. Acta* **2004**, *49* (7), 1079-1090. DOI: 10.1016/j.electacta.2003.10.019.

(90) Reimers, J. N.; Dahn, J. R. Electrochemical and In Situ X-Ray Diffraction Studies of Lithium Intercalation in Li_xCoO_2. *J. Electrochem. Soc.* **1992**, *139*, 2091. DOI: 10.1149/1.2221184.

(91) Mellin, M.; Cherkashinin, G.; Mohseni, E.; Phillips, R.; Jaegermann, W.; Hofmann, J. P. Voltage-dependent charge compensation mechanism and cathode electrolyte interface stability of the lithium-ion battery cathode materials $LiCoO_2$ and $LiNi_{1/3}Mn_{1/3}Co_{1/3}O_2$ studied by photoelectron spectroscopy. *Journal of Materials Chemistry A* **2024**, *12* (6), 3644-3658. DOI: 10.1039/d3ta05981b.

(92) Tateyama, Y.; Gao, B.; Jalem, R.; Haruyama, J. Theoretical picture of positive electrode–solid electrolyte interface in all-solid-state battery from electrochemistry and semiconductor physics viewpoints. *Current Opinion in Electrochemistry* **2019**, *17*, 149-157. DOI: 10.1016/j.coelec.2019.06.003.

(93) Wang, C.; Li, S.; Chen, W.; Zhao, Y.; Xu, S.; Dou, H.; Zhang, X. The improvement of the high voltage performance of $LiCoO_2$ by coating $LiTaO_3$ via magnetron sputtering. *CrystEngComm* **2023**, *25* (46), 6496-6502. DOI: 10.1039/d3ce00873h.

(94) Sastre, J.; Chen, X.; Aribia, A.; Tiwari, A. N.; Romanyuk, Y. E. Fast Charge Transfer across the $Li_7La_3Zr_2O_{12}$ Solid Electrolyte/$LiCoO_2$ Cathode Interface Enabled by an Interphase-Engineered All-Thin-Film Architecture. *ACS Appl Mater Interfaces* **2020**, *12* (32), 36196-36207. DOI: 10.1021/acsami.0c09777 From NLM PubMed-not-MEDLINE.

(95) Tsai, C.-L.; Ma, Q.; Dellen, C.; Lobe, S.; Vondahlen, F.; Windmüller, A.; Grüner, D.; Zheng, H.; Uhlenbruck, S.; Finsterbusch, M.; et al. A garnet structure-based all-solid-state Li battery without interface modification: resolving incompatibility issues on positive electrodes. *Sustainable Energy & Fuels* **2019**, *3* (1), 280-291. DOI: 10.1039/c8se00436f.

(96) Shoji, M.; Munakata, H.; Kanamura, K. Fabrication of All-Solid-State Lithium-Ion Cells Using Three-Dimensionally Structured Solid Electrolyte $Li_7La_3Zr_2O_{12}$ Pellets. *Frontiers in Energy Research* **2016**, *4*. DOI: 10.3389/fenrg.2016.00032.

(97) Kim, J.; Kim, M.; Noh, S.; Lee, G.; Shin, D. Enhanced electrochemical performance of surface modified $LiCoO_2$ for all-solid-state lithium batteries. *Ceram. Int.* **2016**, *42* (2), 2140-2146. DOI: 10.1016/j.ceramint.2015.09.126.

(98) Ishii, K.; Uchikoshi, T.; Miyoshi, S.; Ode, M.; Ohno, T.; Takada, K. Reactivity

evaluation of NASICON-type solid electrolyte LATP, LAGP and Olivine-type cathode LCP. *Mater. Lett.* **2022**, *324*. DOI: 10.1016/j.matlet.2022.132736.

(99) Tian, H.-K.; Jalem, R.; Gao, B.; Yamamoto, Y.; Muto, S.; Sakakura, M.; Iriyama, Y.; Tateyama, Y. Electron and Ion Transfer across Interfaces of the NASICON-Type LATP Solid Electrolyte with Electrodes in All-Solid-State Batteries: A Density Functional Theory Study via an Explicit Interface Model. *ACS Applied Materials & Interfaces* **2020**, *12* (49), 54752-54762. DOI: 10.1021/acsami.0c16463.

(100) Robertsona, A. D.; Westa, A. R.; Ritchieb, A. G. Review of crystalline lithium-ion conductors suitable for high temperature battery applications. *Solid State Ionics* **1997**, *104*, 1-11. DOI: 10.1016/S0167-2738(97)00429-3.

(101) Pervez, S. A.; Cambaz, M. A.; Thangadurai, V.; Fichtner, M. Interface in Solid-State Lithium Battery: Challenges, Progress, and Outlook. *ACS Appl Mater Interfaces* **2019**, *11* (25), 22029-22050. DOI: 10.1021/acsami.9b02675 From NLM PubMed-not-MEDLINE.

(102) Lau, J.; DeBlock, R. H.; Butts, D. M.; Ashby, D. S.; Choi, C. S.; Dunn, B. S. Sulfide Solid Electrolytes for Lithium Battery Applications. *Advanced Energy Materials* **2018**, *8* (27). DOI: 10.1002/aenm.201800933.

(103) Wagner, R.; Redhammer, G. J.; Rettenwander, D.; Senyshyn, A.; Schmidt, W.; Wilkening, M.; Amthauer, G. Crystal Structure of Garnet-Related Li-Ion Conductor $Li_{7-3x}Ga_xLa_3Zr_2O_{12}$: Fast Li-Ion Conduction Caused by a Different Cubic Modification? *Chem. Mater.* **2016**, *28* (6), 1861-1871. DOI: 10.1021/acs.chemmater.6b00038 From NLM PubMed-not-MEDLINE.

(104) Hamao, N.; Kataoka, K.; Kijima, N.; Akimoto, J. Synthesis, crystal structure and

conductive properties of garnet-type lithium ion conductor Al-free $Li_{7-x}La_3Zr_{2-x}Ta_xO_{12}$ ($0 \leq x \leq 0.6$). *J. Ceram. Soc. Jpn.* **2016**, *124* (6), P6-1-P6-3. DOI: 10.2109/jcersj2.124.P6-1.

(105) Tong, Z.; Wang, S.-B.; Liao, Y.-K.; Hu, S.-F.; Liu, R.-S. Interface Between Solid-State Electrolytes and Li-Metal Anodes: Issues, Materials, and Processing Routes. *ACS Applied Materials & Interfaces* **2020**, *12* (42), 47181-47196. DOI: 10.1021/acsami.0c13591.

(106) Jiang, Z.; Han, Q.; Wang, S.; Wang, H. Reducing the Interfacial Resistance in All-Solid-State Lithium Batteries Based on Oxide Ceramic Electrolytes. *ChemElectroChem* **2019**, *6* (12), 2970-2983. DOI: 10.1002/celc.201801898.

(107) Xia, H.; Tang, S. B.; Lu, L. Thin Film Microbatteries Prepared by Pulsed Laser Deposition. *Journal of the Korean Physical Society* **2007**, *51* (3), 1055-1062. DOI: 10.3938/jkps.51.1055.

(108) Amatucci, G. G.; Tarascon, J. M.; Klein, L. C. CoO_2, The End Member of the $LiCoO_2$ Solid Solution. *Journal of Electrochemical Society* **1996**, *143*, 1114. DOI: 10.1149/1.1836594.

(109) Wentworth, R. A. D.; Piper, T. S. A Crystal Field Model for the Spectral Relationships inMonoacidopentaammine and Diacdotetraammine Complexes of Cobalt(III). *Inorganic Chemistry* **1965**, *4*, 709-714. DOI: 10.1021/ic50027a024.

(110) Marianetti, C. A.; Kotliar, G.; Ceder, G. A first-order Mott transition in Li_xCoO_2. *Nat Mater* **2004**, *3* (9), 627-631. DOI: 10.1038/nmat1178 From NLM Medline.

(111) Ensling, D.; Cherkashinin, G.; Schmid, S.; Bhuvaneswari, S.; Thissen, A.; Jaegermann, W. Nonrigid Band Behavior of the Electronic Structure of $LiCoO_2$ Thin Film during Electrochemical Li Deintercalation. *Chem. Mater.* **2014**, *26* (13),

3948-3956. DOI: 10.1021/cm501480b.

(112) Dahéron, L.; Dedryvère, R.; Martinez, H.; Ménétrier, M.; Denage, C.; Delmas, C.; Gonbeau, D. Electron Transfer Mechanisms upon Lithium Deintercalation from $LiCoO_2$ to CoO_2. *Chem. Mater.* **2008**, *20*, 583-590. DOI: 10.1021/cm702546s.

(113) Mizokawa, T.; Fujimori, A. Electronic structure and orbital ordering in perovskite-type 3d transition-metal oxides studied by Hartree-Fock band-structure calculations. *Physical Review B* **1996**, *B54*, 5368. DOI: 10.1103/PhysRevB.54.5368.

(114) Mizokawa, T.; Wakisaka, Y.; Sudayama, T.; Iwai, C.; Miyoshi, K.; Takeuchi, J.; Wadati, H.; Hawthorn, D. G.; Regier, T. Z.; Sawatzky, G. A. Role of oxygen holes in Li_xCoO_2 revealed by soft X-ray spectroscopy. *Phys. Rev. Lett.* **2013**, *111* (5), 056404. DOI: 10.1103/PhysRevLett.111.056404 From NLM PubMed-not-MEDLINE.

(115) Yazami, R.; Touzain, P. A reversible graphite-lithium negative electrode for electrochemical generators. *J. Power Sources* **1983**, *9* (3), 365-371. DOI: 10.1016/0378-7753(83)87040-2.

(116) Billaud, D.; Henry, F. X.; Willmann, P. Electrochemical sysnthesis of binary graphite-lithium intercalation compounds. *Mater. Res. Bull.* **1993**, *28* (5), 477-483. DOI: 10.1016/0025-5408(93)90130-6.

(117) An, S. J.; Li, J.; Daniel, C.; Mohanty, D.; Nagpure, S.; Wood, D. L. The state of understanding of the lithium-ion-battery graphite solid electrolyte interphase (SEI) and its relationship to formation cycling. *Carbon* **2016**, *105*, 52-76. DOI: 10.1016/j.carbon.2016.04.008.

(118) Park, C. M.; Kim, J. H.; Kim, H.; Sohn, H. J. Li-alloy based anode materials for

Li secondary batteries. *Chem. Soc. Rev.* **2010**, *39* (8), 3115-3141. DOI: 10.1039/b919877f From NLM PubMed-not-MEDLINE.

(119) Lai, S.-C. Solid Lithium-Silicon Electrode. *J. Electrochem. Soc.* **1976**, *123*, 1196. DOI: 10.1149/1.2133033

(120) Sharma, R. A.; Seefurth, R. N. Thermodynamic Properties of the Lithium‐Silicon System. *J. Electrochem. Soc.* **1976**, *123*, 1763. DOI: 10.1149/1.2132692.

(121) Seefurth, R. N.; Sharma, R. A. Investigation of Lithium Utilization from A Lithium‐Silicon Electrode. *J. Electrochem. Soc.* **1977**, *124*, 1207. DOI: 10.1149/1.2133529.

(122) WEN, C. J.; HUGGINS, R. A. Chemical Diffusion in Intermediate Phases in the Lithium-Silicon. *J. Solid State Chem.* **1981**, *37*, 271-278. DOI: 10.1016/0022-4596(81)90487-4.

(123) Obrovac, M. N.; Krause, L. J. Reversible Cycling of Crystalline Silicon Powder. *J. Electrochem. Soc.* **2007**, *154*, A103-A108. DOI: 10.1149/1.2402112.

(124) Hatchard, T. D.; Dahn, J. R. In Situ XRD and Electrochemical Study of the Reaction of Lithium with Amorphous Silicon. *J. Electrochem. Soc.* **2004**, *151*, A838-A842. DOI: 10.1149/1.1739217.

(125) Endo, R.; Ohnishi, T.; Takada, K.; Masuda, T. Electrochemical Lithiation and Delithiation in Amorphous Si Thin Film Electrodes Studied by Operando X-ray Photoelectron Spectroscopy. *J. Phys. Chem. Lett* **2022**, *13* (31), 7363-7370. DOI: 10.1021/acs.jpclett.2c01312 From NLM PubMed-not-MEDLINE.

(126) Ohta, N.; Kimura, S.; Sakabe, J.; Mitsuishi, K.; Ohnishi, T.; Takada, K. Anode Properties of Si Nanoparticles in All-Solid-State Li Batteries. *ACS Applied Energy*

Materials **2019**, *2* (10), 7005-7008. DOI: 10.1021/acsaem.9b01517.

(127) Sakabe, J.; Ohta, N.; Ohnishi, T.; Mitsuishi, K.; Takada, K. Porous amorphous silicon film anodes for high-capacity and stable all-solid-state lithium batteries. *Communications Chemistry* **2018**, *1* (1). DOI: 10.1038/s42004-018-0026-y.

(128) Loveridge, M. J.; Lain, M. J.; Johnson, I. D.; Roberts, A.; Beattie, S. D.; Dashwood, R.; Darr, J. A.; Bhagat, R. Towards High Capacity Li-ion Batteries Based on Silicon-Graphene Composite Anodes and Sub-micron V-doped $LiFePO_4$ Cathodes. *Sci Rep* **2016**, *6*, 37787. DOI: 10.1038/srep37787 From NLM PubMed-not-MEDLINE.

(129) Key, B.; Morcrette, M.; Tarascon, J.-M.; Grey, C. P. Pair Distribution Function Analysis and Solid State NMR Studies of Silicon Electrodes for Lithium Ion Batteries: Understanding the (De)lithiation Mechanisms. *Journal of the American Chemical Society* **2010**, *133*, 503-512. DOI: 10.1021/ja108085d.

(130) Putra, R. P.; Matsushita, K.; Ohnishi, T.; Masuda, T. Operando Nanomechanical Mapping of Amorphous Silicon Thin Film Electrodes in All-Solid-State Lithium-Ion Battery Configuration during Electrochemical Lithiation and Delithiation. *J Phys Chem Lett* **2024**, *15* (2), 490-498. DOI: 10.1021/acs.jpclett.3c03012 From NLM PubMed-not-MEDLINE.

(131) Nguyen, C. C.; Lucht, B. L. Comparative Study of Fluoroethylene Carbonate and Vinylene Carbonate for Silicon Anodes in Lithium Ion Batteries. *J. Electrochem. Soc.* **2014**, *161* (12), A1933-A1938. DOI: 10.1149/2.0731412jes.

(132) Kitada, K.; Pecher, O.; Magusin, P.; Groh, M. F.; Weatherup, R. S.; Grey, C. P. Unraveling the Reaction Mechanisms of SiO Anodes for Li-Ion Batteries by Combining in Situ ^{7}Li and ex Situ $^{7}Li/^{29}Si$ Solid-State NMR Spectroscopy. *J. Am.*

Chem. Soc. **2019**, *141* (17), 7014-7027. DOI: 10.1021/jacs.9b01589 From NLM PubMed-not-MEDLINE.

(133) Li, J.; Dahn, J. R. An In Situ X-Ray Diffraction Study of the Reaction of Li with Crystalline Si. *J. Electrochem. Soc.* **2007**, *154*, A156. DOI: 10.1149/1.2409862.

(134) Obrovacz, M. N.; Christensen, L. Structural Changes in Silicon Anodes during Lithium Insertion/Extraction. *Electrochem. Solid-State Lett.* **2004**, *7*, A93-A96. DOI: 10.1149/1.1652421.

(135) Liu, X. H.; Zhang, L. Q.; Zhong, L.; Liu, Y.; Zheng, H.; Wang, J. W.; Cho, J.-H.; Dayeh, S. A.; Picraux, S. T.; Sullivan, J. P.; et al. Ultrafast Electrochemical Lithiation of Individual Si Nanowire Anodes. *Nano Lett.* **2011**, *11* (6), 2251-2258. DOI: 10.1021/nl200412p.

(136) Liu, X. H.; Zhong, L.; Huang, S.; Mao, S. X.; Zhu, T.; Huang, J. Y. Size-Dependent Fracture of Silicon Nanoparticles During Lithiation. *ACS Nano* **2012**, *6*, 1522-1531. DOI: 10.1021/nn204476h.

(137) Key, B.; Bhattacharyya, R.; Morcrette, M.; Sezne´c, V.; Tarascon, J.-M.; Grey, C. P. Real-Time NMR Investigations of Structural Changes in Silicon Electrodes for Lithium-Ion Batteries. *J. Am. Ceram. Soc.* **2008**, *131*, 9239-9249. DOI: 10.1021/ja8086278.

(138) Ogata, K.; Salager, E.; Kerr, C. J.; Fraser, A. E.; Ducati, C.; Morris, A. J.; Hofmann, S.; Grey, C. P. Revealing lithium-silicide phase transformations in nano-structured silicon-based lithium ion batteries via in situ NMR spectroscopy. *Nat Commun* **2014**, *5*, 3217. DOI: 10.1038/ncomms4217 From NLM PubMed-not-MEDLINE.

(139) Chan, C. K.; Ruffo, R.; Hong, S. S.; Huggins, R. A.; Cui, Y. Structural and

electrochemical study of the reaction of lithium with silicon nanowires. *J. Power Sources* **2009**, *189* (1), 34-39. DOI: 10.1016/j.jpowsour.2008.12.047.

(140) Miyazaki, R.; Ohta, N.; Ohnishi, T.; Takada, K. Anode properties of silicon-rich amorphous silicon suboxide films in all-solid-state lithium batteries. *J. Power Sources* **2016**, *329*, 41-49. DOI: 10.1016/j.jpowsour.2016.08.070.

(141) Haruta, M.; Doi, T.; Inaba, M. Oxygen-Content Dependence of Cycle Performance and Morphology Changes in Amorphous-SiO_x Thin-Film Negative Electrodes for Lithium-Ion Batteries. *J. Electrochem. Soc.* **2019**, *166* (2), A258-A263. DOI: 10.1149/2.0861902jes.

(142) Nguyen, C. C.; Choi, H.; Song, S.-W. Roles of Oxygen and Interfacial Stabilization in Enhancing the Cycling Ability of Silicon Oxide Anodes for Rechargeable Lithium Batteries. *J. Electrochem. Soc.* **2013**, *160* (6), A906-A914. DOI: 10.1149/2.118306jes.

(143) Sugimoto, R.; Marumoto, K.; Haruta, M.; Inaba, M.; Doi, T. Quantitative Evaluation and Improvement of Interfacial Li^+ Transfer Between SiO_x Electrode and Garnet‐Type Ta‐Doped $Li_7La_3Zr_2O_{12}$ Electrolyte. *ChemElectroChem* **2022**, *9* (17). DOI: 10.1002/celc.202200491.

(144) Kim, T.; Park, S.; Oh, S. M. Solid-State NMR and Electrochemical Dilatometry Studyon Li^+Uptake Extraction Mechanism in SiO Electrode. *J. Electrochem. Soc.* **2007**, *154*. DOI: 10.1149/1.2790282.

(145) Takezawa, H.; Ito, S.; Yoshizawa, H.; Abe, T. Structural stabilization on SiO_x film anode with large areal capacity for enhanced cyclability in lithium-ion batteries. *J. Power Sources* **2016**, *324*, 45-51. DOI: 10.1016/j.jpowsour.2016.05.061.

(146) Li, S.; Tsutsumi, S.; Shironita, S.; Umeda, M. Peak Attribution of the Differential

Capacity Profile of a $LiCoO_2$ -based Three-electrode Li-ion Laminate Cell. *Electrochemistry* **2022**, *90* (3), 037004-037004. DOI: 10.5796/electrochemistry.21-00128.

(147) Endo, R.; Ohnishi, T.; Takada, K.; Masuda, T. In Situ Observation of Lithiation and Delithiation Reactions of a Silicon Thin Film Electrode for All-Solid-State Lithium-Ion Batteries by X-ray Photoelectron Spectroscopy. *J. Phys. Chem. Lett* **2020**, *11* (16), 6649-6654. DOI: 10.1021/acs.jpclett.0c01906 From NLM PubMed-not-MEDLINE.

(148) Endo, R.; Ohnishi, T.; Takada, K.; Masuda, T. Instrumentation for tracking electrochemical reactions by x-ray photoelectron spectroscopy under conventional vacuum conditions. *Journal of Physics Communications* **2021**, *5* (1), 015001. DOI: 10.1088/2399-6528/abd617.

2. Experimental

2.1 Sample preparation

2.1.1 Fabrication of an all-solid-state (ASS) cell in Chapter 4

In the Chapter 4, electrochemical reactions of $LiCoO_2$ cathode in an ASS cell configuration were investigated. Thus, in this section, the preparation method for the ASS cell with configurations of Pt/$LiCoO_2$ (LCO)-Li_3BO_3 (LBO)/Nb or Ta/ $Li_{6.6}La_3Zr_{1.6}Ta_{0.4}O_{12}$ (LLZT)/Li shown in Figure 2-1 is described.

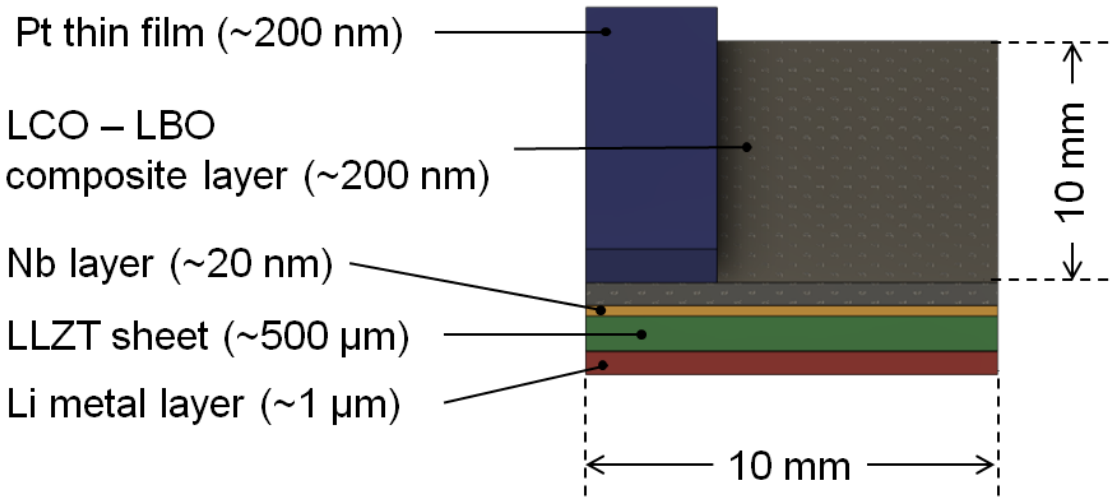

Figure 2-1. Schematic illustration of the Pt/LCO-LBO/Nb or Ta/LLZT/Li cell.

Fabrication procedure was slightly different between section 4.2.1 and 4.2.2 in Chapter 4. One side of a $Li_{6.6}La_3Zr_{1.6}Ta_{0.4}O_{12}$ solid electrolyte sheet (10mm × 10mm × 500 μm; LLZT, Toshima Manufacturing Co., Ltd., Japan) was sandblasted with 220-grit alumina powder to obtain a rough surface. After annealing at 700 °C for 2 hours, the

LLZT was immersed in an aqueous solution saturated with LiOH for 1 hour to remove resistive species, such as LiOH and Li_2CO_3. A 20 nm-thick Nb (section 4.2.1) or Ta (section 4.2.2) thin layer was deposited on the sandblasted surface of LLZT by DC sputtering using Ar gas, and 1.892 mg (section 4.2.1) or 1.398 mg (section 4.2.2) of LCO fine powder with an average particle size of around 200 nm, was applied to the LLZT precoated with Nb or Ta layer. A 10 μL droplet of aqueous solution saturated with LiOH was placed on the LCO-applied LLZT and then dried in a vacuum. Subsequently, a 10 μL droplet of aqueous solution saturated with H_3BO_3 was placed on the LCO-applied LLZT and then dried in a vacuum. Finally, the LLZT was annealed at 700 °C for 2 hours under an oxygen flow to form a LCO-LBO composite cathode on a Nb or Ta interlayer-coated LLZT. Pt thin layer with a thickness of 200 nm was overcoated on a 10 mm × 4 mm rectangular area of LCO-LBO composite cathode, as a current collector.

The other side of LLZT was mechanically polished by 600-grit sandpaper and then a 1 μm-thick Li thin layer was formed by thermal evaporation. After placing a piece of Li metal foil with a thickness of 100 μm as an anode, the LLZT was heated at 200 °C for 30 min to yield an ASS cell in the LCO-LBO/Ta/LLZT/ Li configuration.

Although the Nb or Ta thin layer sandwiched by the LCO-LBO composite cathode and LLZT should be converted to a Li^+ ion conductive amorphous Li-Nb-O or Li-Ta-O

phase after heating,[1] the interlayer is denoted as Ta because no experimental evidence was obtained in the present study.

2.1.2 Fabrication of an ASS thin-film cell in Chapter 5

In the Chapter 5, lithiation and delithiation processes of $SiO_{0.53}$ anode in thin-film cell-configuration were investigated. Thus, in this section, the preparation method for the ASS thin-film cell with configurations of Cu/$SiO_{0.53}$/LLZT/Li in Figure 2-2 is described.

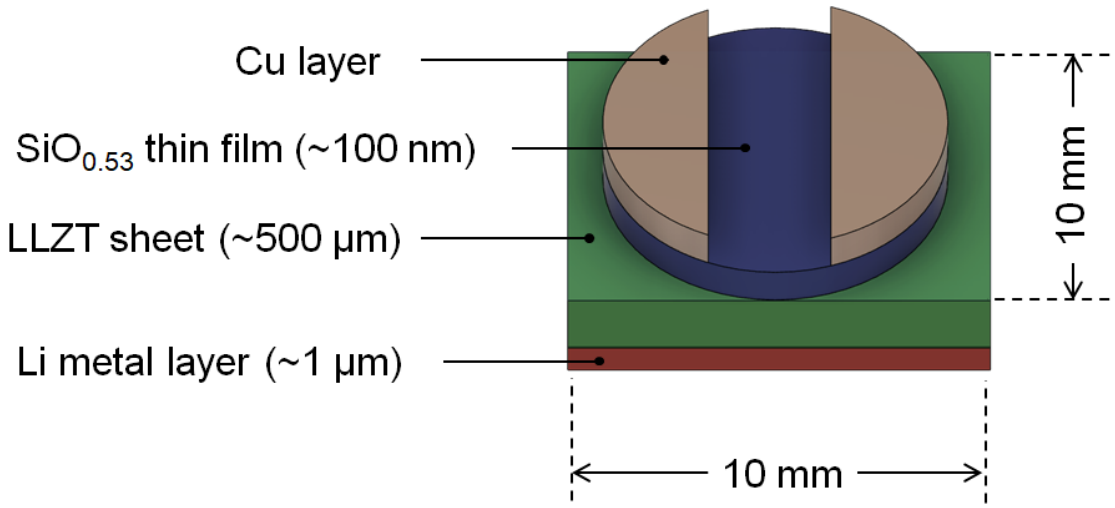

Figure 2-2. Schematic illustration of the Cu/$SiO_{0.53}$/LLZT/Li

The $SiO_{0.53}$ thin films were prepared on the LLZT sheets in the same batch used in Chapter 4 by radio-frequency magnetron sputtering (SPAD-2240UM, Advanced Optics Vacuum Co., Ltd.) using Ar/O_2 gas mixtures.[2] The thickness of $SiO_{0.53}$ thin film was ca. 100 nm. The surface of sputter-deposited $SiO_{0.53}$ thin film was coated with a copper

layer as a current collector by direct current (DC) sputtering. The samples were mounted on the stage of QUICK COATER (SC-701, Sanyu Electron Co., Ltd.) in the Ar-filled glove box. The Cu deposition was performed at the pressure of about 10^1 Pa. During the copper deposition, a center rectangular part with about 4 mm × 10 mm was masked using a stainless-steel stencil mask to yield an uncoated area exposing amorphous $SiO_{0.53}$ layer for XPS measurement. The LLZT surface of the LLZT/Si/Cu structure was polished by using 400-grit sandpapers. The Li metal layer with a diameter of 8.5 mm was thermally deposited on the LLZT surface from a Li wire (Honjo Metal Co., Ltd.). The thickness of Li deposition is approximately 1.5 μm which is larger than that required for the formation of the theoretical maximum composition ($Li_{3.75}Si$) with the 100 nm-thick $SiO_{0.53}$.

2.2 Characterization

2.2.1 X-ray photoelectron spectroscopy (XPS)

X-ray photoelectron spectroscopy (XPS) is capable of nondestructively analyzing the elemental composition, oxidation states, and electronic states of a solid surface by detecting photoelectrons ejected by x-ray irradiation.[3-7] The kinetic energies of the photoelectrons are characteristic of the core levels of the chemical species and are represented by the following equation.[8]

$$E_k = h\nu - E_b - \phi \quad (1)$$

where E_k is the kinetic energy of emitted photoelectrons, $h\nu$ is the energy of incident x-rays, E_b is the binding energy of electrons at core levels, ϕ is the work function of the sample of interest. Thus, surface-sensitive information is obtained by using conventional laboratory-based XPS equipped with an Al-Kα (1486.7 eV) or Mg-Kα (1253.6 eV) source because E_k (~1000 eV or less) and corresponding inelastic mean free path (IMFP) are relatively small.[8]

2.2.1.1 XPS measurements in Chapter 5

The lithiation and delithiation of the $SiO_{0.53}$ thin-film cell was investigated using *in-situ* XPS system.[9] The Cu thin layer on $SiO_{0.53}$ thin-film working-electrode was electrically connected to the hemispherical analyzer through the sample holder, while the Li counter electrode was insulated from the $SiO_{0.53}$ working electrode side. The cell mounted on sample holder was transferred from an Ar-filled glove box to XPS apparatus (Shimadzu, Kratos) without air exposure using a transfer vessel. After transferring the sample into the analysis chamber, two independent terminals encounter the $SiO_{0.53}$ working electrode and Li counter electrode side. This allows us to apply a bias between the $SiO_{0.53}$ working electrode and Li counter electrode by a potentiostat outside vacuum. XPS measurements were performed in the analysis chamber kept under

a pressure of 5×10^{-8} Torr. X-rays from monochromatic Al-Kα (1486.7 eV) source at a power of 300 W with a spot size of 200 μm were incident to the exposed area of the $SiO_{0.53}$ working electrode. The pass energy of the photoelectrons was fixed at 80 eV. The obtained spectra were fitted using the Voigt function after the background subtraction by using a Shirley method.[10] Dynamic XPS measurements in which Si 2p, C 1s, O 1s, and Li 1s photoelectron spectra were continuously measured throughout the charge/discharge cycles.

2.2.2 Hard x-ray photoelectron spectroscopy (HAXPES)

XPS using hard x-rays, i.e., hard x-ray photoelectron spectroscopy (HAXPES), enables us to analyze the surface and deeper layer buried at depth > 50 nm because it generates photoelectrons with E_k higher than that in the conventional XPS using an Al-Kα source.[11-13] In general, photoionization cross-section of core levels becomes relatively low for hard x-ray excitation.[11, 13] Therefore, in the 2000s, pioneering HAXPES measurements were performed in synchrotron radiation facilities because hard x-rays with a high photon flux were available.[11] However, laboratory-based HAXPES instruments equipped with Cr-Kα (5414.9 eV) or Ga-Kα (9250 eV) sources have been developed in recent years.[14, 15]

2.2.2.1 HAXPES measurements in Chapter 4

The 200 nm-thick Pt thin layer on LCO-LBO cathode was electrically connected to the hemispherical analyzer through the terminal A and base plate, while the Li anode was insulated from the LCO-LBO cathode side by the insulating plate on the base plate (Figure 2-3). The cell mounted on sample holder was transferred from an Ar-filled glove box to HAXPES apparatus (Scienta omicron, ULVAC-PHI) without air exposure. After transferring the sample into the analysis chamber, terminals B and C encounter the Li anode and LCO-LBO cathode sides, respectively. This allows us to apply a bias between the Li anode and LCO-LBO cathode by a potentiostat outside vacuum. HAXPES measurements were performed in the analysis chamber kept under a pressure of 2×10^{-8} mbar. X-rays from monochromatic Cr-Kα (5414.9 eV) source at a power of 50 W with a spot size of 200 μm were incident to the exposed area of the LCO-LBO composite cathode with an incident angle θ of 75°. The pass energy of the photoelectrons was fixed at 200 eV. The obtained spectra were fitted using the Voigt function after the background subtraction by using a Shirley method.[10] In addition to static HAXPES measurements of pristine and electrochemically treated cell 30 min after each charge/discharge process, dynamic HAXPES measurements in which B 1s (section 4.2.1 in Chapter 4) or Pt 4f (section 4.2.2 in Chapter 4) and Co $2p_{3/2}$ photoelectron

spectra were alternately measured throughout the charge/discharge cycles.

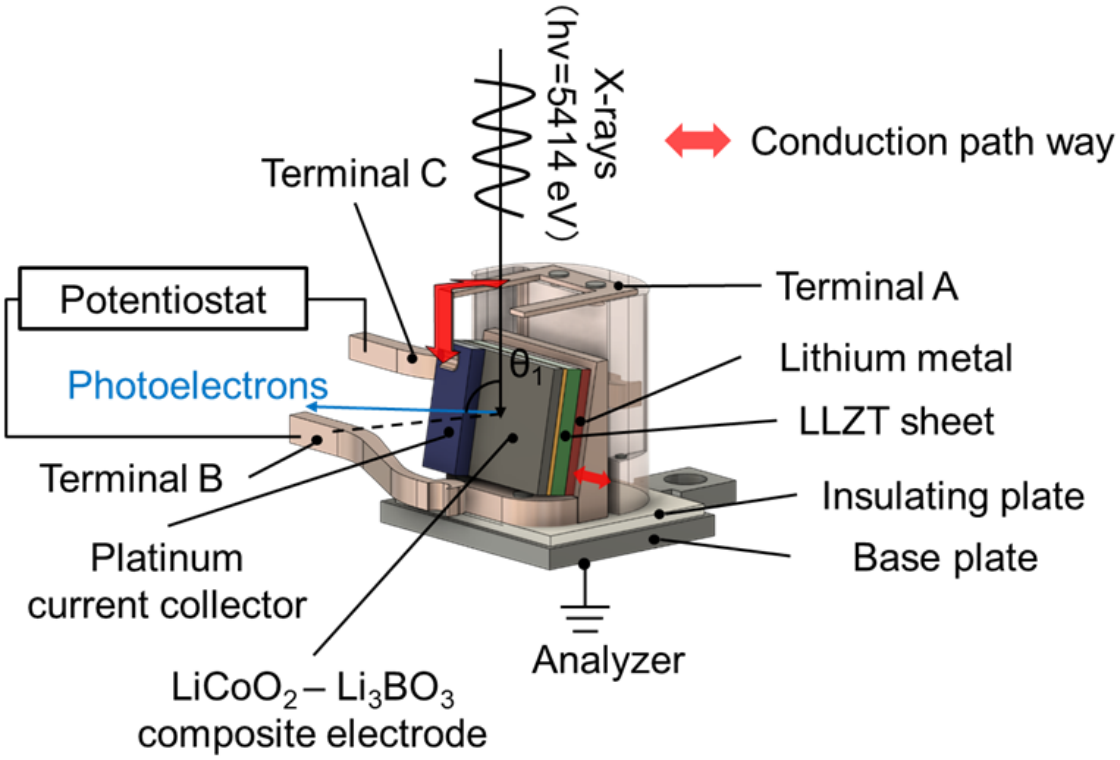

Figure 2-3. Schematic illustration of the sample holder for HAXPES measurements.

2.2.3 Electrochemical measurements

2.2.3.1 Galvanostatic charging/discharging analysis in Chapter 4

A galvanostatic charge/discharge cycles were carried out at a constant current of ±12.96μA corresponding to 0.05C in potential ranges of 3.0 – 4.2 V and 3.0 – 4.7 V vs. Li^+/Li using a potentio-galvanostat (Bio-Logic VSP-300) at room temperature. The potential given herein is expressed versus Li^+/Li unless otherwise noted.[16]

2.2.3.2 Galvanostatic lithiation/delithiation analysis in Chapter 5

The galvanostatic and/or potentiostatic lithiation/delithiation were carried out in the analysis chamber kept under a pressure of about 7×10^{-9} Torr. The sample holder in the chamber and a potentio-galvanostat at the outside were connected by coaxial cables via vacuum feed through.[9] The cell voltage, i.e., potential difference between $SiO_{0.53}$ as a working electrode and Li as a counter electrode, was monitored under constant current and/or voltage conditions. The cutoff potential was set to be 0.02 and 1.5 V (vs. Li^+/Li). The capacity values are given in mAh g^{-1} based on the weight of Si in $SiO_{0.53}$ thin film.

2.2.4 Ellipsometry measurements in Chapter 3

The ellipsometry measurements were performed using variable-angle spectroscopic ellipsometry (Alpha-SE VASE, J.A. Woollam Co.) at incident angles of 65°, 70°, and 75° and wavelengths of 380 – 900 nm for confirming the angle-resolved measurement function in Chapter 3. The thicknesses of the SiO_2 layers formed on the Si substrate were determined using the J. A. Woollam (JAW) standard model[17] composed of a SiO_2 layer, an interlayer between the SiO_2 layer and the Si substrate, and a Si substrate. The optical constants of the SiO_2 and interlayer in the model were determined using the Sellmeier function,[17] one of the empirical equations relating the refractive index and wavelength for transparent media. On the other hand, the optical constant of the Si

substrate was determined using a parametric functional model.[17]

References

(1) Kato, T.; Hamanaka, T.; Yamamoto, K.; Hirayama, T.; Sagane, F.; Motoyama, M.; Iriyama, Y. In-situ $Li_7La_3Zr_2O_{12}/LiCoO_2$ interface modification for advanced all-solid-state battery. *J. Power Sources* **2014**, *260*, 292-298. DOI: 10.1016/j.jpowsour.2014.02.102.

(2) Sugimoto, R.; Marumoto, K.; Haruta, M.; Inaba, M.; Doi, T. Quantitative Evaluation and Improvement of Interfacial Li^+ Transfer Between SiO_x Electrode and Garnet-Type Ta-Doped $Li_7La_3Zr_2O_{12}$ Electrolyte. *ChemElectroChem* **2022**, *9* (17). DOI: 10.1002/celc.202200491.

(3) Kersell, H.; Chen, P.; Martins, H.; Lu, Q.; Brausse, F.; Liu, B.-H.; Blum, M.; Roy, S.; Rude, B.; Kilcoyne, A.; et al. Simultaneous ambient pressure x-ray photoelectron spectroscopy and grazing incidence x-ray scattering in gas environments. *Rev. Sci. Instrum.* **2021**, *92* (4), 044102. DOI: 10.1063/5.0044162.

(4) Toyoshima, R.; Yoshida, M.; Monya, Y.; Kousa, Y.; Suzuki, K.; Abe, H.; Mun, B. S.; Mase, K.; Amemiya, K.; Kondoh, H. In Situ Ambient Pressure XPS Study of CO Oxidation Reaction on Pd(111) Surfaces. *The Journal of Physical Chemistry C* **2012**, *116* (35), 18691-18697. DOI: 10.1021/jp301636u.

(5) Seo, M.; Lee, Y.; Shin, H.; Kim, E.; Kim, H. S.; Chung, K. B.; Kim, G.; Mun, B. S. Effect of Bias Potential on the Interface of a Solid Electrolyte and Electrode during XPS Depth Profiling Analysis. *ACS Appl Mater Interfaces* **2024**, *16* (20), 26922-26931. DOI: 10.1021/acsami.4c03597 From NLM PubMed-not-MEDLINE.

(6) Kondoh, H.; Toyoshima, R.; Monya, Y.; Yoshida, M.; Mase, K.; Amemiya, K.; Mun, B. S. In situ analysis of catalytically active Pd surfaces for CO oxidation with near ambient pressure XPS. *Catal. Today* **2016**, *260*, 14-20. DOI:

10.1016/j.cattod.2015.05.016.

(7) Nagasaka, M.; Kondoh, H.; Amemiya, K.; Ohta, T.; Iwasawa, Y. Proton transfer in water–hydroxyl mixed overlayers on Pt(1 1 1): Combined approach of laser desorption and spatially-resolved X-ray photoelectron spectroscopy. *Surface Science* **2009**, *603* (10-12), 1690-1695. DOI: 10.1016/j.susc.2008.09.054.

(8) Fadley, C. S.; Shirley, D. A. Electronic densities of states from x-ray photoelectron spectroscopy. *J. Res. Natl. Bur. Stand. Sec. A* **1970**, *74A* (4), 543. DOI: 10.6028/jres.074a.045.

(9) Endo, R.; Ohnishi, T.; Takada, K.; Masuda, T. Instrumentation for tracking electrochemical reactions by x-ray photoelectron spectroscopy under conventional vacuum conditions. *Journal of Physics Communications* **2021**, *5* (1), 015001. DOI: 10.1088/2399-6528/abd617.

(10) Schmid, M.; Steinrück, H.-P.; Gottfried, J. M. A new asymmetric Pseudo-Voigt function for more efficient fitting of XPS lines. *Surf. Interface Anal.* **2014**, *46* (8), 505-511. DOI: 10.1002/sia.5521.

(11) Kalha, C.; Fernando, N. K.; Bhatt, P.; Johansson, F. O. L.; Lindblad, A.; Rensmo, H.; Medina, L. Z.; Lindblad, R.; Siol, S.; Jeurgens, L. P. H.; et al. Hard x-ray photoelectron spectroscopy: a snapshot of the state-of-the-art in 2020. *J. Phys.: Condens. Matter* **2021**, *33*, 233001. DOI: 10.1088/1361-648X/abeacd.

(12) Spencer, B. F.; Maniyarasu, S.; Reed, B. P.; Cant, D. J. H.; Ahumada-Lazo, R.; Thomas, A. G.; Muryn, C. A.; Maschek, M.; Eriksson, S. K.; Wiell, T.; et al. Inelastic background modelling applied to hard X-ray photoelectron spectroscopy of deeply buried layers: A comparison of synchrotron and lab-based (9.25 keV) measurements. *Appl. Surf. Sci.* **2021**, *541*, 148635. DOI:

10.1016/j.apsusc.2020.148635.

(13) Siol, S.; Mann, J.; Newman, J.; Miyayama, T.; Watanabe, K.; Schmutz, P.; Cancellieri, C.; Jeurgens, L. P. H. Concepts for chemical state analysis at constant probing depth by lab-based XPS/HAXPES combining soft and hard X-ray sources. *Surf. Interface Anal.* **2020**, *52* (12), 802-810. DOI: 10.1002/sia.6790.

(14) Kobayashi, K.; Kobata, M.; Iwai, H. Development of a laboratory system hard X-ray photoelectron spectroscopy and its applications. *J. Electron. Spectrosc. Relat. Phenom.* **2013**, *190*, 210-221. DOI: 10.1016/j.elspec.2013.04.007.

(15) Regoutz, A.; Mascheck, M.; Wiell, T.; Eriksson, S. K.; Liljenberg, C.; Tetzner, K.; Williamson, B. A. D.; Scanlon, D. O.; Palmgren, P. A novel laboratory-based hard X-ray photoelectron spectroscopy system. *Rev. Sci. Instrum.* **2018**, *89* (7), 073105. DOI: 10.1063/1.5039829.

(16) Iwama, T.; Ohnishi, T.; Masuda, T. Operando Observation of Lithiation and Delithiation Reactions of a $LiCoO_2$-Li_3BO_3 Composite Electrode Formed on a $Li_{6.6}La_3Zr_{1.6}Ta_{0.4}O_{12}$ Solid Electrolyte Sheet by Laboratory-based Hard X-ray Photoelectron Spectroscopy. *Electrochemistry* **2023**, *91* (11), 117005. DOI: 10.5796/electrochemistry.23-00090.

(17) Herzinger, C. M.; Johs, B.; McGahan, W. A.; Woollam, J. A.; Paulson, W. Ellipsometric determination of optical constants for silicon and thermally grown silicon dioxide via a multi-sample, multi-wavelength, multi-angle investigation. *J. Appl. Phys.* **1998**, *83*, 3323. DOI: 10.1063/1.367101.

3. Instrumentation

3.1 Introduction

Hard x-ray photoelectron spectroscopy (HAXPES) has been used for a wide variety of materials to nondestructively analyze the electronic structure and chemical composition of solid/solid interfaces, such as metal-oxide-semiconductor (MOS) structures[1-3] and electrode/solid electrolyte interfaces in lithium-ion batteries including all-solid-state batteries.[4] Recently, HAXPES measurements under bias conditions have been reported. For example, changes in the interfacial densities at the dielectric/semiconductor interface and the potential distribution in each layer for MOS capacitors under bias applications were clarified by analyzing the magnitudes of photoelectron peak shifts attributed to the core level of the dielectric layer and semiconductor.[1, 5, 6] In addition, the electronic structure changes for an electrode and a solid-state electrolyte (SSE) of all-solid-state thin-film lithium-ion batteries during cycling were observed by analyzing the photoelectron peak changes derived from the electrode and SSE.[7-10]

Angle-resolved x-ray photoelectron spectroscopy (AR-XPS) enables us to obtain depth distributions of chemical species by tuning the geometry of the x-rays, sample,

and hemispherical analyzer, that is, take-off angles (TOAs). This technique has been used in a wide range of applications, such as observing the surface band alignments of semiconductors[11, 12] and analyzing the thickness of layered samples.[13, 14] When a laboratory-based XPS apparatus equipped with a conventional Al-Kα source is used, however, the information depth is limited to the nanometer scale from the sample surface.[15] Thus, AR-XPS using hard x-rays is strongly desired for investigating the depth profiles of chemical species and electronic states of solid/solid interfaces covered by a surface over layer in the tens-of-nanometer scale.[6]

Recently, our group developed an *in-situ* electrochemical XPS system using a laboratory-based XPS apparatus equipped with a conventional Al-Kα source and applied it to the lithiation/delithiation reactions at a-Si thin-film electrode deposited on a $Li_{6.6}La_3Zr_{1.6}Ta_{0.4}O_{12}$ (LLZT) solid electrolyte.[16-18] Although the previous work successfully observed the formation of irreversible surface over layers such as lithium-silicates, lithium oxides (Li_2O), and lithium carbonates (Li_2CO_3), as well as lithium silicides reversibly responding to lithiation/delithiation, information on bulk and interfaces buried within a solid electrode layer is limited because of its high surface sensitivity. In the present study, we develop an *operando* HAXPES system in which angle-resolved measurements of samples transferred without air exposure can be

performed under bias applications using a laboratory-based HAXPES apparatus equipped with a Cr-Kα source. The functions of the direct-current (DC) bias application and angle-resolved measurements were confirmed using metal Au foils and a SiO_2 film formed on a Si substrate.

3.2 Set up for applied HAXPES

A laboratory-based HAXPES instrument is composed of an Ar-filled glove box, a sample entry chamber, a preparation chamber, an analysis chamber, a hemispherical analyzer (Scienta omicron EW4000), and a x-ray source (Ulvac-phi, FXS36-500S) as shown in Figure 3-1. After certain pretreatment in the glove box, a sample is transferred into the sample entry chamber kept with an atmospheric pressure by supplying Ar gas from the glove box. After vacuum level reaches ~10^{-7} mbar, the sample stored in the sample entry chamber is further transferred to the analysis chamber kept in 5×10^{-9} mbar for the HAXPES measurements through the preparation chamber.

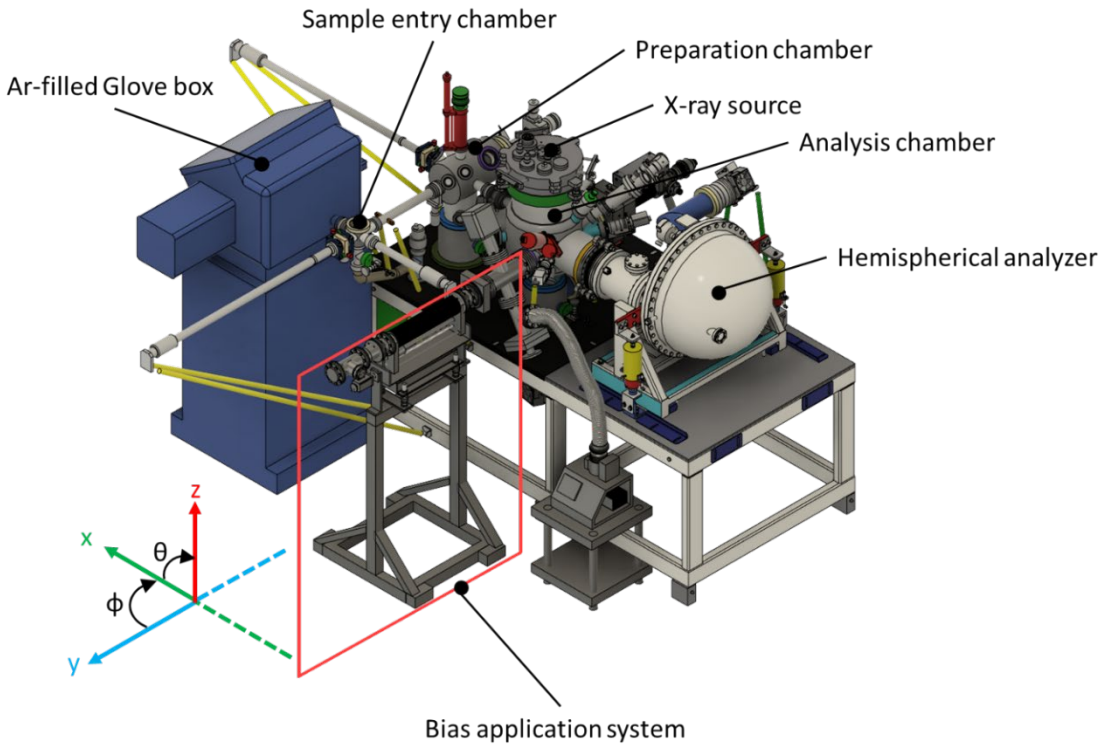

Figure 3-1. A schematic representation of HAXPES system.

Figure 3-2 shows schematic illustrations of the sample holder. Part A, made of oxygen-free copper, is electrically connected to terminal C by screws G (Figure 3-2 (a, b)) and grounded to the hemispherical analyzer through screws F and molybdenum stage D (Figure 3-2 (a, b)). The sample is pushed onto part B by terminal C to ensure electrical contact between the sample surface and the hemispherical analyzer through terminal C, screws G, part A, screws F, and molybdenum stage D (Figure 3-2 (b)). Because part B is electrically connected to the back side of the sample with insulation from part A and molybdenum stage D by ceramic plate E and insulators I (Figure 3-2 (b)), a bias can be

applied between the front and back sides of the samples by clipping the sample holder with terminals K and L, as shown in Figure 3-2 (c, d); terminals K and L are independently connected to parts A and B, respectively. A simplified schematic of the circuit is presented in Figure 3-2 (e).

As shown in Figure 3-2 (a) and (b), the lens axis of the hemispherical analyzer is parallel to the X-axis of sample holder in the initial stage, and the sample surface is tilted from the lens axis by a tilt angle θ_1 of ~ 75° to maximize the acceptance angles of photoelectrons emitted at the surface. To compensate for the small photoionization cross-section due to the use of hard x-rays,[19, 20] an oblique incident configuration is adopted; the sample-mounting surface of part B is tilted at θ_2 of 15° to the axis of incident x-rays. The x-ray spots at the incident angle θ_2 of 90° and 15° are a circle with a diameter of approximately 200 μm and rectangular with a size of approximately 200 μm × 773 μm, respectively.

Electrical connections of terminal K-part B and terminal L-part A were maintained during the azimuthal rotation of the sample holder along the Z-axis, as shown in Figure 3-2 (f) and (g). Because the axis of this azimuthal rotation was identical to the axis of the incident x-rays, the irradiation area remained unchanged during the angle-resolved

measurements. Figure 3-3 shows the x-ray irradiation area at various azimuthal rotation angles Φ in the range of 0° – 75° projected on a phosphor screen placed in the part B of the sample holder shown in Figure 3-2 (a) and (b). The blue spot in Figure 3-3 indicates the irradiated x-ray on the phosphor screen. The irradiation area remanied unchanged during the angle-resolved measurements. The irradiation area at various rotation angles Φ in the range of 0° – 75° projected on a phosphor screen placed at part B is shown in Figure 3-3. The azimuthal rotation angle Φ is defined as the angle between the lens axis of hemispherical analyzer and X-axis of sample holder as shown in Figure 3-2 (f) and (g).

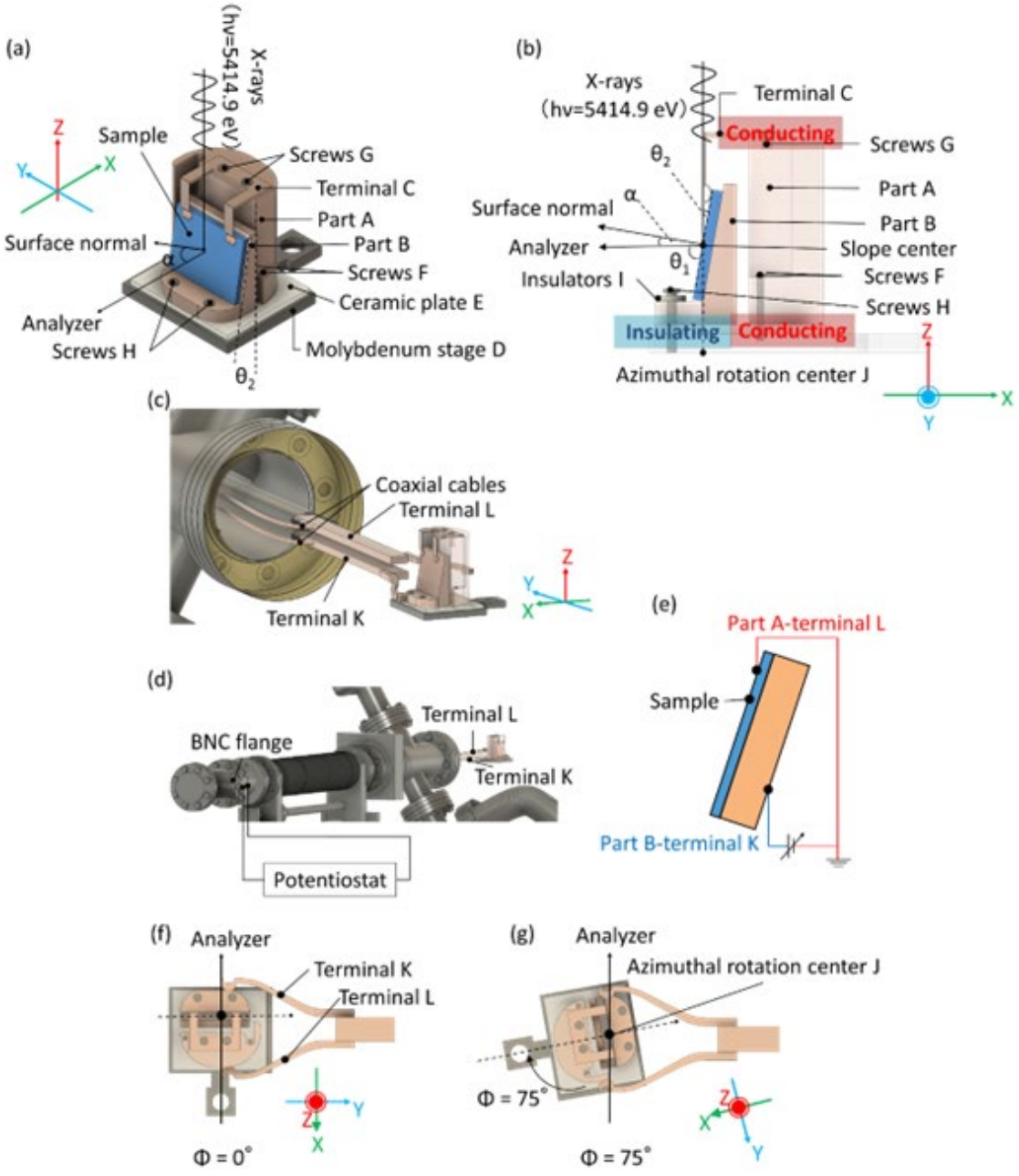

Figure 3-2. Schematic representations of the (a, b) sample holder, (c, d) bias application system, (f, g) top view of the sample holder and the terminals (terminal K and L) for a bias application and angle-resolved XPS. The azimuthal rotation angle is represented by Φ. Φ = (f) 0° and (g) 75°.

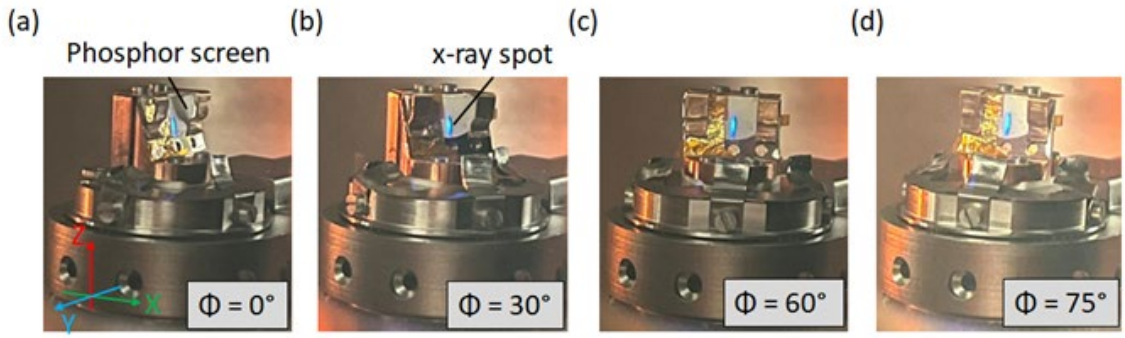

Figure 3-3 Photographs of x-ray irradiation area at various rotation angles Φ. Φ = (a) 0°, (b) 30°, (c) 60°, and (d) 75°.

3.3 Results

3.3.1 Application of DC voltages

The shift in the photoelectron peaks of the Au samples confirmed the application of a direct current (DC) bias voltage. Two pieces of Au foil (99.95%, Nilaco Co., Ltd.) (Foils 1 and 2) were pushed onto part B, as shown in Figure 3-4 (a). One foil was electrically connected to part B, while the other foil was insulated from part B by a polyimide film inserted between the foil 1 and part B but electrically connected to part A and a hemispherical analyzer through terminal C, as described in the Section 3.2. Foils 1 and 2 were denoted as the working electrode (WE) and counter electrode (CE), respectively. HAXPES measurements were performed in each circuit, as shown in Figure 3-4 (b) and (c), while external DC biases of -5, -2, 0, +2, and +5 V were applied to foil 2 versus foil 1. The binding energies of the photoelectron peaks at an applied bias of 0 V were

calibrated with respect to the Au $4f_{7/2}$ peak (84.0 eV) or Au $3d_{5/2}$ peak (2206.7 eV). The same calibration was applied to each spectrum at the applied bias of -5, -2, +2, and +5 V.

Figure 3-5 (a) shows the Au $3d_{5/2}$ photoelectron spectra obtained in the circuit where foil 1 (WE) was grounded with the hemispherical analyzer, while foil 2 (CE) was insulated from the hemispherical analyzer, as shown in Figure 3-4 (b). A peak corresponding to Au $3d_{5/2}$ was observed for the Au foil. The Au $3d_{5/2}$ peaks of foil 1 were identical under the bias conditions (Figure 3-5 (a) upper plot). In contrast, the peaks of foil 2 shifted owing to the applied bias (Figure 3-5 (a) lower plot). On the other hand, Figure 3-5 (b) shows the Au $3d_{5/2}$ photoelectron spectra obtained in the circuit where foil 1 (WE) was insulated from the hemispherical analyzer, while foil 2 (CE) was grounded to the hemispherical analyzer, as shown in Figure 3-4 (c). The Au $3d_{5/2}$ peaks of the foil 1 shifted owing to the applied bias (Figure 3-5 (b), upper plot). In contrast, the peaks of foil 2 were identical under the bias conditions (Figure 3-5 (b), lower plot). In addition, the Au 4f photoelectron peaks exhibited a similar shift under bias conditions, as shown in Figure 3-6. In both circuits, the peak positions of the Au foil grounded to the hemispherical analyzer remained unchanged under the bias conditions, while those of Au foil insulated from the hemispherical analyzer shifted, corresponding to the applied bias and its polarity. Thus, it was demonstrated that the sample holder and bias application

system enabled us to apply biases from outside the analysis chamber to samples retained under vacuum conditions.

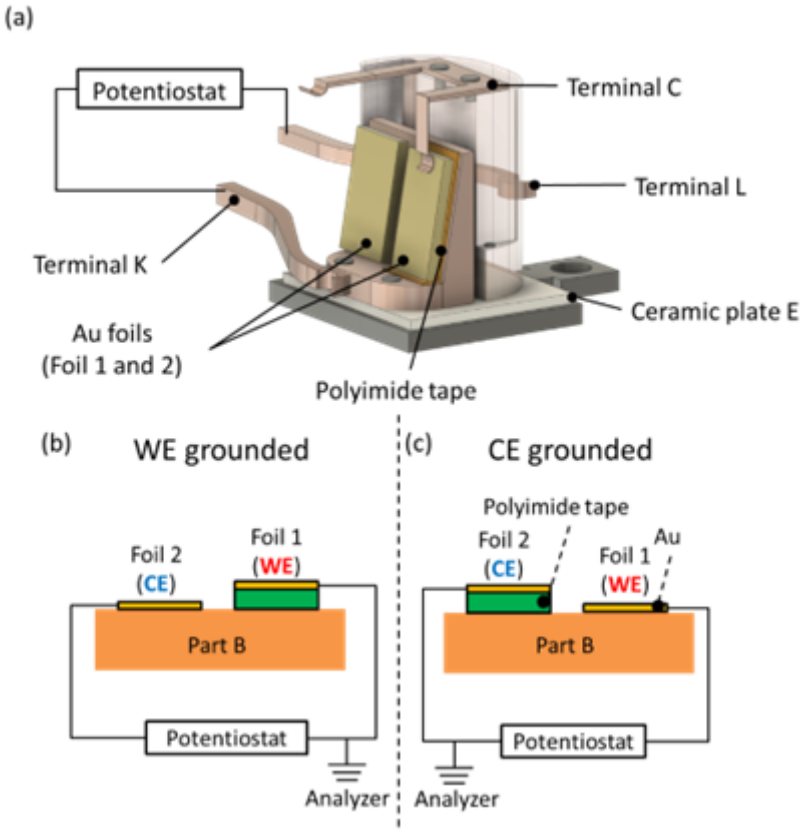

Figure 3-4. (a) A schematic illustration of the bias application system for HAXPES. Simplified schematic representations of the two electrical circuits: (b) the working electrode (WE) or (c) the counter electrode (CE) grounded to the hemispherical analyzer.

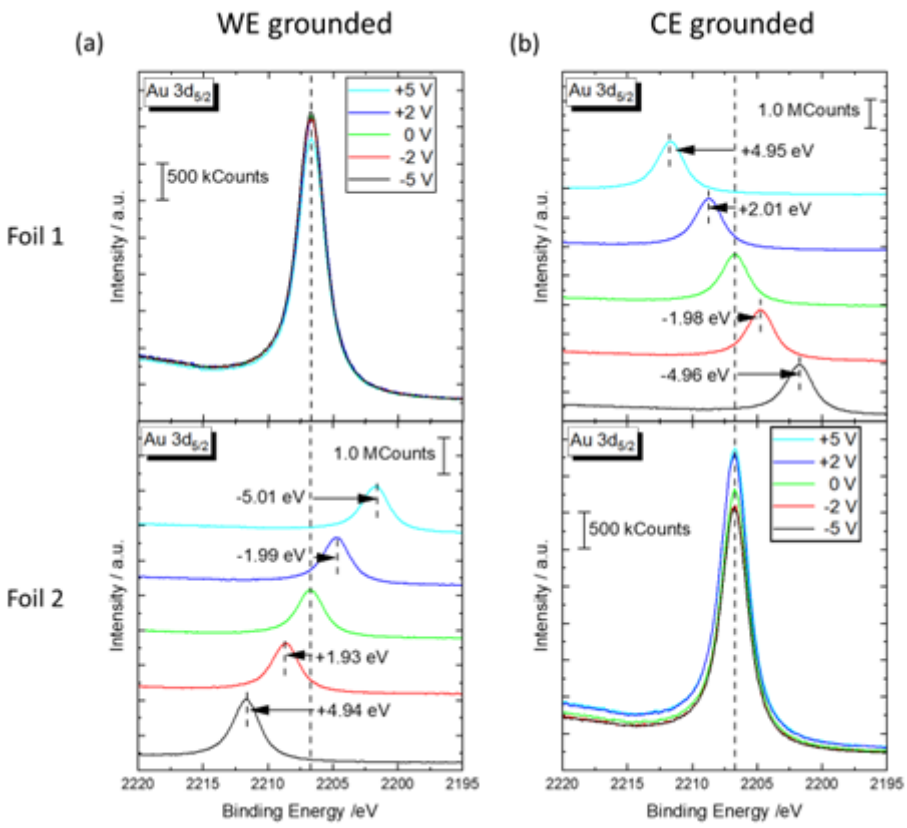

Figure 3-5. Au $3d_{5/2}$ photoelectron spectra under bias application in two electrical circuits: (a) WE and (b) CE grounded to the hemispherical analyzer. The dashed lines in the graphs indicate the binding energies of the Au $3d_{5/2}$ peaks at 2206.7 eV, determined by curve fitting using the Voigt function after Shirly background subtraction.

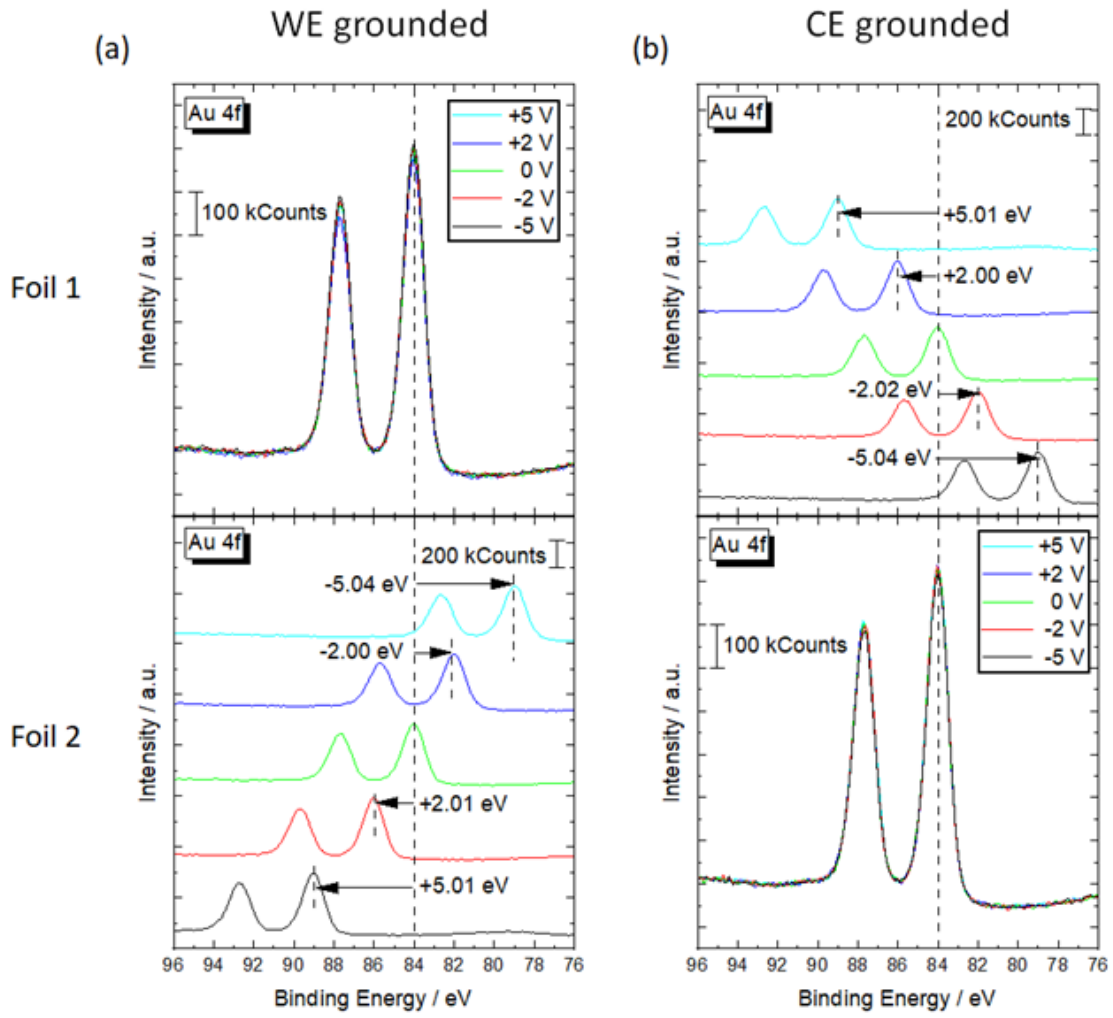

Figure 3-6. Au 4f photoelectron spectra under bias application in two electrical circuits: (a) WE and (b) CE grounded to the hemispherical analyzer. The dashed lines in the graphs indicate the binding energies of the Au $4f_{7/2}$ peaks at 84.0 eV, determined by curve fitting using the Voigt function after Shirly background subtraction.

3.3.2 Calculations of a SiO_2 layer thickness using angle-resolved measurements

The thickness of SiO_2 film formed on a Si substrate was estimated by the relative area of the photoelectron peaks corresponding to the SiO_2 and Si measured at different take-off angles (TOAs) α and the physical properties of those materials. The estimated thicknesses were compared with those determined by ellipsometry.

Figure 3-7 shows Si 2p and Si 1s photoelectron spectra at α of 15°, 33°, 61°, and 76° corresponding to the azimuthal rotation angles Φ of 0°, 30°, 60°, and 75°, respectively. The binding energy was calibrated with respect to the C 1s peaks corresponding to hydrocarbon species (285.0 eV). As α increased, the intensity ratio of bulk Si peak to SiO_2 peak decreased in both Si 2p and Si 1s regions. The peaks corresponding to the Si substrate were not observed in Si 2p and Si 1s regions at α of 61.2°, confirming that more surface-sensitive photoelectron spectra were obtained at higher α.

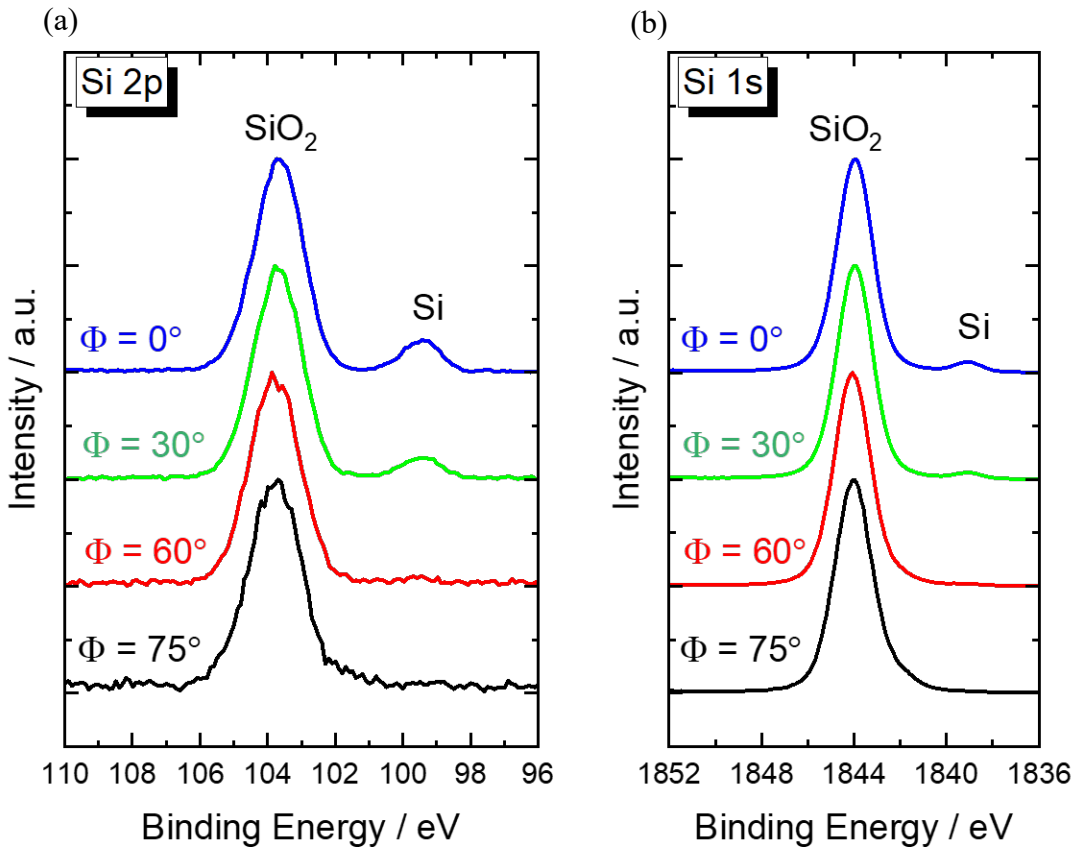

Figure 3-7. (a) Si 2p, (b) Si 1s photoelectron spectra generated from Si substrate with its oxide layer at the azimuthal angle Φ of 0°, 30°, 60° and 75°.

The thickness of the SiO_2 layer formed on the Si was determined using the following equation.[13, 16, 21]

$$d = \lambda_{SiO_2} \cos\alpha \ln\left[\frac{I_{SiO_2}}{I_{Si}} \frac{N_{Si}\lambda_{Si}}{N_{SiO_2}\lambda_{SiO_2}} + 1\right] \quad (2)$$

where λ_{SiO_2} and λ_{Si} are the inelastic mean free paths (IMFPs) of the Si 2p and Si 1s photoelectrons in the SiO_2 layer and the Si substrate, respectively, obtained using the TPP-2M formula.[22-24] N_{SiO_2} and N_{Si} are the Si atomic densities of the SiO_2 layer and Si

substrate,[25] and I_{SiO_2} and I_{Si} are the photoelectron intensities of the SiO_2 peak and Si peak in the Si 2p and Si 1s regions. In the Si 2p region, the kinetic energies of photoelectrons generated from the SiO_2 layer and Si substrate by x-rays from the Cr-Kα source are 5308 and 5312 eV, respectively, and corresponding IMFPs are 11.7 and 9.93 nm, respectively. Similarly, in the Si 1s region, those of photoelectrons generated from the SiO_2 layer and Si substrate are 3567 and 3572 eV, respectively, and corresponding IMFPs are 8.39 and 6.69 nm, respectively. Consequently, the estimated thickness of SiO_2 thin film was 29.8 nm (Table 3-1), that is 17.4% thicker than that estimated by ellipsometry. The error was within an uncertainty of 10 – 20% arising from the IMFPs values of photoelectrons calculated by the TPP-2M equation.[21, 24] It was therefore demonstrated that the sample holder was capable of angle-resolved measurements.

Table 3-1. SiO_2 film thickness calculated from the strength ratio of SiO_2 and Si.

Orbitals	Azimuthal rotation angle : Φ (°)	TOAs : α (°)	AR-XPS (nm)	Ellipsometry / nm
Si 2p	0	15	29.6	25.5±0.298
Si 2p	15	33	28.9	
Si 1s	0	15	30.3	
Si 1s	15	33	30.3	

3.4 Conclusion

In conclusion, we developed the laboratory-based HAXPES apparatus equipped with the functions of bias application and angle-resolved measurements. In the demonstrations of bias application function using Au foils, the Au 4f and Au $3d_{5/2}$ photoelectron peaks shifted corresponding to the applied bias and its polarity. In addition, the thickness of the SiO_2 layer formed on the Si substrate was estimated with an error of 17.4% using a peak intensity ratio of the SiO_2 and the Si by angle-resolved measurements. The system reported in the present paper is expected to be applied for nondestructively analyzing the electronic states and chemical structures not only for bulk electrode materials[10] but also for electrode/electrolyte interfaces in all-solid-state Li-ion batteries to clarify the origin of the ion transport resistance such as a heterogeneous interphase formed by the mutual ion diffusion[26] and space charge layer formed by the difference in the chemical potential.[27]

References

(1) Yamashita, Y.; Chikyow, T. Origin of Fermi level pinning in high-k gate stack structures studied by operando hard x-ray photoelectron spectroscopy. *J. Electron. Spectrosc. Relat. Phenom.* **2020**, *238*, 146890. DOI: 10.1016/j.elspec.2019.146890.

(2) Kakushima, K.; Okamoto, K.; Tachi, K.; Song, J.; Sato, S.; Kawanago, T.; Tsutsui, K.; Sugii, N.; Ahmet, P.; Hattori, T.; et al. Observation of band bending of metal/high-k Si capacitor with high energy x-ray photoemission spectroscopy and its application to interface dipole measurement. *J. Appl. Phys.* **2008**, *104* (10), 104908. DOI: 10.1063/1.3021461.

(3) Walsh, L. A.; Hughes, G.; Lin, J.; Hurley, P. K.; O'Regan, T. P.; Cockayne, E.; Woicik, J. C. Hard x-ray photoelectron spectroscopy and electrical characterization study of the surface potential in metal/Al_2O_3/GaAs(100) metal-oxide-semiconductor structures. *Physical Review B: Condensed Matter and Materials Physics* **2013**, *88* (4), 045322. DOI: 10.1103/PhysRevB.88.045322.

(4) Liu, Y.; Sun, Q.; Liu, J.; Banis, M. N.; Zhao, Y.; Wang, B.; Adair, K.; Hu, Y.; Xiao, Q.; Zhang, C.; et al. Variable-Energy Hard X-ray Photoemission Spectroscopy: A Nondestructive Tool to Analyze the Cathode–Solid-State Electrolyte Interface. *ACS Applied Materials & Interfaces* **2020**, *12* (2), 2293-2298. DOI: 10.1021/acsami.9b16343.

(5) Yamashita, Y.; Ohmori, K.; Ueda, S.; Yoshikawa, H.; Chikyow, T.; Kobayashi, K. Bias-voltage Application in Hard X-Ray Photoelectron Spectroscopy for Characterization of Advanced Materials. *e-Journal of Surface Science and Nanotechnology* **2010**, *8*, 81-83. DOI: 10.1380/ejssnt.2010.81.

(6) Ohta, A.; Murakami, H.; Ikeda, M.; Makihara, K.; Ikenaga, E.; Miyazaki, S.

Potential changes and chemical bonding features for Si-MOS structure as evaluated from HAXPES analysis. *Microelectron. Eng.* **2017**, *178*, 80-84. DOI: 10.1016/j.mee.2017.05.002.

(7) Kiuchi, H.; Hikima, K.; Shimizu, K.; Kanno, R.; Toshiharu, F.; Matsubara, E. Operando hard X-ray photoelectron spectroscopy of $LiCoO_2$ thin film in an all-solid-state lithium ion battery. *Electrochem. Commun.* **2020**, *118*, 106790. DOI: 10.1016/j.elecom.2020.106790.

(8) Hikima, K.; Shimizu, K.; Kiuchi, H.; Hinuma, Y.; Suzuki, K.; Hirayama, M.; Matsubara, E.; Kanno, R. Reaction Mechanism of Li_2MnO_3 Electrodes in an All-Solid-State Thin-Film Battery Analyzed by Operando Hard X-ray Photoelectron Spectroscopy. *Journal of the American Chemical Society* **2022**, *144* (1), 236-247. DOI: 10.1021/jacs.1c09087 From NLM PubMed-not-MEDLINE.

(9) Hikima, K.; Shimizu, K.; Kiuchi, H.; Hinuma, Y.; Suzuki, K.; Hirayama, M.; Matsubara, E.; Kanno, R. Operando analysis of electronic band structure in an all-solid-state thin-film battery. *Communications Chemistry* **2022**, *5* (1), 52. DOI: 10.1038/s42004-022-00664-w From NLM PubMed-not-MEDLINE.

(10) Iwama, T.; Ohnishi, T.; Masuda, T. Operando Observation of Lithiation and Delithiation Reactions of a $LiCoO_2$-Li_3BO_3 Composite Electrode Formed on a $Li_{6.6}La_3Zr_{1.6}Ta_{0.4}O_{12}$ Solid Electrolyte Sheet by Laboratory-based Hard X-ray Photoelectron Spectroscopy. *Electrochemistry* **2023**, *91* (11), 117005. DOI: 10.5796/electrochemistry.23-00090.

(11) Huang, R.; Liu, T.; Zhao, Y.; Zhu, Y.; Huang, Z.; Li, F.; Liu, J.; Zhang, L.; Zhang, S.; Dingsun, A.; et al. Angular dependent XPS study of surface band bending on Ga-polar n-GaN. *Appl. Surf. Sci.* **2018**, *440*, 637-642. DOI:

10.1016/j.apsusc.2018.01.196.

(12) Nagamura, N.; Horiba, K.; Toyoda, S.; Kurosumi, S.; Shinohara, T.; Oshima, M.; Fukidome, H.; Suemitsu, M.; Nagashio, K.; Toriumi, A. Direct observation of charge transfer region at interfaces in graphene devices. *Appl. Phys. Lett.* **2013**, *102* (24). DOI: 10.1063/1.4808083.

(13) Strohmeier, B. R. An ESCA method for determining the oxide thickness on aluminum alloys. *Surf. Interface Anal.* **1990**, *15* (1), 51-56. DOI: 10.1002/sia.740150109.

(14) Horiba, K.; Nakamura, Y.; Nagamura, N.; Toyoda, S.; Kumigashira, H.; Oshima, M.; Amemiya, K.; Senba, Y.; Ohashi, H. Scanning photoelectron microscope for nanoscale three-dimensional spatial-resolved electron spectroscopy for chemical analysis. *Rev. Sci. Instrum.* **2011**, *82* (11), 113701. DOI: 10.1063/1.3657156 From NLM Medline.

(15) Fadley, C. S.; Shirley, D. A. Electronic densities of states from x-ray photoelectron spectroscopy. *J. Res. Natl. Bur. Stand. Sec. A* **1970**, *74A* (4), 543. DOI: 10.6028/jres.074a.045.

(16) Endo, R.; Ohnishi, T.; Takada, K.; Masuda, T. In Situ Observation of Lithiation and Delithiation Reactions of a Silicon Thin Film Electrode for All-Solid-State Lithium-Ion Batteries by X-ray Photoelectron Spectroscopy. *J. Phys. Chem. Lett* **2020**, *11* (16), 6649-6654. DOI: 10.1021/acs.jpclett.0c01906 From NLM PubMed-not-MEDLINE.

(17) Endo, R.; Ohnishi, T.; Takada, K.; Masuda, T. Instrumentation for tracking electrochemical reactions by x-ray photoelectron spectroscopy under conventional vacuum conditions. *Journal of Physics Communications* **2021**, *5* (1), 015001. DOI:

10.1088/2399-6528/abd617.

(18) Endo, R.; Ohnishi, T.; Takada, K.; Masuda, T. Electrochemical Lithiation and Delithiation in Amorphous Si Thin Film Electrodes Studied by Operando X-ray Photoelectron Spectroscopy. *J. Phys. Chem. Lett* **2022**, *13* (31), 7363-7370. DOI: 10.1021/acs.jpclett.2c01312 From NLM PubMed-not-MEDLINE.

(19) Kalha, C.; Fernando, N. K.; Bhatt, P.; Johansson, F. O. L.; Lindblad, A.; Rensmo, H.; Medina, L. Z.; Lindblad, R.; Siol, S.; Jeurgens, L. P. H.; et al. Hard x-ray photoelectron spectroscopy: a snapshot of the state-of-the-art in 2020. *J. Phys.: Condens. Matter* **2021**, *33*, 233001. DOI: 10.1088/1361-648X/abeacd.

(20) Siol, S.; Mann, J.; Newman, J.; Miyayama, T.; Watanabe, K.; Schmutz, P.; Cancellieri, C.; Jeurgens, L. P. H. Concepts for chemical state analysis at constant probing depth by lab-based XPS/HAXPES combining soft and hard X-ray sources. *Surf. Interface Anal.* **2020**, *52* (12), 802-810. DOI: 10.1002/sia.6790.

(21) Seah, M. P.; Spencer, S. J.; Bensebaa, F.; Vickridge, I.; Danzebrink, H.; Krumrey, M.; Gross, T.; Oesterle, W.; Wendler, E.; Rheinländer, B.; et al. Critical review of the current status of thickness measurements for ultrathin SiO_2 on Si Part V: Results of a CCQM pilot study. *Surf. Interface Anal.* **2004**, *36* (9), 1269-1303. DOI: 10.1002/sia.1909.

(22) Tanuma, S.; Powell, C. J.; Penn, D. R. Calculations of electron inelastic mean free paths. V. Data for 14 organic compounds over the 50-2000 eV range. *Surf. Interface Anal.* **1994**, *21* (3), 165-176. DOI: 10.1002/sia.740210302.

(23) Tanuma, S.; Powell, C. J.; Penn, D. R. Calculations of Electron Inelastic Mean Free Paths (IMFPs)

Ⅵ. Analysis of the Gries Inelastic Scattering Model and Predictive IMFP Equation.

Surf. Interface Anal. **1997**, *25*, 25.

(24) Tanuma, S.; Powell, C. J.; Penn, D. R. Calculations of electron inelastic mean free paths. IX. Data for 41 elemental solids over the 50 eV to 30 keV range. *Surf. Interface Anal.* **2011**, *43* (3), 689-713. DOI: 10.1002/sia.3522.

(25) Himpsel, F. J.; McFeely, F. R.; Taleb-Ibrahimi, A.; Yarmoff, J. A.; Hollinger, G. Microscopic structure of the SiO_2/Si interface. *Physical Review B: Condensed Matter and Materials Physics* **1988**, *38* (9), 6084-6096. DOI: 10.1103/physrevb.38.6084 From NLM PubMed-not-MEDLINE.

(26) Kim, K. H.; Iriyama, Y.; Yamamoto, K.; Kumazaki, S.; Asaka, T.; Tanabe, K.; Fisher, C. A. J.; Hirayama, T.; Murugan, R.; Ogumi, Z. Characterization of the interface between $LiCoO_2$ and $Li_7La_3Zr_2O_{12}$ in an all-solid-state rechargeable lithium battery. *J. Power Sources* **2011**, *196* (2), 764-767. DOI: 10.1016/j.jpowsour.2010.07.073.

(27) Takada, K.; Ohta, N.; Zhang, L.; Xu, X.; Hang, B. T.; Ohnishi, T.; Osada, M.; Sasaki, T. Interfacial phenomena in solid-state lithium battery with sulfide solid electrolyte. *Solid State Ionics* **2012**, *225*, 594-597. DOI: 10.1016/j.ssi.2012.01.009.

4. Electrochemical Reactions of $LiCoO_2$-Li_3BO_3 Composite Cathodes

4.1 Introduction

$LiCoO_2$ (LCO) is a widely used cathode material in conventional liquid-type lithium-ion batteries (LIBs) due to its relatively high theoretical capacity of 274 mAh g^{-1} and superior cycle performance.[1, 2] As mentioned in Chapter 1, changes in crystal structure and electronic states after charge/discharge cycles have been well-studied. It is known that high-voltage operations to 4.2 V or more positive result in capacity rapidly fading due to the irreversible structural and electronic changes.[3-9] However, the mechanism of capacity fading have not been fully clarified because it involves various complex phenomena such as decomposition of electrolytes,[10] Co dissolution,[11] and reduction of Co^{3+} to Co^{2+} ions[12] in liquid systems.

Electrochemical reactions of LCO electrodes in an all-solid-state battery configuration were explored by various research groups.[13-17] For example, Park et al. constructed a $LiCoO_2$-Li_3BO_3 (LCO-LBO) composite cathode on a $Li_{6.6}La_3Zr_{1.6}Ta_{0.4}O_{12}$ (LLZT) by using co-sintering to yield a half cell with a LCO-LBO/LLZT/Li configuration and demonstrated a stable capacity retention without significant side reactions at the

interfaces of LCO, LBO, and LLZT in a potential range of 2.5 – 4.4 V vs. Li^+/Li.[16] Jang et al. further studied electrochemical responses of a LCO thin film constructed on lithium phosphorus oxynitride electrolyte (LiPON) in LCO/LiPON/Li configuration by radio frequency magnetron sputtering. They showed that capacity retention is stable for charge/discharge cycles up to 4.4 V or less positive, whereas it drastically decays for charge/discharge cycles up to 4.45 V or more positive.[17] Ohnishi et al. constructed a LCO/Li_3PO_4/Li-configured epitaxially grown LCO thin film on the sapphire (0001) plane with the (001) orientation, and investigated the crystal structure and cyclability under high-voltage operations using *in situ* x-ray diffraction (XRD) and electrochemical impedance spectroscopy (EIS). They revealed that the transformation from H3 phase to H1-3 phase under high-voltage charging causes irreversible increase in the electronic resistance, leading to reduction of the cyclability.[13]

In the present study, a LCO-LBO composite cathode layer of LCO-LBO mixture was formed on a LLZT solid electrolyte sheet precoated with a Nb or Ta thin layer in LCO-LBO/Nb or Ta/LLZT/Li configuration and its electrochemical behavior was investigated with different voltage range using a laboratory-based *operando* HAXPES apparatus shown in Chapter 3.

4.2 Results and Discussion

4.2.1 Charge/discharge cycles in a potential range from 3.0 – 4.2 V

4.2.1.1 Structural analysis of surface and cross-section of LCO-LBO/LLZT/Li cell

Figure 4-1 and Figure 4-2 and show surface and cross-sectional scanning electron microscopy (SEM) images and energy dispersive spectroscopy (EDS) maps of the LCO-LBO composite cathode. The size of primary LCO particles is around 200 nm and those are interconnected by LBO distributed in the composite cathode. LBO is uniformly distributed in the entire composite electrode, but some LBO is segregated on the top and bottom of the composite electrode. We denote such LCO-LBO composite cathode as LCO-LBO composite cathode with segregation in this paper.

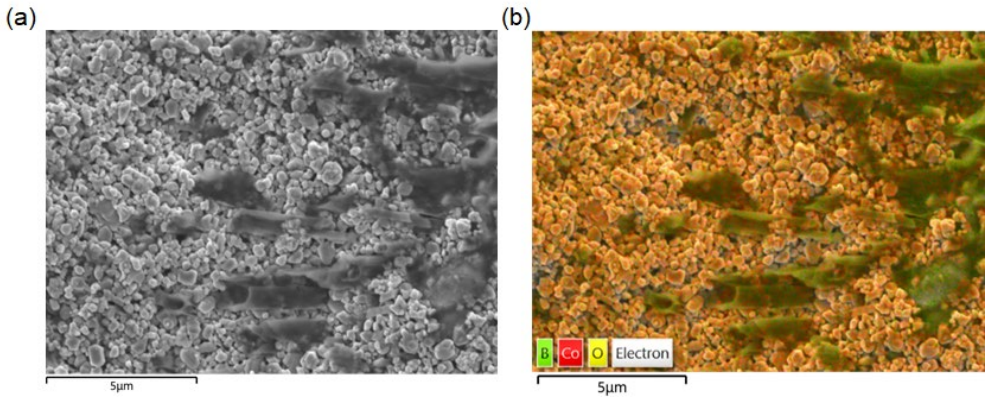

Figure 4-1. (a) A SEM image and (b) EDS map of LCO-LBO composite cathode in top view.

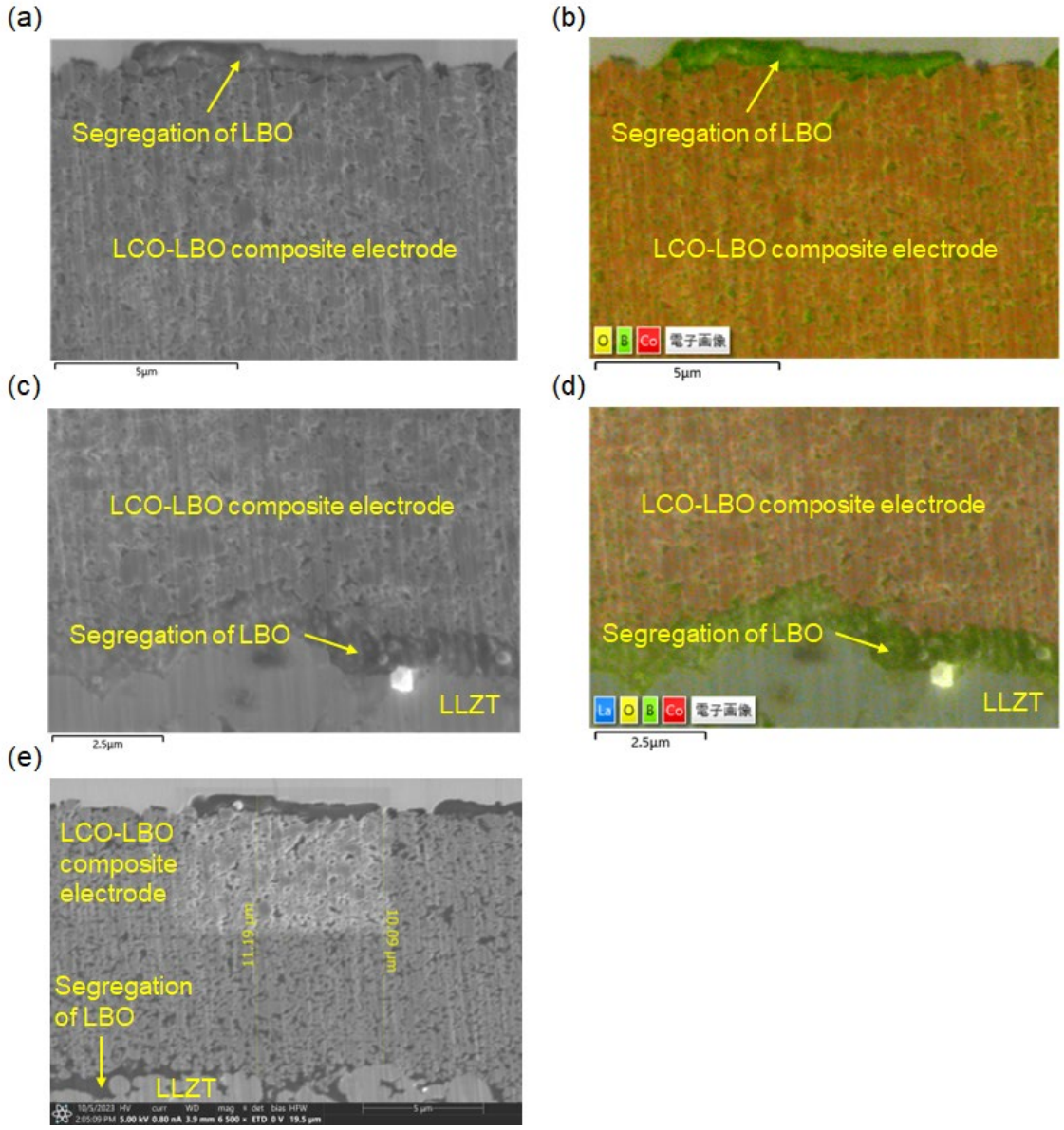

Figure 4-2. Cross-sectional (a, c, e) SEM images and (b, d) EDS maps of the LCO-LBO composite cathode. (a, b) The top side (outermost side), (c, d) bottom side (LLZT side) and (e) entire LCO-LBO composite cathode.

4.2.1.2 Charge and discharge characteristics

Figure 4-3 (a) and (b) shows typical galvanostatic charge/discharge potential profiles, cycle performance, and corresponding Coulombic efficiency of the all-solid-state (ASS)

cell. In the first a few charge/discharge cycles, capacities for charging are somewhat larger than those of successive discharging. The charge integrations of the first charging and successive discharging were 121 mAh g^{-1} and 83.3 mAh g^{-1}, respectively, with a Coulombic efficiency of 69.1%. Those in the second charging and discharging were 99.8 mAh g^{-1} and 85.2 mAh g^{-1}, respectively, with a Coulombic efficiency of 85.4%. We denote such initial irreversible cycles as conditioning. The irreversible capacity loss during the conditioning cycles should be due to the anodic instability of LLZT[18, 19] and/or irreversible reaction characteristic to low temperature LCO formed by wet chemical process, followed by annealing.[20] After the conditioning, galvanostatic potential profiles become reversible; with a capacity of ~85 mAh g^{-1} and a Coulombic efficiency of ~100%.

A characteristic plateau corresponding to the $Co^{3+/4+}$ accompanying with lithiation/delithiation of LCO at the potential of ~3.9 V *vs*. Li^+/Li was observed, confirming the reversible redox reaction.[21,22] The capacity and Coulombic efficiency of the present ASS cell were higher than those of previous report on LBO-free LCO cathode layer directly formed on a garnet-type solid electrolyte[16] and LCO-LBO composite electrode,[16] confirming the role of Li^+ ion conducting LBO interlayer at the LCO/LLZT interfaces.[16] As shown in Figure 4-2, part of LBO was segregated on the top and bottom of composite cathode layer. The charge/discharge capacity after conditioning cycles is

around 85 mAh g^{-1} (Figure 4-3), which is 62% of theoretical capacity of LCO, 137 mAh g^{-1}. The ratio of active LCO is still higher than that reported previously by other group.[16] However, such segregation is considered as the origin of inactive LCO.

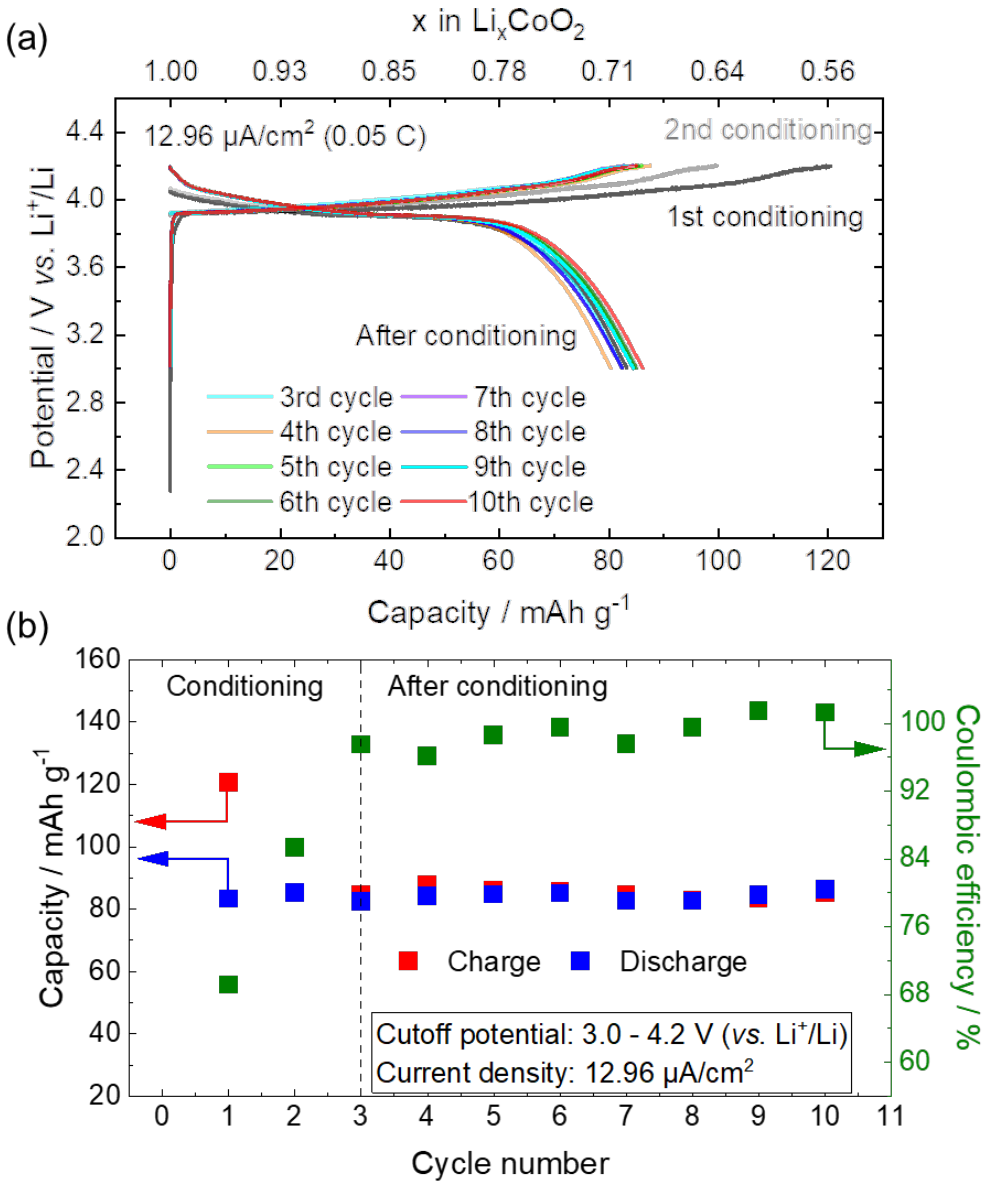

Figure 4-3. (a) Galvanostatic charge/discharge potential profiles, (b) cycle performance and corresponding Coulombic efficiency of the ASS cell.

4.2.1.3 Static observations of electrochemical reactions of LCO-LBO composite electrode

Figure 4-4 shows the Co $2p_{3/2}$ and B 1s photoelectron spectra of the LCO-LBO composite cathode with segregation before and after conditioning cycles. In the photoelectron spectra without calibration (Figure 4-4 (a) and Figure 4-4 (b)), the Co $2p_{3/2}$ peak shifted by 0.5 eV to a lower binding energy from the pristine to first charged state although the Pt thin layer (current collector) deposited on LCO-LBO composite cathode was grounded to the hemispherical analyzer. This shift is attributed to the change in valence state of LCO due to the transition from a p-type semiconducting to a metallic state induced by delithiation.[14] After the first charging, the position of Co $2p_{3/2}$ peak remained unchanged because the Fermi level of LCO, Pt and hemispherical analyzer were aligned.

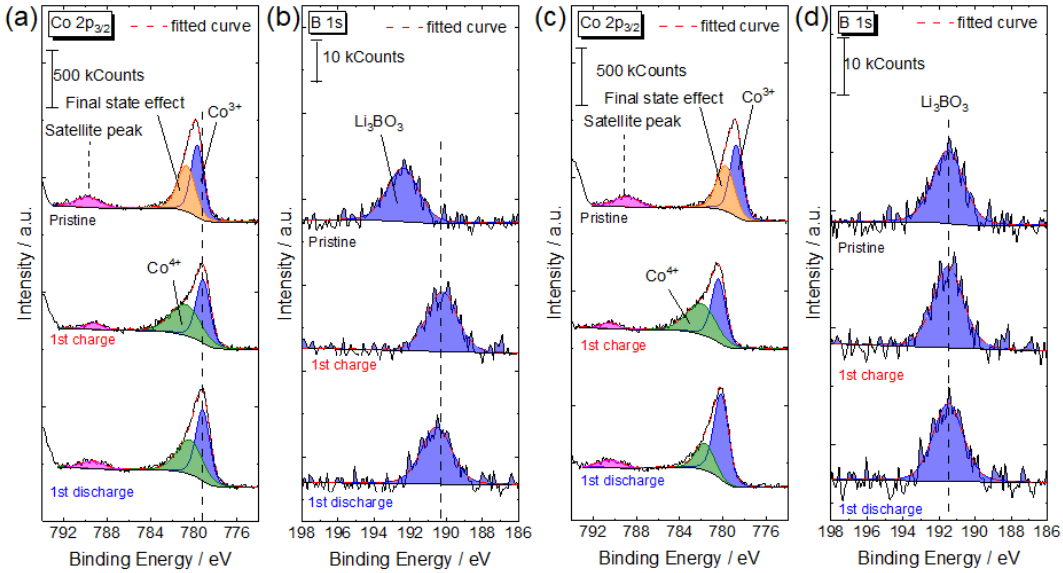

Figure 4-4. Co $2p_{3/2}$ and B 1s photoelectron spectra of the LCO-LBO composite cathode with segregation before and after charge/discharge cycles (a, b) without and (c, d) with calibration using the B 1s peak of LBO at 191.5 eV.

Here, photoelectron spectra (Co $2p_{3/2}$, B 1s, C 1s, and Li 1s) of the LCO-LBO composite cathode with segregation before and after charge/discharge cycles without calibration, calibrated by the B 1s peak of LBO at 191.5 eV, the Co^{3+} peak of LCO at 780.0 eV, the C 1s peak of hydrocarbon at 285.0 eV, and the Li 1s peak of LBO/LCO/Li_2CO_3 at 54.5 eV are shown in Figure 4-5, Figure 4-6, Figure 4-7, Figure 4-8, and Figure 4-9, respectively to compare their respective spectra using each component as a standard. Among their standards, B 1s peak at 191.5 eV is considered to be suitable because the electrochemical potential of electron in bulk electrolyte should be constant.[23]

Although the potential distribution occurs in the electric double layer (EDL) at the electrode/electrolyte interfaces, thickness of EDL, in the range of ~10 nm,[24] should be much smaller than the size of primary LBO particles, that is in the sub-micrometer range as imaged by SEM (Figure 4-1). Thus, hereafter, all the spectra obtained from the LCO-LBO composite cathode with segregation were calibrated using B 1s peak of LBO at 191.5 eV as a standard (Figure 4-4 (c) and (d)).

In the Co $2p_{3/2}$ region (Figure 4-4 (c)), a sharp main peak and a broad satellite peak characteristic to LCO were observed at around 780 eV and 790 eV, respectively.[7, 14, 25] The main peak can be deconvoluted into two peaks at around 780 eV and 781 eV attributed to Co^{3+} ions of the LCO and final state effect,[7] respectively. After the 1st charging, the main peak was asymmetrically broadened toward a higher binding energy due to the appearance of Co^{4+} peak overlapping with the component attributed to the final state effect, with maintaining the Co^{3+} peak unchanged (Figure 4-4 (c)). It is noted that the Co^{4+} peak cannot be deconvoluted from that of final state effect because their peak positions are very close to each other. Furthermore, the relative areas of satellite peak decreased (Figure 4-4 (c)), confirming the oxidation of Co^{3+} to Co^{4+} ions.[7, 14]

After the subsequent discharging, those observed changes were recovered; the full width half maximum (FWHM) of Co^{4+} peak decreased and the relative areas of satellite

peak increased (Figure 4-4 (c)), confirming that the Co^{4+} ions were reversibly reduced to Co^{3+} ions. The FWHMs of Co^{4+} peak and relative area of satellite peak were repeatedly changed in response to the successive charge/discharge cycles, suggesting the reversible oxidation-reductions of Co ions in LCO. The shape and intensity of B 1s peak corresponding to LBO were almost unchanged before and after charge/discharge cycles (Figure 4-4 (d)), showing that it serves as a bulk electrolyte in the composite electrode layer.

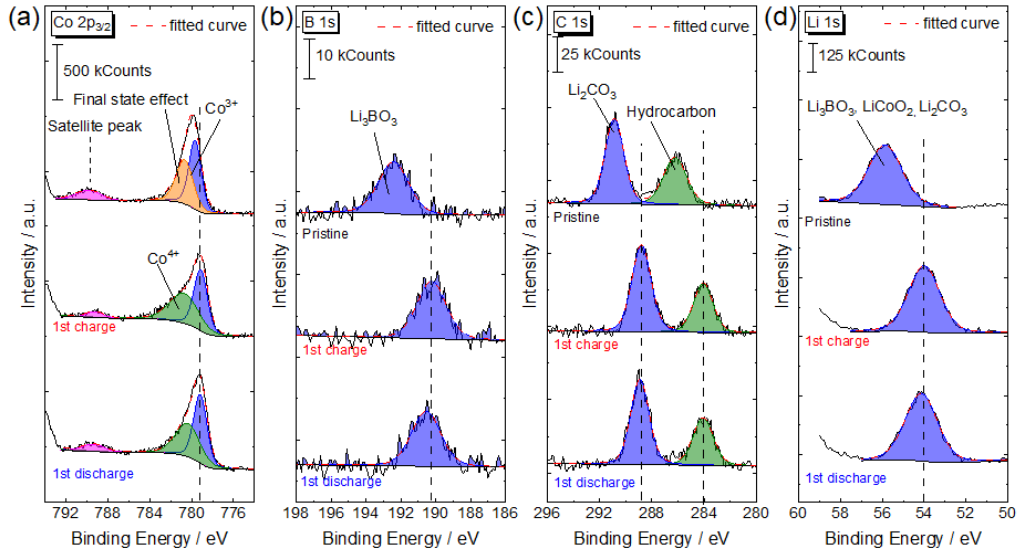

Figure 4-5. (a) Co $2p_{3/2}$, (b) B 1s, (c) C 1s, and (d) Li 1s photoelectron spectra of the LCO-LBO composite cathode with segregation before and after charge/discharge cycles without calibration.

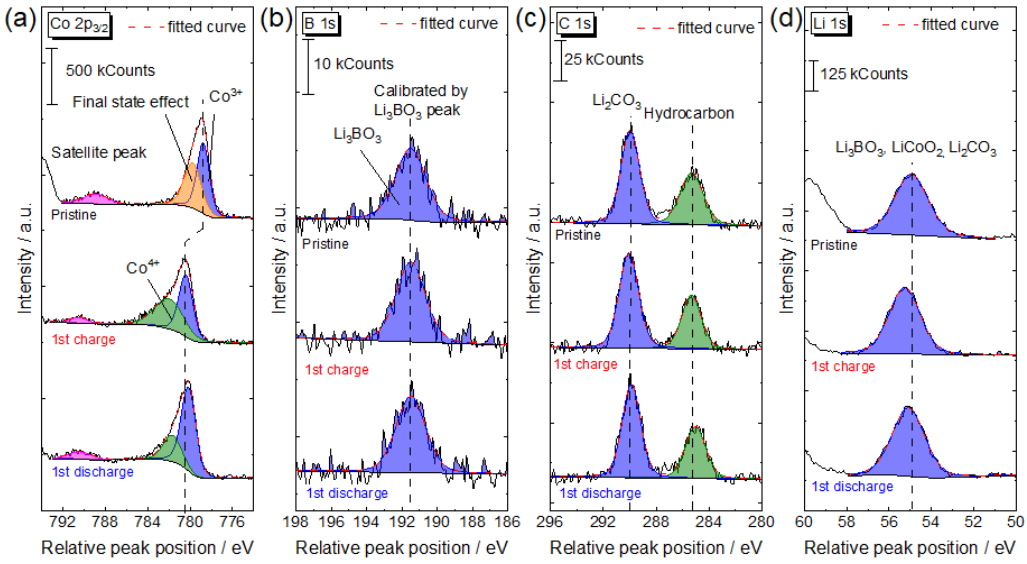

Figure 4-6. (a) Co $2p_{3/2}$, (b) B 1s, (c) C 1s, and (d) Li 1s photoelectron spectra of the LCO-LBO composite cathode with segregation before and after charge/discharge cycles with calibration using the B 1s peak of LBO at 191.5 eV.

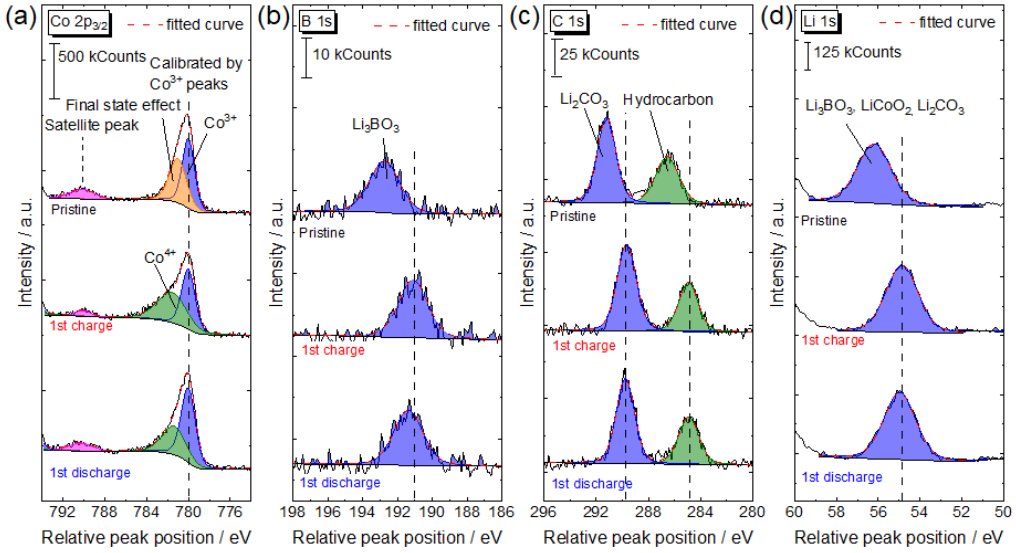

Figure 4-7. (a) Co $2p_{3/2}$, (b) B 1s, (c) C 1s, and (d) Li 1s photoelectron spectra of the LCO-LBO composite cathode with segregation before and after charge/discharge cycles with calibration using the Co^{3+} peak of LCO at 780.0 eV.

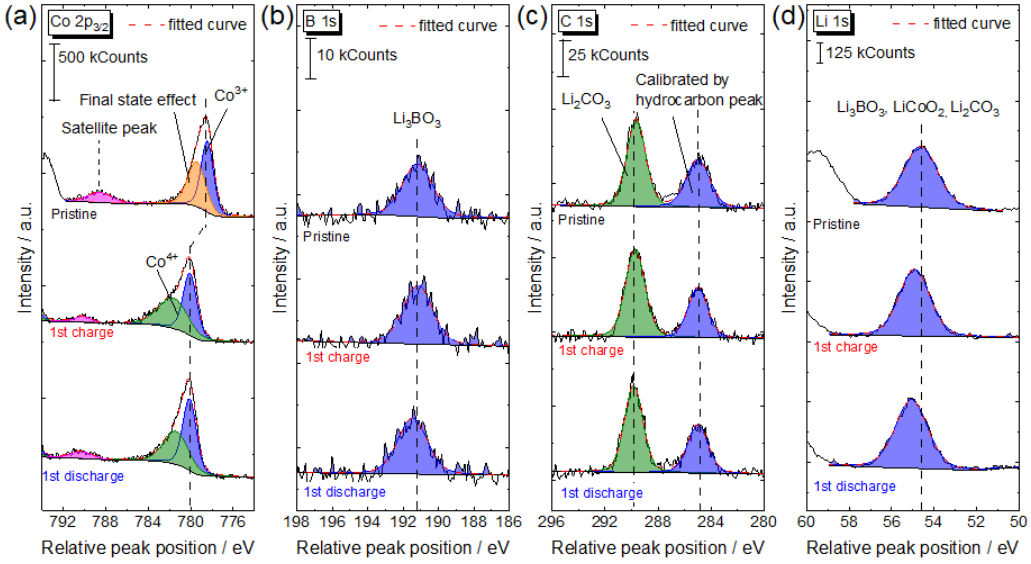

Figure 4-8. (a) Co $2p_{3/2}$, (b) B 1s, (c) C 1s, and (d) Li 1s photoelectron spectra of the LCO-LBO composite cathode with segregation before and after charge/discharge cycles with calibration using the C 1s peak of hydrocarbon at 285.0 eV.

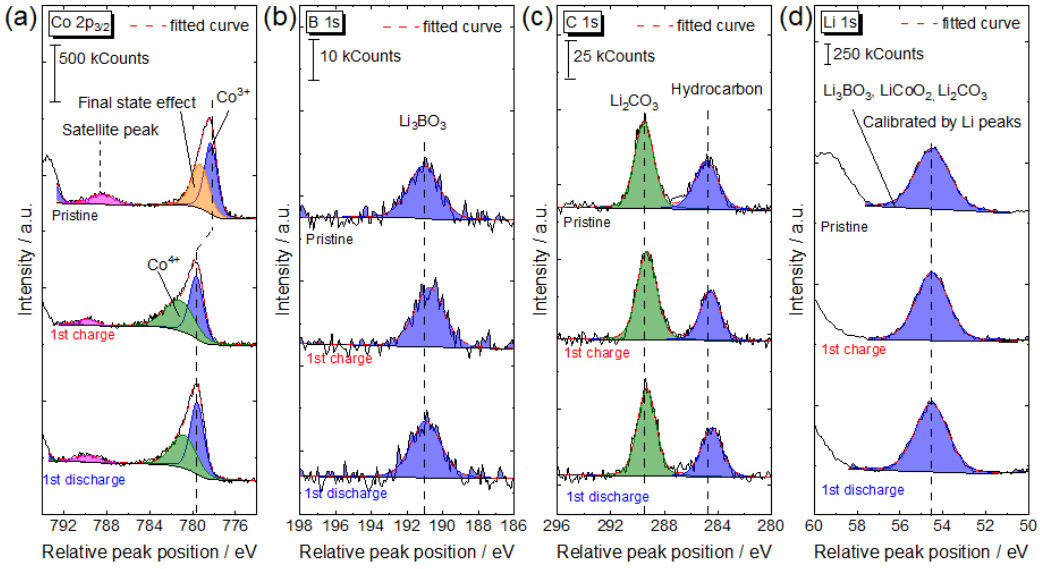

Figure 4-9. (a) Co $2p_{3/2}$, (b) B 1s, (c) C 1s, and (d) Li 1s photoelectron spectra of the LCO-LBO composite cathode with segregation before and after charge/discharge cycles with calibration using the Li 1s peak of LBO/LCO/Li_2CO_3 at 54.5 eV.

4.2.1.4 Dynamic observations of electrochemical reactions of LCO-LBO composite electrode

Figure 4-10 shows the time course of photoelectron spectra in the B 1s and Co $2p_{3/2}$ regions of LCO-LBO composite cathode repeatedly measured throughout the charge/discharge cycles after conditioning. Upon charging, Co^{4+} peak and the satellite peak started to broaden and decrease, respectively, due to the oxidation of Co^{3+} ions as observed in static HAXPES measurements (Figure 4-4). Those changes became more prominent with increase in the capacity. In addition to the broadening of Co^{4+} peak and decrease of satellite peak, the positions of the Co^{3+} and Co^{4+} peaks shifted to a higher binding energy consistently with the cell voltage, i.e., the electrode potential of a Pt thin layer deposited on the LCO-LBO composite electrode throughout charging process as shown in Figure 4-10 (g). Since the B 1s peak of LBO at 191.5 eV is used as a standard, this shift is attributed to the change in cell voltage, i.e., the electrochemical potential of LCO, in response to the decrease of Li content x in Li_xCoO_2. In the subsequent discharging process, the position of Co^{3+} and Co^{4+} peaks reversibly shifted to a lower binding energy consistently with the electrode potential. In addition, FWHM of Co^{4+} peak and intensity of satellite peak gradually recovered with the decrease of Li content x in Li_xCoO_2, confirming the reversibility.

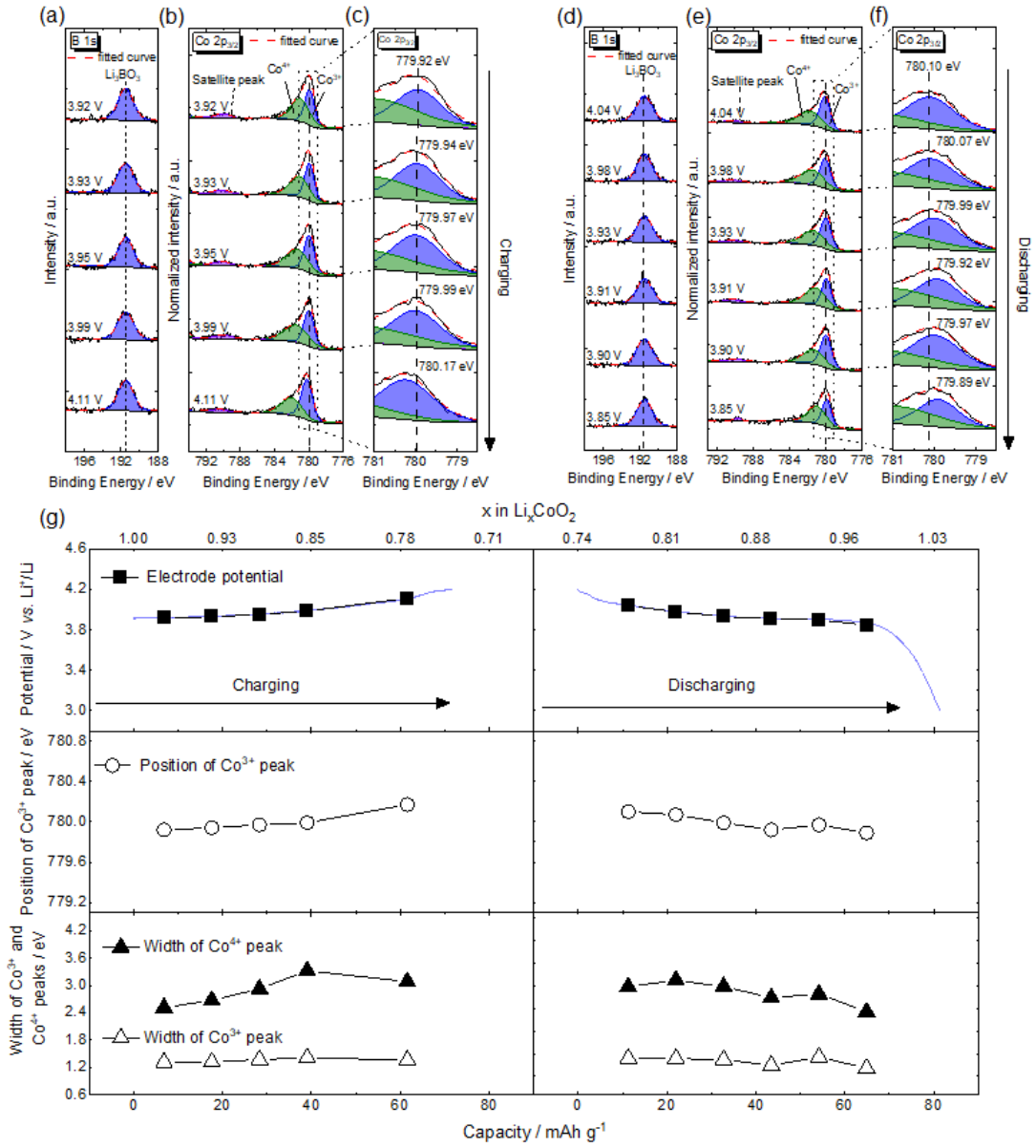

Figure 4-10. B 1s and Co 2p photoelectron spectra generated during (a, b) charging and (d, e) discharging processes in the potential range of 3.0 – 4.2 V *vs.* Li^+/Li. (c, f) Magnified graphs of dashed boxes shown in (b, e). (e) Position of Co^{3+} peak, FWHM of Co^{4+} peak and intensity of satellite peak plotted as functions of capacity, together with galvanostatic charge/discharge potential profiles.

4.2.2 Charge/discharge cycles in potential ranges from 3.0 – 4.2 V or more positive

4.2.2.1 Structural analysis of surface and cross-section of LCO-LBO/LLZT/Li cell

Figure 4-11 and Figure 4-12 show surface and cross-sectional SEM images and EDS maps of the LCO-LBO composite cathode. Although LBO was segregated on composite electrode surfaces and at interfaces between the composite cathode and LLZT solid electrolyte of the ASS cell used in Section 4.2.1,[26] LBO is uniformly distributed in the entire composite cathode without any segregation in the present ASS cell. We denote such LCO-LBO composite cathode as well-dispersed LCO-LBO composite cathode in this paper.

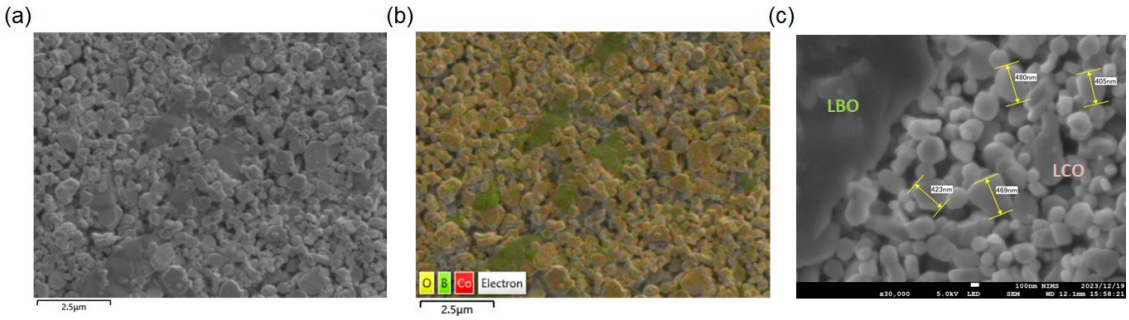

Figure 4-11. (a) A Surface SEM image and (b) corresponding EDS map of well-dispersed LCO-LBO composite cathode. (c) The magnified image of shown in (a).

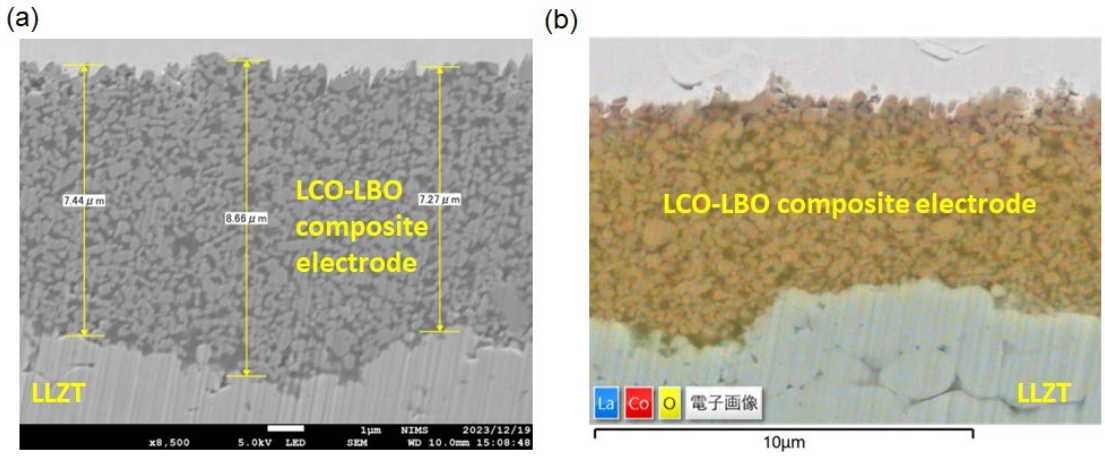

Figure 4-12. Cross-sectional (a) SEM images and (b) EDS maps of the LCO-LBO composite cathode.

4.2.2.2 Charge and discharge characteristics

Figure 4-13 (a) shows typical galvanostatic charge/discharge potential profiles of the ASS cell with the well-dispersed LCO-LBO composite cathode. Under the charging to 4.2 V, the capacity densities of the first charging and discharging were 118 mAh g^{-1} and 86 mAh g^{-1}, respectively, with a Coulombic efficiency of 73%. Those of the second and third cycles were around 86 mAh g^{-1}, with a Coulombic efficiency of 97%, confirming stable cycles without a significant capacity loss under the charging to 4.2 V. We denote such initial irreversible cycle as conditioning cycle, as is the case of ASS cell with LCO-LBO composite cathode with segregation.[26]

When a cutoff potential was extended to 4.7 V, the charge and discharge capacity densities increased to 137 mAh g^{-1} and 121 mAh g^{-1}, respectively, but corresponding

Coulombic efficiency decreased to 88%, suggesting the electrochemical irreversibility of well-dispersed LCO-LBO composite cathode in the ASS cell under the high-voltage operation.

Figure 4-13 (c) shows positive and negative dQ/dV curves corresponding to the plateau regions in the galvanostatic charge and discharge potential profiles, respectively.[21, 27] The positive dQ/dV curves with a cutoff potential of 4.7 V or less positive showed the sharp intense peaks at 3.91 V and relatively small peaks at 4.07 and 4.18 V characteristic to LCO, corresponding to phase transformations from the H1 to H3 phase due to the delithiation.[3] In addition to the three peaks, new two peaks were observed at 4.57 and 4.64 V during charging to 4.7 V, corresponding to the phase transformations from H3 to H1-3 and H1-3 to O1 phase, respectively.[3, 28]

The negative dQ/dV curves except for that during discharging from 4.7 to 3.0 V showed three peaks, corresponding to the phase transformations from H3 to H1 phase due to the lithiation.[3]

The dQ/dV peak intensities and positions during charge/discharge cycles in a potential range of 3.0 – 4.4 V or less positive were similar to each other, suggesting that the series of phase transformations was reversible, leading to stable cycles. On the other hand, the peak intensity at 3.90 V under the discharging from 4.5 to 3.0 V decreased while the peak

positions were similar to those values under discharging from 4.4 to 3.0 V, indicating part of Li^+ ions did not reinsert into the LCO. During the discharging from 4.7 to 3.0 V, the new negative dQ/dV peaks were observed at 4.11 and 4.15 V and not typical to LCO. If those new peaks correspond to the peaks observed at 4.06 and 4.17 V, and undesired side reactions took place among the LCO, LBO and LLZT to increase the electrode polarization, dQ/dV peaks shift to more positive potential under charging and less positive under discharging with keeping the difference of peak position.[29, 30] However, the difference of peak position was 0.04 V in the potential range of 3.0 – 4.7 V, while those value was 0.11 V in the potential range of 3.0 – 4.2 V, as shown in Figure 4-13 (d). Thus, the new negative dQ/dV peaks did not corresponds to the phase transformations from H3 to M1 phase and M1 to H2 phase, and undesired phase transformations took place. In addition, the peak intensity at 3.90 V drastically decreased under discharging from 4.7 to 3.0 V, leading to the decrease of Coulombic efficiency.

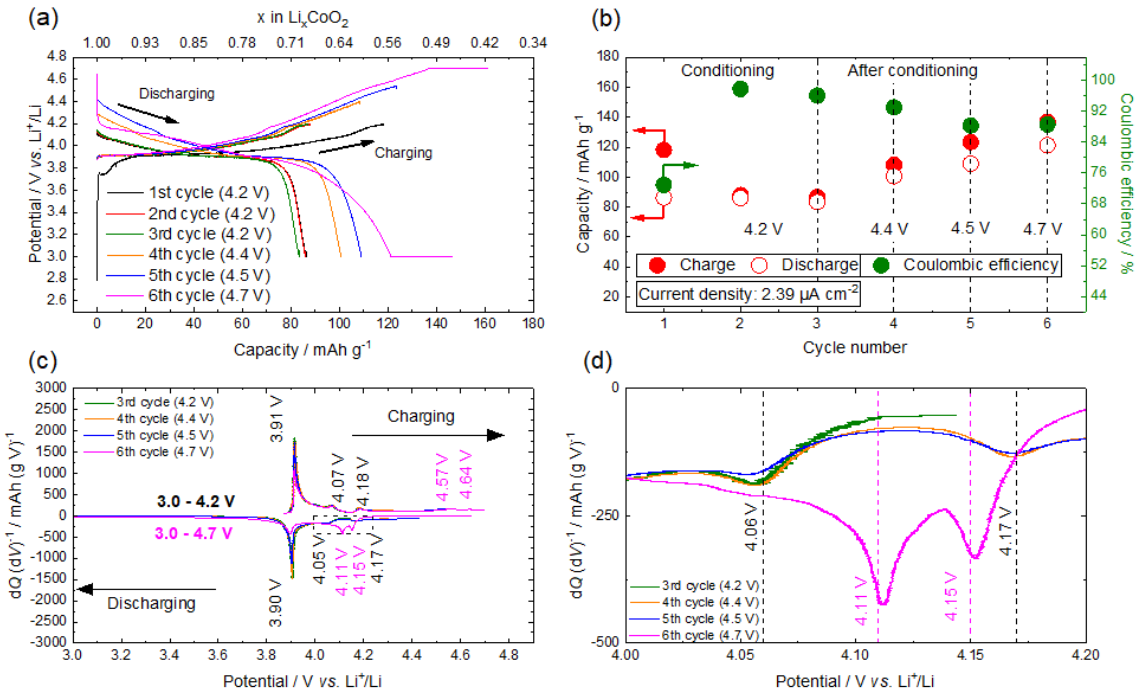

Figure 4-13. (a) Galvanostatic charge/discharge potential profiles of the ASS cell, (b) cycle performance and corresponding Coulombic efficiency of the ASS cell, and (c) corresponding differential capacity plots. (d) Magnified graph of dashed area in (a).

4.2.2.3 Observations of electrochemical reactions of LCO-LBO composite electrode

Figure 4-14 (a) and (b) show the configuration of *operando* HAXPES measurements in section 4.2.1.3 and 4.2.1.4 and following section 4.2.2.3, respectively. In section 4.2.1.3 and 4.2.1.4, all the Co $2p_{3/2}$ and B 1s photoelectron spectra obtained from the LCO-LBO composite cathode with segregation were calibrated using B 1s peak of LBO at 191.5 eV as a standard in configuration (a). In the following section, however, the Co

$2p_{3/2}$ and O 1s photoelectron spectra were calibrated using Pt $4f_{7/2}$ peak of Pt thin layer (current collector) deposited on LCO-LBO composite cathode at 71.1 eV as a standard in configuration (b) because B 1s peak corresponding to LBO was not obtained in configuration (a) although the LBO was uniformly distributed in the LCO-LBO composite cathode by EDS (Figure 4-11 and Figure 4-12).

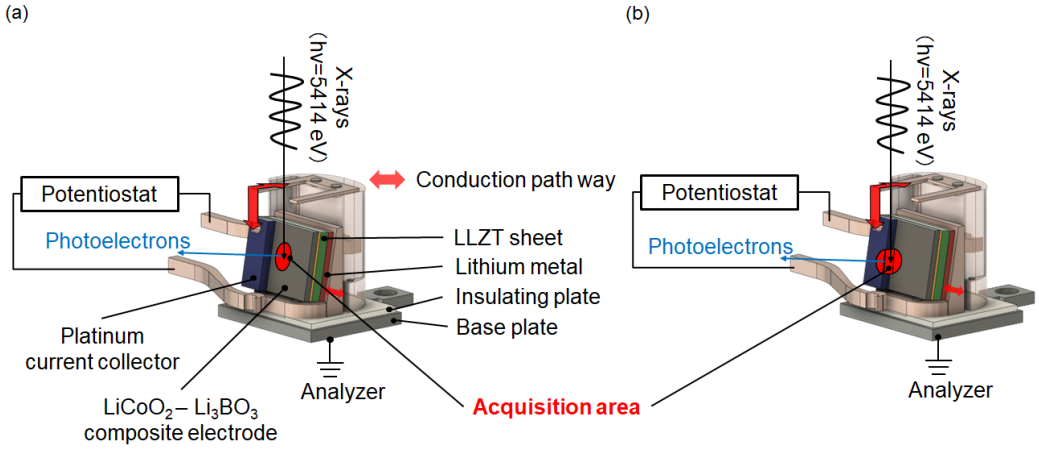

Figure 4-14. Schematic illustrations of configuration of *operando* HAXPES measurements in (a) section 4.2.1.3 and 4.2.1.4 and (b) following section 4.2.2.3.

Figure 4-15 shows the Co $2p_{3/2}$ photoelectron spectra of the LCO-LBO composite electrode before and after conditioning cycles together with electrode potentials and fitting parameters. As documented in the section 4.2.1.3, Co 2p peak is composed of two components; Co^{3+} peak at 779.3 eV and the one corresponding to the final state effect at 780.2 eV. As all the spectra were calibrated using Pt $4f_{7/2}$ peaks from the Pt thin layer deposited on LCO-LBO composite electrode as a current collector (Figure 4-14), the

position of Co^{3+} peak remains almost unchanged throughout all the charge/discharge cycles except for the 0.2 eV shift after the first charging due to the change from p-type semiconducting to metallic states (section 4.2.1.3). After the first charging up to 4.2 V, a peak corresponding to Co^{4+} appears at the binding energy slightly higher than that of final state effect and thus the apparent FWHM of shoulder peak attributed to the final state effect and Co^{4+} peak significantly broadened. After the successive discharging up to 3.0 V, the apparent FWHM reverted to the original as Co^{4+} peaks became smaller due to the reduction accompanying with the insertion of Li ions. Such broadening and shrinking are reversible up to the 4th discharging after charging up to 4.4 V, confirming the very high capacity retention capability of LCO in high-voltage operation When the voltage, i.e., positive potential limit of LCO with respect to Li^+/Li, is extended to 4.5 V, the FWHM of peak corresponding to Co^{4+} ions and final state effect does not recovered to the original value, implying the occurrence of irreversible oxidation reactions such as oxygen release and structural degradation.[31, 32]

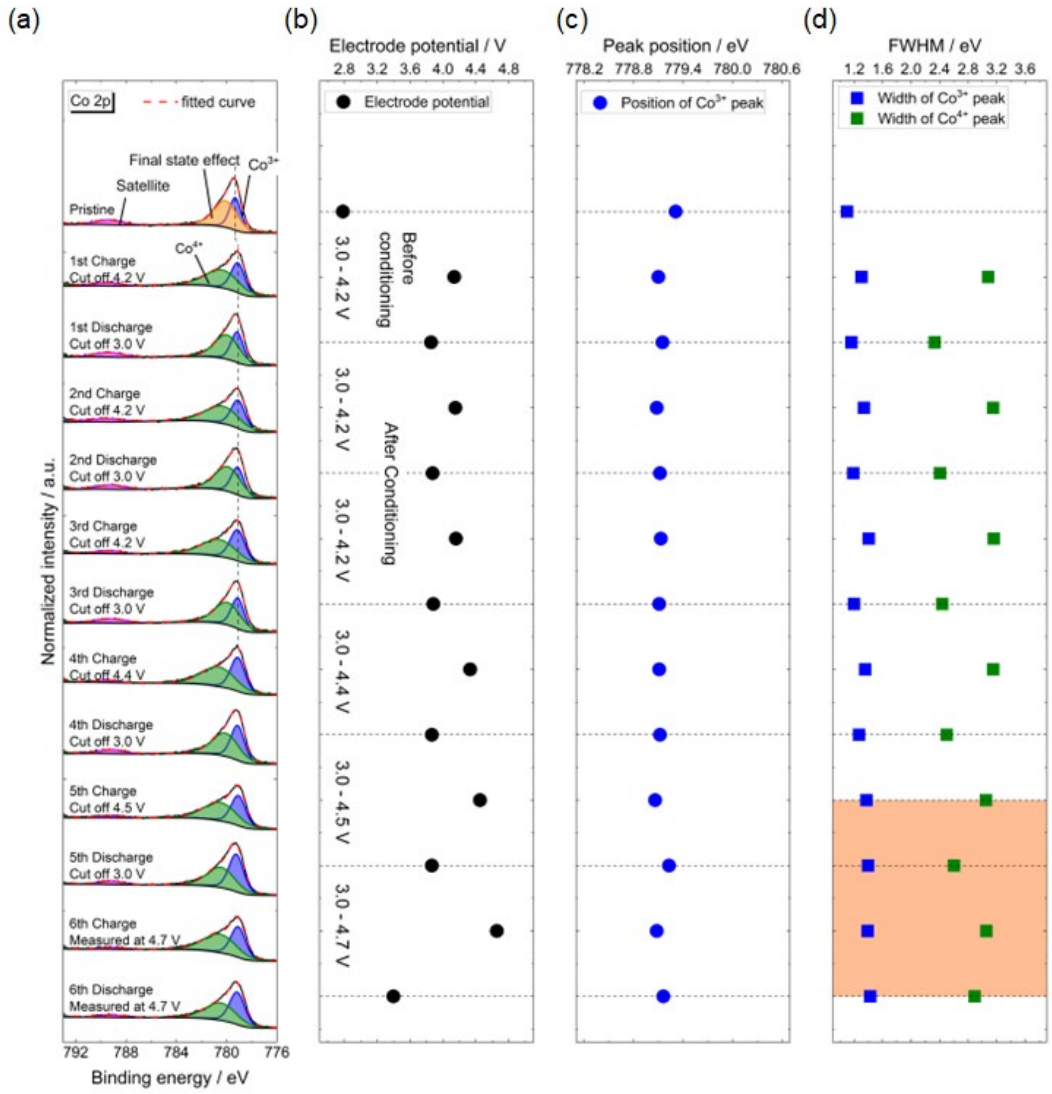

Figure 4-15. (a) Co $2p_{3/2}$ photoelectron spectra of the well-dispersed LCO-LBO composite cathode before and after charge/discharge cycles calibrated by Pt peak at 71.1 eV in the potential range of 3.0 – 4.2 V or more positive. (b) Average electrode potential under the HAXPES measurements at each state. Peak position of (c) Co^{3+} ions and (d) FWHM of Co^{3+} and Co^{4+} ions.

Figure 4-16 shows the O 1s photoelectron spectra of the well-dispersed LCO-LBO composite cathode before and after conditioning cycles calibrated using Pt $4f_{7/2}$ peaks from the Pt thin layer deposited on LCO-LBO composite cathode as a current collector. In the O 1s region of pristine cell, two peaks corresponding to O^{2-} anions in a lattice LCO and Li_2CO_3 adsorbed on the LCO surface were observed at 529.1 eV and 531.8 eV, respectively.[7] Despite of larger photoionization cross section of O 1s region compared with B 1s region under Cr-Kα irradiation,[33] no LBO peaks was observed in B 1s (~191.5 eV) and O 1s regions (~530 eV)[34] because the LBO was uniformly distributed in the entire composite electrode as imaged by SEM-EDS analysis (Figure 4-11 and Figure 4-12). In addition, no peaks corresponding to LLZT were observed in O 1s (~530 eV), La $3d_{5/2}$ (837.2 eV), Zr $3d_{5/2}$ (~184.2 eV), and Ta 4d regions (~230 eV).[35, 36]

After the first charging with a cutoff voltage of 4.2 V, the Li_2CO_3 peak ~531.8 eV shifted to ~530.4 eV. The shift was almost consistent with the change of open circuit voltage of pristine state ~2.8 V to the cutoff voltage 4.2 V. In the present experiment, the Pt thin layer deposited on LCO-LBO composite cathode was grounded together with hemispherical analyzer and its Pt $4f_{7/2}$ peak was used as a standard. Hence, the peak corresponding to Li_2CO_3 shifted as is the case of LBO (Figure 4-4 (b)) due to their insulating nature.[14, 23] Hereafter, the Li_2CO_3 peak reversibly shifted in response to the

potential change due to the charge/discharge cycles until the 5th discharge. After the 6th charging, however, the peak at around Li_2CO_3 did not follow the potential changes caused by charge/discharge cycles anymore. Here, the C1s photoelectron spectra of LCO-LBO composite cathode after 3rd to 6th cycles are shown in Figure 4-17. The intensity of Li_2CO_3 peak at around 290 eV decreased after charging to 4.5 V or more positive, implying the decomposition of Li_2CO_3.[37] Thus, the peak at around 530.1 eV of LCO-LBO composite cathode after 5th charging is not corresponding to Li_2CO_3 but other species.

After the first charging up to 4.2 V, the peak corresponding to lattice O^{2-} anions also shifted to a lower binding energy by around 0.6 eV. In the subsequent discharging, the peak shifted to a higher binding energy by around 0.4 eV. After the first cycle, the position of O^{2-} peak reversibly responded to the charge/discharge cycles with a positive potential limit of 4.5 V, and the values of peak shift of lattice O^{2-} anions were around 0.4 eV except for that from the pristine state to the first charged state because the shift during the first charging includes not only the above-mentioned electrochemical reactions but also the transition of electronic state from a semiconducting to metallic. Two independent groups observed similar peak at around 528.7 eV with maintaining the original O^{2-} anions peak at around 529.2 eV at thin-film electrode surfaces of LCO and 528.7 eV[14, 38] after charging using hard x-ray photoelectron spectroscopy. Although the origin of new peak at a lower

binding energy was not clearly identified in their papers, it can be attributed to an increase of screening effect of the core electron because of metallic properties of delithiated LCO[39] and/or hybridization between Co 3d states and O 2p band that induces the upshift of O 1s level toward the Fermi level.[6]

When the positive potential limit for charging was extended to 4.7 V, the values of peaks shift of lattice O^{2-} anions increased to around 0.7 eV. This can be explained by the increase of the screening effect and/or stronger hybridization of Co 3d and O 2p orbitals due to the progression of delithiation.[6, 39-41]

In addition to the peak shifts, new peak appeared at 531.2 eV corresponding to electron deficient oxygen dimer$(O_2)^{n-}$ after charging to 4.7 V, and it remained after the subsequent discharging, indicating the oxidation of lattice oxygen under high voltage cycle.[38] The peaks of Li_2CO_3 and electron deficient oxygen dimer $(O_2)^{n-}$ cannot be deconvoluted because their peak positions are very close to each other. As evident by photoelectron spectra of C 1s region (Figure 4-17), however, Li_2CO_3 was decomposed and thus the peak at 531.2 eV should be due to the electron deficient oxygen dimer $(O_2)^{n-}$. Oxygen dimer will be eventually released as O_2 gas, leading to the structural disorder.[31, 32]

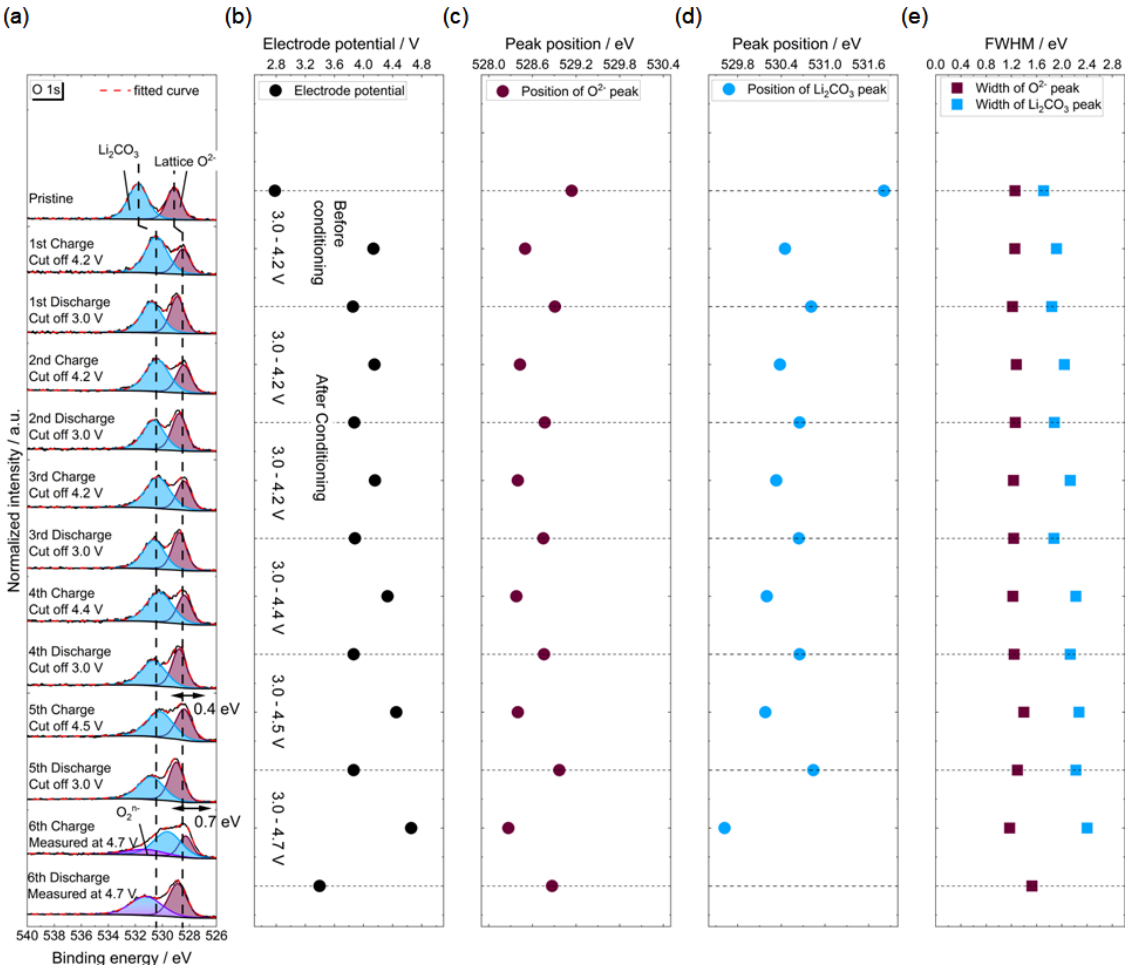

Figure 4-16. (a) O 1s photoelectron spectra of the well-dispersed LCO-LBO composite cathode before and after charge/discharge cycles calibrated by Pt peak at 71.1 eV in the potential range of 3.0 – 4.7 V. (b) Average electrode potential under the HAXPES measurements at each state. Peak position of (c) lattice O^{2-} ions and (d) Li_2CO_3. (d) FWHM of lattice O^{2-} ions and Li_2CO_3.

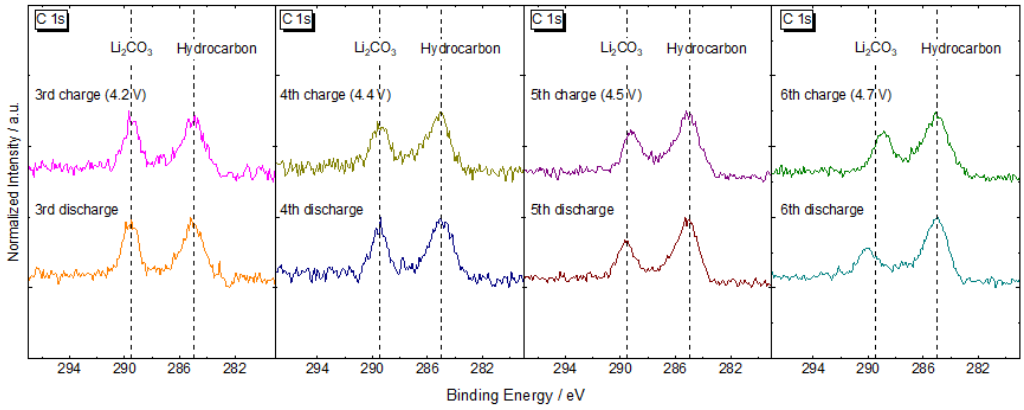

Figure 4-17. C 1s photoelectron spectra for LCO-LBO composite electrode under each electrochemical condition calibrated by a hydrocarbon peak at 285.0 eV. Dashed lines indicate positions of peaks attributed to Li_2CO_3 and hydrocarbons, respectively.

4.3 Conclusion

We investigated the electrochemical reactions of LCO-LBO composite cathode deposited on a LLZT in an ASS cell configuration during charge/discharge cycles using a laboratory-based *operando* HAXPES. In the first charging, the change in valence state of LCO due to the transition from a p-type semiconducting to a metallic state induced by delithiation was observed, as shown in Figure 4-4. As shown in Figure 4-10, LCO peak shifted consistently with the change of cell voltage because the B 1s peak due to LBO was used as an internal standard.

In the potential range of 3.0 – 4.4 V or less positive, reversible oxidation/reduction of Co^{4+} ions were confirmed by increase/decrease of FWHMs of Co^{4+} peak in response to charge/discharge cycles, respectively. In the potential range of 3.0 – 4.5 V or more positive, irreversible oxidation of Co^{4+} ions took place, confirmed by irreversible increase of FWHMs and peak position of Co^{4+} ions. In addition to the irreversible oxidation of Co^{4+} ions, lattice O^{2-} anions in the LCO were also irreversibly oxidized in the potential range of 3.0 – 4.7 V, leading to capacity fading.

References

(1) Godshall, N. A.; Raistrick, I. D.; Huggins, R. A. THERMODYNAMIC INVESTIGATIONS OF TERNARY LITHIUM-TRANSITION METAL-OXYGEN CATHODE MATERIALS. *Mater. Res. Bull.* **1980**, *15*, 561-570. DOI: 10.1016/0025-5408(80)90135-X.

(2) Lyu, Y.; Wu, X.; Wang, K.; Feng, Z.; Cheng, T.; Liu, Y.; Wang, M.; Chen, R.; Xu, L.; Zhou, J.; et al. An Overview on the Advances of $LiCoO_2$ Cathodes for Lithium-Ion Batteries. *Advanced Energy Materials* **2020**, *11* (2). DOI: 10.1002/aenm.202000982.

(3) Lin, C.; Li, J.; Yin, Z. W.; Huang, W.; Zhao, Q.; Weng, Q.; Liu, Q.; Sun, J.; Chen, G.; Pan, F. Structural Understanding for High-Voltage Stabilization of Lithium Cobalt Oxide. *Adv. Mater.* **2023**, e2307404. DOI: 10.1002/adma.202307404 From NLM Publisher.

(4) Amatucci, G. G.; Tarascon, J. M.; Klein, L. C. CoO_2, The End Member of the $LiCoO_2$ Solid Solution. *Journal of Electrochemical Society* **1996**, *143*, 1114. DOI: 10.1149/1.1836594.

(5) Marianetti, C. A.; Kotliar, G.; Ceder, G. A first-order Mott transition in Li_xCoO_2. *Nat Mater* **2004**, *3* (9), 627-631. DOI: 10.1038/nmat1178 From NLM Medline.

(6) Ensling, D.; Cherkashinin, G.; Schmid, S.; Bhuvaneswari, S.; Thissen, A.; Jaegermann, W. Nonrigid Band Behavior of the Electronic Structure of $LiCoO_2$ Thin Film during Electrochemical Li Deintercalation. *Chem. Mater.* **2014**, *26* (13), 3948-3956. DOI: 10.1021/cm501480b.

(7) Dahéron, L.; Dedryvère, R.; Martinez, H.; Ménétrier, M.; Denage, C.; Delmas, C.; Gonbeau, D. Electron Transfer Mechanisms upon Lithium Deintercalation from

$LiCoO_2$ to CoO_2. *Chem. Mater.* **2008**, *20*, 583-590. DOI: 10.1021/cm702546s.

(8) Mizokawa, T.; Fujimori, A. Electronic structure and orbital ordering in perovskite-type 3d transition-metal oxides studied by Hartree-Fock band-structure calculations. *Physical Review B* **1996**, *B54*, 5368. DOI: 10.1103/PhysRevB.54.5368.

(9) Mizokawa, T.; Wakisaka, Y.; Sudayama, T.; Iwai, C.; Miyoshi, K.; Takeuchi, J.; Wadati, H.; Hawthorn, D. G.; Regier, T. Z.; Sawatzky, G. A. Role of oxygen holes in Li_xCoO_2 revealed by soft X-ray spectroscopy. *Phys. Rev. Lett.* **2013**, *111* (5), 056404. DOI: 10.1103/PhysRevLett.111.056404 From NLM PubMed-not-MEDLINE.

(10) Endo, E.; Yasuda, T.; Kita, A.; Yamaura, K.; Sekaia, K. A $LiCoO_2$ Cathode Modified by Plasma ChemicalVapor Deposition for Higher Voltage Performance. *J. Electrochem. Soc.* **2000**, *147* (4), 1291. DOI: 10.1149/1.1393352.

(11) Amatucci, G. G.; Tarascon, J. M.; Klein, L. C. Cobalt dissolution in $LiCoO_2$-based non-aqueous rechargeable batteries. *Solid State Ionics* **1996**, *83*, 167-173. DOI: 10.1016/0167-2738(95)00231-6.

(12) Takamatsu, D.; Koyama, Y.; Orikasa, Y.; Mori, S.; Nakatsutsumi, T.; Hirano, T.; Tanida, H.; Arai, H.; Uchimoto, Y.; Ogumi, Z. First In Situ Observation of the $LiCoO_2$ Electrode/Electrolyte Interface by Total-Reflection X-ray Absorption Spectroscopy. *Angew. Chem. Int. Ed.* **2012**, *51* (46), 11597-11601. DOI: 10.1002/anie.201203910.

(13) Ohnishi, T.; Mitsuishi, K.; Takada, K. In Situ X-ray Diffraction of $LiCoO_2$ in Thin-Film Batteries under High-Voltage Charging. *ACS Applied Energy Materials* **2021**, *4* (12), 14372-14379. DOI: 10.1021/acsaem.1c03046.

(14) Kiuchi, H.; Hikima, K.; Shimizu, K.; Kanno, R.; Toshiharu, F.; Matsubara, E. Operando hard X-ray photoelectron spectroscopy of $LiCoO_2$ thin film in an all-solid-state lithium ion battery. *Electrochem. Commun.* **2020**, *118*, 106790. DOI: 10.1016/j.elecom.2020.106790.

(15) Ohta, S.; Komagata, S.; Seki, J.; Saeki, T.; Morishita, S.; Asaoka, T. All-solid-state lithium ion battery using garnet-type oxide and Li_3BO_3 solid electrolytes fabricated by screen-printing. *J. Power Sources* **2013**, *238*, 53-56. DOI: 10.1016/j.jpowsour.2013.02.073.

(16) Park, K.; Yu, B.-C.; Jung, J.-W.; Li, Y.; Zhou, W.; Gao, H.; Son, S.; Goodenough, J. B. Electrochemical Nature of the Cathode Interface for a Solid-State Lithium-Ion Battery: Interface between $LiCoO_2$ and Garnet-$Li_7La_3Zr_2O_{12}$. *Chem. Mater.* **2016**, *28* (21), 8051-8059. DOI: 10.1021/acs.chemmater.6b03870.

(17) Jang, Y.-I.; Dudney, N. J.; Blom, D. A.; Allard, L. F. High-Voltage Cycling Behavior of Thin-Film $LiCoO_2$ Cathodes. **2002**, *149* (11), A1442-A1447. DOI: 10.1149/1.1511751.

(18) Kanamura, K.; Kimura, T.; Shoji, M.; Munakata, H. All Solid State Battery with LLZ Solid Electrolyte and Li Metal Anode. *ECS Meeting Abstracts* **2016**, *MA2016-03* (1), 45-45. DOI: 10.1149/ma2016-03/1/45.

(19) Sakakura, M.; Mitsuishi, K.; Okumura, T.; Ishigaki, N.; Iriyama, Y. Fabrication of Oxide-Based All-Solid-State Batteries by a Sintering Process Based on Function Sharing of Solid Electrolytes. *ACS Appl Mater Interfaces* **2022**, *14* (43), 48547-48557. DOI: 10.1021/acsami.2c10853 From NLM PubMed-not-MEDLINE.

(20) Ren, Y.; Liu, T.; Shen, Y.; Lin, Y.; Nan, C.-W. Garnet-type oxide electrolyte with novel porous-dense bilayer configuration for rechargeable all-solid-state lithium

batteries. *Ionics* **2017**, *23* (9), 2521-2527. DOI: 10.1007/s11581-017-2224-5.

(21) Reimers, J. N.; Dahn, J. R. Electrochemical and In Situ X-Ray Diffraction Studies of Lithium Intercalation in Li_xCoO_2. *J. Electrochem. Soc.* **1992**, *139*, 2091. DOI: 10.1149/1.2221184.

(22) Li, S.; Tsutsumi, S.; Shironita, S.; Umeda, M. Peak Attribution of the Differential Capacity Profile of a $LiCoO_2$ -based Three-electrode Li-ion Laminate Cell. *Electrochemistry* **2022**, *90* (3), 037004-037004. DOI: 10.5796/electrochemistry.21-00128.

(23) Wu, X.; Villevieille, C.; Novak, P.; El Kazzi, M. Monitoring the chemical and electronic properties of electrolyte-electrode interfaces in all-solid-state batteries using operando X-ray photoelectron spectroscopy. *Phys. Chem. Chem. Phys.* **2018**, *20* (16), 11123-11129. DOI: 10.1039/c8cp01213j.

(24) Nomura, Y.; Yamamoto, K.; Hirayama, T.; Ouchi, S.; Igaki, E.; Saitoh, K. Direct Observation of a Li-Ionic Space-Charge Layer Formed at an Electrode/Solid-Electrolyte Interface. *Angew. Chem. Int. Ed. Engl.* **2019**, *58* (16), 5292-5296. DOI: 10.1002/anie.201814669 From NLM PubMed-not-MEDLINE.

(25) A. T. Appapillai; A. N. Mansour; J. Cho; Shao-Horn, Y. Microstructure of $LiCoO_2$ with and without "$AlPO_4$" Nanoparticle Coating: Combined STEM and XPS Studies. *Chem. Mater.* **2007**, *19*, 5748-5757. DOI: 10.1021/cm0715390.

(26) Iwama, T.; Ohnishi, T.; Masuda, T. Operando Observation of Lithiation and Delithiation Reactions of a $LiCoO_2$-Li_3BO_3 Composite Electrode Formed on a $Li_{6.6}La_3Zr_{1.6}Ta_{0.4}O_{12}$ Solid Electrolyte Sheet by Laboratory-based Hard X-ray Photoelectron Spectroscopy. *Electrochemistry* **2023**, *91* (11), 117005. DOI: 10.5796/electrochemistry.23-00090.

(27) Bloom, I.; Jansen, A. N.; Abraham, D. P.; Knuth, J.; Jones, S. A.; Battaglia, V. S.; Henriksen, G. L. Differential voltage analyses of high-power, lithium-ion cells 1. Technique and application. *J. Power Sources* **2005**, *139* (1-2), 295-303. DOI: 10.1016/j.jpowsour.2004.07.021.

(28) Xia, H.; Tang, S. B.; Lu, L. Thin Film Microbatteries Prepared by Pulsed Laser Deposition. *Journal of the Korean Physical Society* **2007**, *51* (3), 1055-1062. DOI: 10.3938/jkps.51.1055.

(29) Yano, A.; Shikano, M.; Ueda, A.; Sakaebe, H.; Ogumi, Z. $LiCoO_2$ Degradation Behavior in the High-Voltage Phase Transition Region and Improved Reversibility with Surface Coating. *J. Electrochem. Soc.* **2016**, *164* (1), A6116-A6122. DOI: 10.1149/2.0181701jes.

(30) Liu, D.; He, Z.; Liu, X. Increased cycling stability of $AlPO_4$-coated $LiMn_2O_4$ for lithium ion batteries. *Mater. Lett.* **2007**, *61* (25), 4703-4706. DOI: 10.1016/j.matlet.2007.03.012.

(31) Jiang, Y. Y.; Qin, C. D.; Yan, P. F.; Sui, M. L. Origins of capacity and voltage fading of $LiCoO_2$ upon high voltage cycling. *Journal of Materials Chemistry A* **2019**, *7* (36), 20824-20831. DOI: 10.1039/c9ta06579b.

(32) Kong, W.; Zhang, J.; Wong, D.; Yang, W.; Yang, J.; Schulz, C.; Liu, X. Tailoring Co3d and O2p Band Centers to Inhibit Oxygen Escape for Stable 4.6 V $LiCoO_2$ Cathodes. *Angew. Chem. Int. Ed. Engl.* **2021**, *60* (52), 27102-27112. DOI: 10.1002/anie.202112508 From NLM PubMed-not-MEDLINE.

(33) Scofield, J. H. Theoretical Photoionization Cross Section from 1 to 1500 keV. **1973**. DOI: 10.2172/4545040.

(34) Nagao, K.; Suyama, M.; Kato, A.; Hotehama, C.; Deguchi, M.; Sakuda, A.;

Hayashi, A.; Tatsumisago, M. Highly Stable Li/Li_3BO_3–Li_2SO_4 Interface and Application to Bulk-Type All-Solid-State Lithium Metal Batteries. *ACS Applied Energy Materials* **2019**, *2* (5), 3042-3048. DOI: 10.1021/acsaem.9b00470.

(35) Li, Y.; Chen, X.; Dolocan, A.; Cui, Z.; Xin, S.; Xue, L.; Xu, H.; Park, K.; Goodenough, J. B. Garnet Electrolyte with an Ultralow Interfacial Resistance for Li-Metal Batteries. *J. Am. Chem. Soc.* **2018**, *140* (20), 6448-6455. DOI: 10.1021/jacs.8b03106 From NLM PubMed-not-MEDLINE.

(36) Yamada, H.; Ito, T.; Kammampata, S. P.; Thangadurai, V. Toward Understanding the Reactivity of Garnet-Type Solid Electrolytes with H_2O/CO_2 in a Glovebox Using X-ray Photoelectron Spectroscopy and Electrochemical Methods. *ACS Applied Materials & Interfaces* **2020**, *12* (32), 36119-36127. DOI: 10.1021/acsami.0c09135.

(37) Papp, J. K.; Li, N.; Kaufman, L. A.; Naylor, A. J.; Younesi, R.; Tong, W.; McCloskey, B. D. A comparison of high voltage outgassing of $LiCoO_2$, $LiNiO_2$, and Li_2MnO_3 layered Li-ion cathode materials. *Electrochim. Acta* **2021**, *368*. DOI: 10.1016/j.electacta.2020.137505.

(38) Guhl, C.; Rohrer, J.; Kehne, P.; Ferber, T.; Alff, L.; Albe, K.; Jaegermann, W.; Komissinskiy, P.; Hausbrand, R. The role of covalent bonding and anionic redox for the performance of sodium cobaltate electrode materials. *Energy Storage Materials* **2021**, *37*, 190-198. DOI: 10.1016/j.ensm.2021.02.008.

(39) Ruiz, D. D.; Cocchi, C. First-Principles Core Spectroscopy of $LiCoO_2$ and CoO_2. *The Journal of Physical Chemistry C* **2022**, *126* (27), 10949-10956. DOI: 10.1021/acs.jpcc.2c01597.

(40) Yang, J. H.; Kim, H.; Ceder, G. Insights into Layered Oxide Cathodes for

Rechargeable Batteries. *Molecules* **2021**, *26* (11). DOI: 10.3390/molecules26113173 From NLM PubMed-not-MEDLINE.

(41) Hu, E.; Li, Q.; Wang, X.; Meng, F.; Liu, J.; Zhang, J.-N.; Page, K.; Xu, W.; Gu, L.; Xiao, R.; et al. Oxygen-redox reactions in LiCoO2 cathode without O–O bonding during charge-discharge. *Joule* **2021**, *5* (3), 720-736. DOI: 10.1016/j.joule.2021.01.006.

5. Static and Dynamic Analysis of Lithiation/Delithiation of Amorphous-SiO_x Thin-Film Anodes

5.1 Introduction

Silicon oxides (SiO_x) have been attracting wide attention as a candidate of anode materials for advanced lithium ion batteries because its cycle performance is significantly improved as compared to pure Si which has an excellent capacity density and a poor cyclability.[1] SiO_x anodes show very large irreversible capacity loss in the initial cycle because part of Li^+ ions inserted into Si/Li silicides are consumed for the side reaction to form electrochemically inactive species,[2-4] as well as reversible Li silicides (Li_ySi).[4] Thus, the achievable capacity density becomes much lower than that of pure Si. These inactive species are the origin of lower capacity density but considered as a key to improve the cycle performance.[1, 2, 5, 6] Miyazaki et al. proposed that the inactive species act as a buffer against the pulverization of Li_ySi during charge/discharge cycles because Si is surrounded by SiO_2 matrix/inactive species in SiO_x anodes and immobilized by them.[1] On the other hand, Kitada et al. proposed that the lithiation of SiO_x does not reach up to $Li_{3.75}Si$ where the crystalline Li_ySi (c-Li_ySi) forms, due to the formation of highly resistive Li_2O and

lithium-silicate species or compressive stress to Si caused by the volume expansion of inactive species during the lithiation.[7] As the phase transformation from c-Li_ySi to amorphous Li_ySi (a-Li_ySi) induces significant volume change,[8-10] avoidance of the formation of c-Li_ySi may cause the improved cycle performance.[8, 11, 12] However, the formation mechanism of the Li_2O and lithium silicates (Li silicates) during the initial lithiation are unclear yet.

In the present Chapter, the successive lithiation/delithiation reactions of a sputter-deposited $SiO_{0.53}$ thin-film anode on a $Li_{6.6}La_3Zr_{1.6}Ta_{0.4}O_{12}$ (LLZT) solid electrolyte were tracked using *in-situ* electrochemical x-ray photoelectron spectroscopy (XPS) system. The origin of superior cycle performance of SiO_x thin-film anodes were discussed by static and dynamic observations.

5.2 Results and Discussion

5.2.1 Composition of SiO_x thin-film anode

The oxygen content in SiO_x deposited by radio-frequency (RF) magnetron sputtering using Ar/O_2 gas mixtures on a LLZT pellet was confirmed to be 0.53 by energy dispersive x-ray spectroscopy (EDX). This value should be the average of entire SiO_x thin film because the probing depth of EDX with several micrometers is sufficiently larger than the thickness of the $SiO_{0.53}$ thin film, 100 nm.[13]

Oxide species in the $SiO_{0.53}$ at the pristine state were characterized using XPS. Figure 5-1 (a) shows Si 2p photoelectron spectra for the $SiO_{0.53}$ thin-film anode. Two broad Si 2p peaks were observed at around 99 and 102 eV. The curve fitting analysis was performed based on an assumption that the Si 2p curve in SiO_x consists of five components with the oxidation states of 0 (Si^0), +1 (Si^{+1}), +2 (Si^{+2}), +3 (Si^{+3}), and +4 (Si^{+4}) with each energy difference of 1 eV.[1, 14, 15] The full width half maximums (FWHMs) and intensity ratio of the Si $2p_{3/2}$ and $2p_{1/2}$ peaks corresponding to Si oxides were fixed at the same value to reduce the number of refinement parameters.[1, 14, 15] In contrast, the binding energy and the FWHM of the Si $2p_{3/2}$ peak in the Si^0 component were set as variable parameters. Figure 5-1 (b) shows the ratio of the peak integrations of each component with the oxidation number of 0, +1, +2, +3, and +4 obtained by the fitting analysis. This shows Si and $SiO_{1.5\text{-}2}$ are the major components in $SiO_{0.53}$ together with minor suboxides $SiO_{0.5\text{-}1}$.[4, 7]

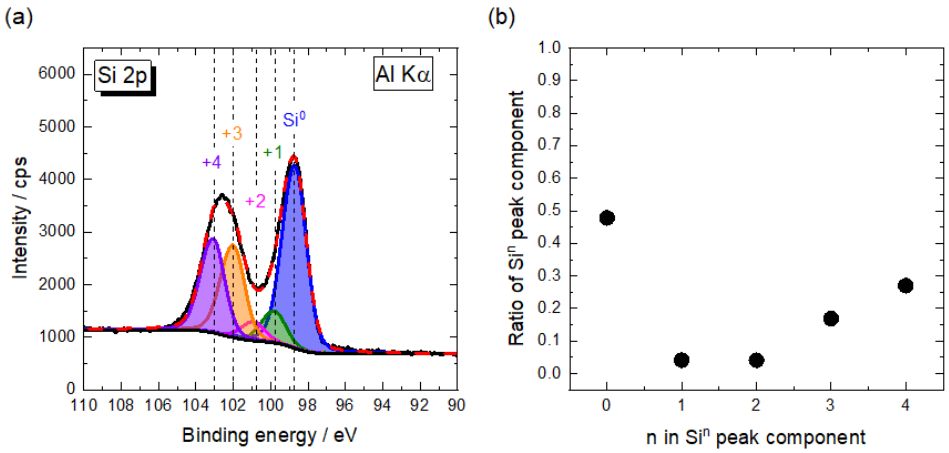

Figure 5-1 (a) Si 2p photoelectron spectra for $SiO_{0.53}$ thin-film anode obtained using Al-Kα rays calibrated by hydrocarbon C 1s peak at 285.0 eV. Si 2p peaks are deconvoluted into five components with the oxidation number of 0, +1, +2, +3, and +4. (b) The ratio of each peak component in the $SiO_{0.53}$ thin-film anode.

5.2.2 Charge/discharge characteristics

Figure 5-2 shows the galvanostatic lithiation/delithiation potential profiles obtained for $SiO_{0.53}$ thin-film half-cell in SiO_x/LLZT/Li configuration. The capacity values are given in mAh g^{-1} based on the weight of Si in $SiO_{0.53}$ thin film. The charge integrations obtained for the first lithiation and delithiation were 3461 mAh g^{-1} and 1514 mAh g^{-1}, respectively. The initial Coulombic efficiency for $SiO_{0.53}$ thin film, 43.9% was much lower than those of pure Si thin-film in both liquid-type[16, 17] and all-solid-state cells.[8, 18] The origin of such large irreversible capacity is considered to be due to the formation of irreversible species such as Li_2O and Li-silicates, in addition to the polarization resistance.

In the second cycle, the charge integrations obtained for the lithiation and delithiation were 1683 mAh g^{-1} and 1563 mAh g^{-1}, respectively, with the Coulombic efficiency of 92.9%. Thereafter, the specific capacity and Coulombic efficiency became almost constant.

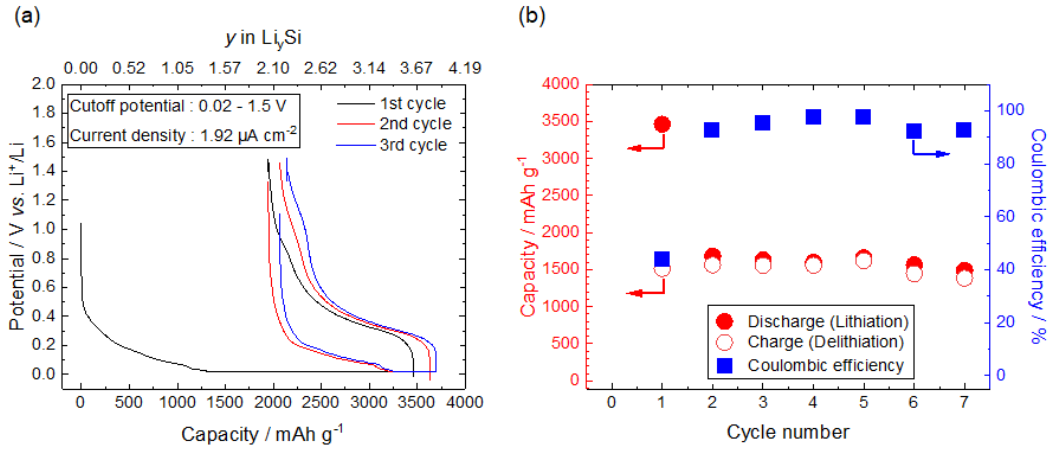

Figure 5-2 (a) Galvanostatic lithiation/delithiation potential profiles and (b) cycle performance obtained for $SiO_{0.53}$/LLZT/Li cell at current of 1.92 μA cm^{-2} and in the potential range of 0.02 – 1.5 V *vs.* Li^+/Li under vacuum condition. Specific capacity was normalized by mass of deposited Si atoms under the sputtering condition using Ar gas.

Figure 5-3 shows the galvanostatic *dQ/dV* curves obtained by differentiating the smoothed potential profiles during the lithiation/delithiation, respectively. The negative *dQ/dV* curve during the first lithiation showed three peaks at 0.34, 0.17, and 0.07 V corresponding to the lithiation of SiO_x to form Li silicates, lithiation of amorphous Si (a-

Si) in the $SiO_{0.53}$ to form Li-poor amorphous Li silicide (a-Li_ySi), and lithiation of Li-poor to form Li-rich a-Li_ySi, respectively.[8, 19-21] In the first delithiation, a broad peak and a shoulder peak were observed at 0.31 V and around 0.4 – 0.6 V corresponding to the delithiation of Li-rich a-Li_ySi,[20, 22] and delithiation of Li-poor a-Li_ySi.[8, 19-21] The intensity of shoulder peak was smaller than previous results on SiO_x thin-film anodes in both liquid-type[2, 6, 23] and all-solid-state cells,[1] suggesting that Li^+ ions were not completely extracted from Li-poor a-Li_ySi due to the polarization resistance.

In the second lithiation, the intensity of negative peak due to the lithiation of a-Si observed at 0.17 V in the first lithiation decreased, confirming that delithiation from a-Li_ySi cannot be completed to form a-Si in this charge/discharge condition.[22] In addition to the decrease of negative peak at 0.17 V, the negative peak due to the lithiation of SiO_x observed at 0.34 V in the first lithiation completely disappeared, confirming the formation of electrochemically inactive species, such as Li_2O and Li silicates in the first lithiation.[2] Hereafter, the positive and negative *dQ/dV* curve remained unchanged, indicating reversible lithiation/delithiation processes.

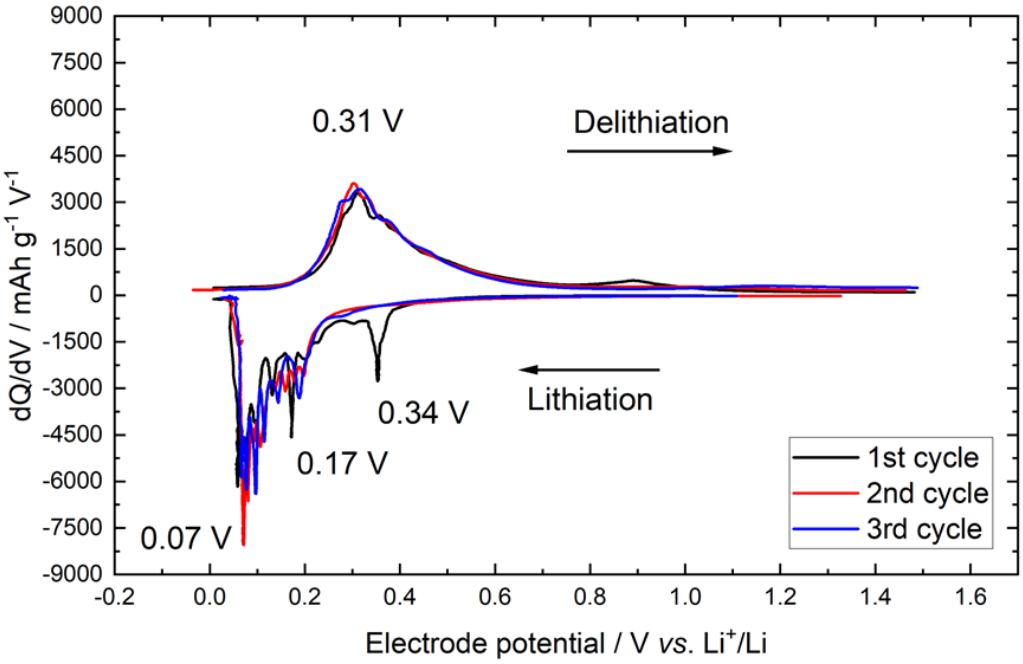

Figure 5-3. Galvanostatic *dQ/dV* curves generated for $SiO_{0.53}$/LLZT/Li thin-film half-cell at current of 1.92 µA cm^{-2} and in the potential range of 0.02 – 1.5 V *vs.* Li^+/Li under vacuum condition.

5.2.3 Analysis of electrochemical lithiation/delithiation process of $SiO_{0.53}$ thin-film anode using XPS

5.2.3.1 Static observations

Figure 5-4 (a), (b), and (c) show the Li 1s, Si 2p and O 1s photoelectron spectra for the $SiO_{0.53}$ thin film after the first and second lithiation/delithiation processes. As described in Section 5.2.1, bulk Si (Si^0) and suboxides (SiO_x) peaks were observed at 98.7 and around 99.7 – 102.7 eV in Si 2p region in the pristine state. In the Li 1s region, a peak

corresponding to lithium carbonates (Li_2CO_3) at 55.8 eV is the majority species. This is probably due to the contamination during the sample preparation and/or transfer processes because any lithiated species were not observed in Si 2p region as discussed in the previous section 5.2.1 with Figure 5-1. In the O 1s region, peaks corresponding to SiO_x together with contamination of Li_2CO_3 were observed at 530.2 and 532 eV.[23] After the first lithiation, a broad Li 1s peak was observed at around 55 eV with a weak shoulder at lower binding energy. Curve fitting analysis showed the appearance of Li_ySi, lithium oxide (Li_2O), and Li silicates at 52.7, 54.6, and 56.0 eV, respectively, together with contamination of Li_2CO_3 at around 56 eV.[8, 18, 24, 25] This implies that the Li containing reactive species underwent the side reactions with residual gasses in the vacuum chamber. It is noted that the Li silicates peak cannot be deconvoluted from that of Li_2CO_3 because their peak positions are very close to each other.[8] A peak corresponding to bulk Si shifted to lower binding energy at 96.1 eV, confirming the formation of Li_ySi as a result of the lithiation of bulk a-Si.[8, 18, 25, 26] In addition, the peaks corresponding to various Si oxides merged into a peak at 101.0 eV probably due to the lithiation. Based on the peak position,[18, 26] lithium orthosilicate (Li_4SiO_4) should be the major Li silicate species. It is noted that all the Si 2p peaks became somewhat smaller than those of pristine state because the formation of topmost layer composed of Li_2O, Li_2CO_3, and Li-silicates

interferes photoelectrons ejected from their underneath.

After the first delithiation, the weak shoulder peak corresponding to Li silicide disappeared due to the Li extraction from the Li_ySi in the Li 1s region.[8] In contrast to the disappearance of Li_ySi peak, the Li_2O and Li_2CO_3/Li silicates peaks remained, indicating their very high resistivity. In the Si 2p region, the position of Li silicate peak at 101.0 eV also remained unchanged as highly resistive species. In contrast, the Si 2p peak corresponding to Li_ySi at 96.1 eV shifted to the higher binding energy of 97.0 eV due to the delithiation. However, it did not revert to the original position at 98.7 eV corresponding to the bulk a-Si, confirming that some Li^+ ions were trapped in Li_ySi due to the polarization resistance.[8, 18, 25, 26] In addition to the highly resistive species such as Li_2O, Li_2CO_3 and Li silicates, this is one of the origins of irreversible capacity loss shown in Figure 5-2. In the O 1s region, broad doublet peaks appeared around 527 – 534 eV. The broad peaks were deconvoluted into peaks corresponding to Li_2O, Li_4SiO_4, and Li_2CO_3 at 528.7, 530.1, and 531.5 eV, respectively.[26, 27]

In the second cycle, the Li_ySi re-appeared and disappeared in the Li 1s region, and the Li_ySi peak quasi-reversibly shifted between 95.8 eV and 96.8 eV in the Si 2p region after the lithiation and delithiation, respectively, while the spectral features related to all the highly resistive species such as Li_2O, Li_2CO_3 and Li silicates remained almost unchanged.

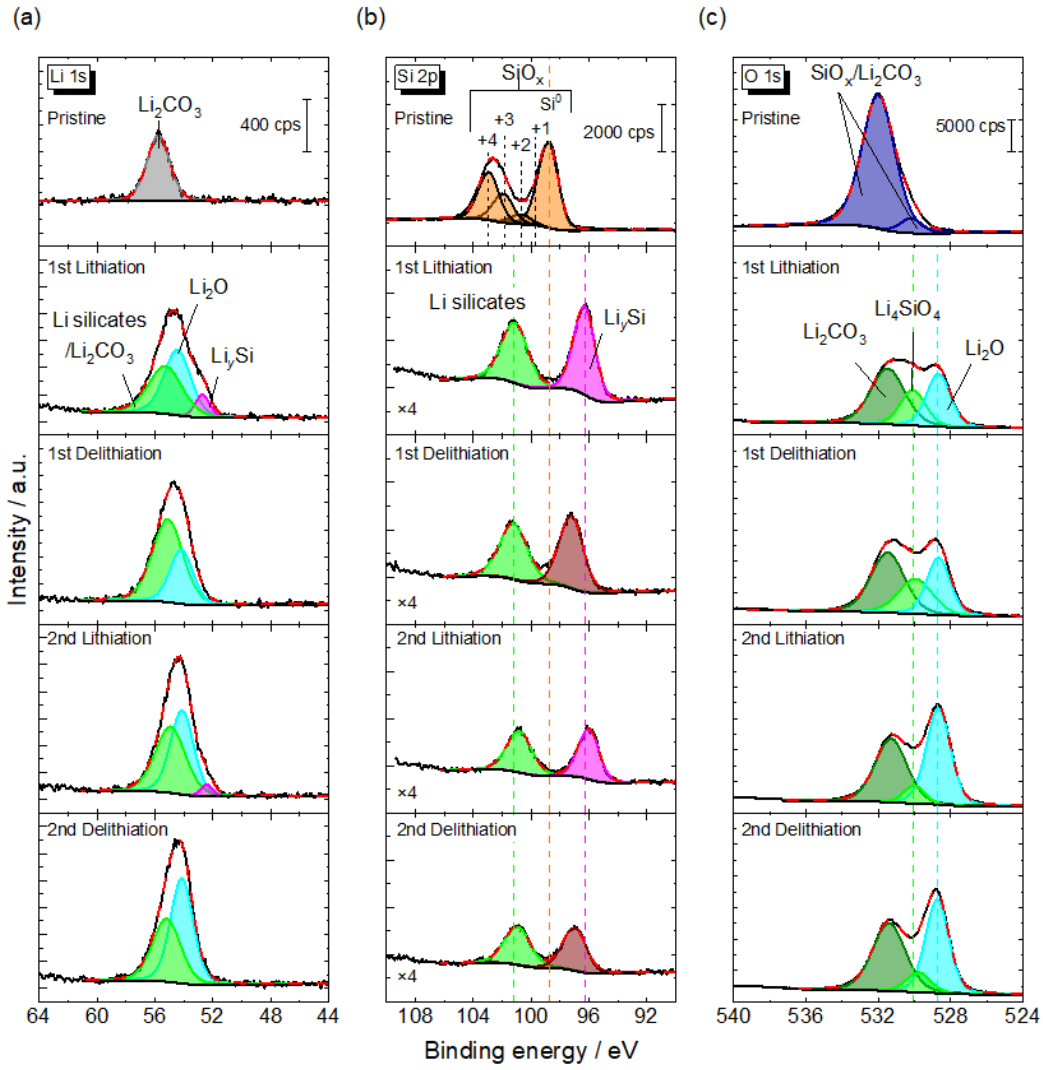

Figure 5-4 (a) Li 1s and O 1s spectra for the $SiO_{0.53}$ thin-film anode in the pristine state, after the first and second lithiation and delithiation. All binding energies were calibrated based on hydrocarbon C 1s peak at 285.0 eV.

5.2.3.2 Dynamic observation

As described in Section 5.2.3.1, Li^+ ions were inserted into the bulk Si and SiO_x to form Li_ySi and Li_4SiO_4 after the lithiation and those were extracted from Li_ySi with maintaining Li_4SiO_4 as irreversible species after the delithiation. To observe the dynamic changes in surface composition, sequential XPS measurements composed of Li 1s, Si 2p, O 1s and C 1s were carried out continuously during lithiation and delithiation.

Figure 5-5 shows the time course photoelectron spectra in the Li 1s and Si 2p regions during the first lithiation and delithiation. As described in Section 5.2.3.1, a peak corresponding to Li_2CO_3 was observed at 55.8 eV in the pristine state. In the Si 2p region, bulk Si (Si^0) and suboxides (SiO_x) peaks were observed at 98.7 and around 99.7 – 102.7 eV.

The peaks in Li 1s and Si 2p regions remained unchanged until the capacity density reached around 1700 mAh g^{-1} corresponding to the Li content $y = 1.7$ in Li_ySi. It is noted that the intensities of all the peaks gradually decreased in this capacity range. This can be attributed to the fluctuation of incident photon flux because any outermost layers yet to be formed at this stage. When the Li content exceeded around $y = 1.8$, new peaks corresponding to Li_ySi suddenly appeared at 52.9 eV in the Li 1s region and at 96.4 eV in the Si 2p region as well as Li silicates peak at 101.5 eV in the Si 2p region. These results

suggest that the lithiation reaction of Si and SiO_x proceeded in a layer-by-layer manner from the bottom side of $SiO_{0.53}$ thin film in contact with the LLZT sheet. In the previous study on electrochemical lithiation/delithiation of a-Si thin film sputter deposited on LLZT,[8] the positions of Li_ySi peaks in the Li 1s and Si 2p regions linearly correlated with the electrochemical charge, i.e., Li content y in Li_ySi and the Si 2p peak reached at 95.4 eV when $Li_{3.50}Si$ was formed. In the present study, however, the two Si 2p peaks due to the a-Si and Li_ySi coexisted in the capacity range from 1750 to 1970 mAh g^{-1} (y = 1.8 – 2.1), and the position of Li_ySi peak was almost constant at around 96.3 eV throughout the entire lithiation process, suggesting that lithiation proceeded grain by grain. According to the linear correlation between the position of Si 2p peak due to the Li_ySi and Li content y in Li_ySi,[8] the resulting Li silicide species should be $Li_{\sim 2.4}Si$. Based on the assumption that all the electrochemical charge was consumed for lithiation of Si, $Li_{3.6}Si$ was formed during the first charging with the capacity density of 3461 mAh/g, and thus 34% of Li^+ ions were consumed for the formation of Li silicates and Li_2O. In fact, a peak corresponding to Li_2O at 54.2 eV became more obvious when the Li content exceeded around y = 2.1 and its intensity increased with increase in capacity density, i.e., Li content. It is noted that Li_2O was formed not only by the lithiation of $SiO_{0.53}$ but also due to the side reactions of Li_ySi with residual gasses in the vacuum chamber. Once crystalline

$Li_{3.75}Si$ (c-$Li_{3.75}Si$) forms during the lithiation up to 3579 mAh/g, phase transformation from c-$Li_{3.75}Si$ to a-Li_ySi occurs during the successive delithiation, resulting in severe capacity fading due to the significant volume change.[8, 10, 11] In the case of $SiO_{0.53}$, however, the formation of c-$Li_{3.75}Si$ was effectively suppressed by trapping Li^+ ions in Li silicates and Li_2O, leading to the superior cycle performance. One may consider that, even though 34 % of Li^+ ions are consumed for Li_2O and Li silicides, lithiation can proceed until the formation of c-$Li_{3.75}Si$ by using extra electrochemical charge. This process was prohibited probably due to the high ionic and/or electronic resistivity of the matrix composed of Li_2CO_3, Li_2O and Li silicates.

During the subsequent delithiation, the intensity of Li_ySi peak at 52.7 eV gradually decreased, and eventually disappeared. Simultaneously, the Li_ySi peak monotonically shifted to higher binding energies with a slope of 0.73 eV/y (Li content y = 3.5 – 2.2) in the Si 2p region. This is clearly different from the delithiation behavior of a fully-lithiated Si thin-film which includes phase transformation from c-$Li_{3.75}Si$ to a-Li_ySi but similar to the monotonic shift of Li_ySi peak throughout the delithiation after the lithiation up to $Li_{2.3}Si$.[8] This observation is indeed consistent with the absence of peak due to the formation of c-$Li_{3.75}Si$ in the *dQ/dV* peaks of Figure 5-3.[8, 11, 20, 28] Kitada et al. previously reported that the c-$Li_{3.75}Si$ did not form in amorphous SiO by the lithiation up to 0 V.[7]

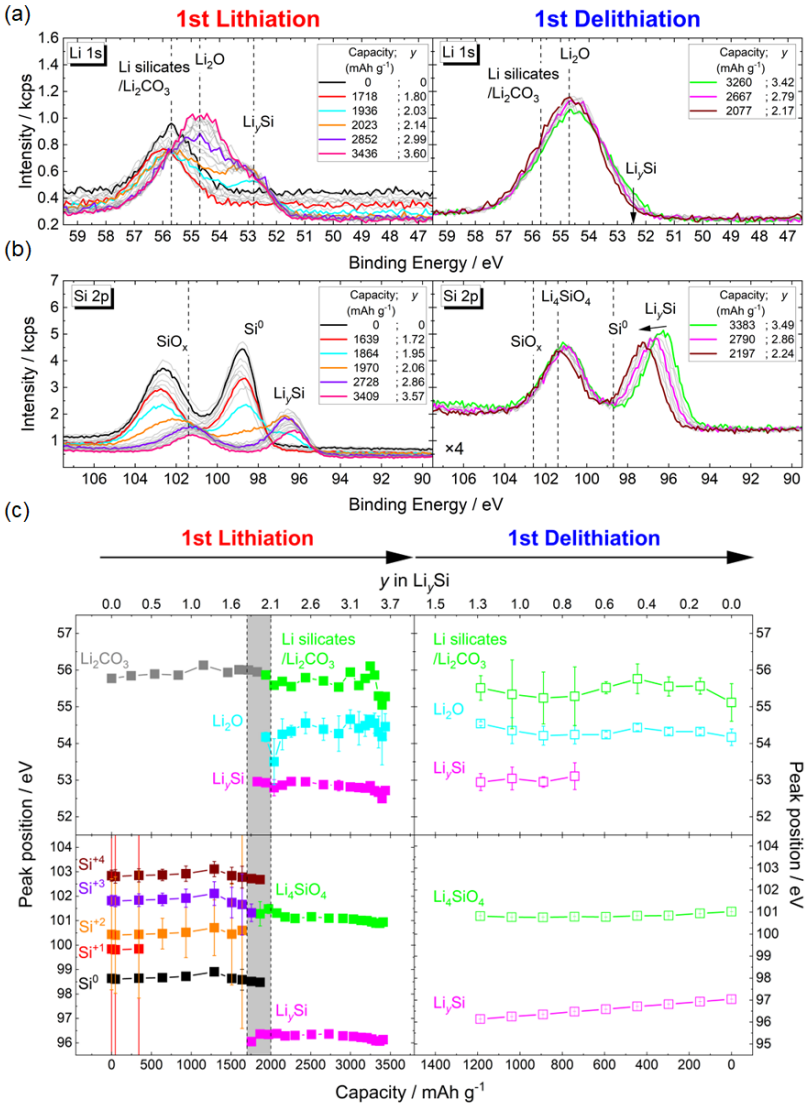

Figure 5-5 (a) Li 1s and (b) Si 2p photoelectron spectra generated during 1st lithiation and delithiation in a potential range of 0.02 – 1.5 V *vs.* Li^+/Li. (c) Position of Li 1s peaks corresponding to Li_2O, Li silicates/Li_2CO_3, and Li silicides (Li_ySi) Si 2p peaks corresponding to Si^0/Li_ySi, suboxide (SiO_x) composed of Si^{+1}, Si^{+2}, Si^{+3}, and Si^{+4} components, and Li_4SiO_4 plotted as functions of capacity. Gray area represents region where a-Si and a-Li_ySi coexisted in the first lithiation.

In the second cycle, the Li_ySi peak re-appeared and disappeared in the Li 1s region and reversibly shifted to lower and higher binding energies in Si 2p region during the lithiation and delithiation, respectively, while the highly resistive species including the Li_2O and Li silicates peaks remained unchanged, confirming the reversible lithiation/delithiation processes, as shown in Figure 5-6.

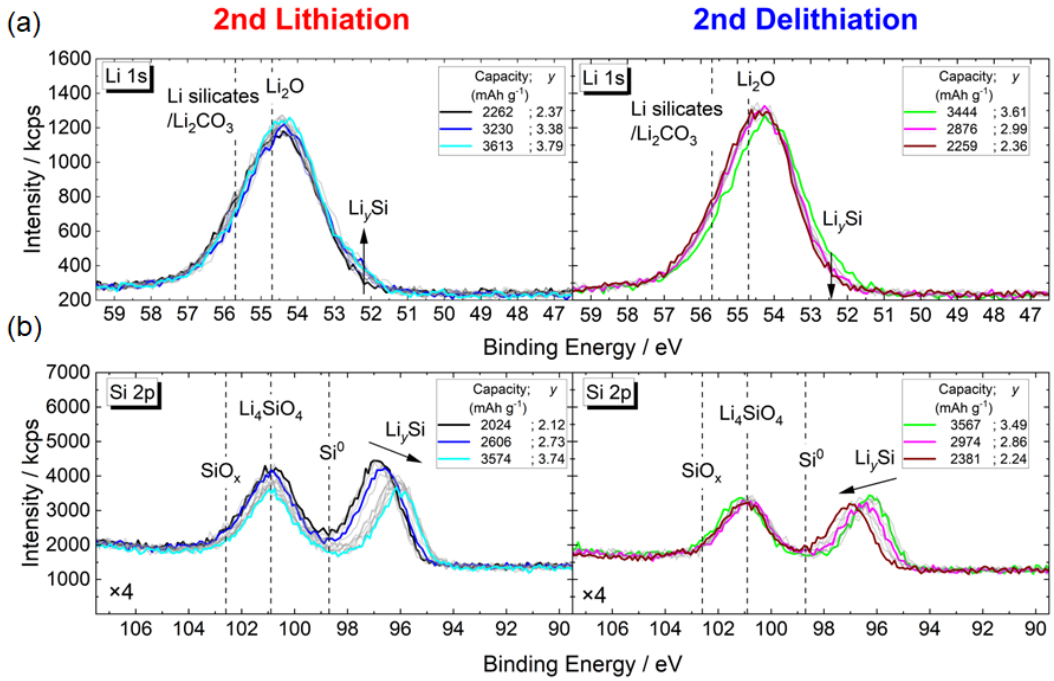

Figure 5-6 (a) Li 1s and (b) Si 2p photoelectron spectra generated during 2nd lithiation and delithiation in a potential range of 0.02 – 1.5 V *vs.* Li^+/Li.

5.3 Conclusions

In conclusion, the first and second lithiation/delithiation processes of a $SiO_{0.53}$ electrode in a thin-film-cell configuration were investigated using an *in-situ* XPS. In the first cycle, the formation of irreversible species such as Li_2CO_3, Li silicates (Li_4SiO_4), and Li_2O, as well as reversible Li_ySi were observed, as shown in Figure 5-4 and Figure 5-5. The Li content y in the Li_ySi was estimated to be $Li_{\sim 2.4}Si$ by the linear correlation between the position of Si 2p peak due to the Li_ySi and Li content y in Li_ySi. This limited amount of Li^+ ions insertion into Si due to the trapping Li^+ ions in Li_4SiO_4 and Li_2O suppresses the formation of c-$Li_{3.75}Si$ during lithiation and phase transformation from c-$Li_{3.75}Si$ to a-Li_ySi during the successive delithiation, leading to improvement of cycle performance of SiO_x thin-film anodes. In the second cycle, reversible shift of Si 2p peak corresponding to Li_ySi were observed while the peaks of irreversible species remained unchanged.

References

(1) Miyazaki, R.; Ohta, N.; Ohnishi, T.; Takada, K. Anode properties of silicon-rich amorphous silicon suboxide films in all-solid-state lithium batteries. *J. Power Sources* **2016**, *329*, 41-49. DOI: 10.1016/j.jpowsour.2016.08.070.

(2) Haruta, M.; Doi, T.; Inaba, M. Oxygen-Content Dependence of Cycle Performance and Morphology Changes in Amorphous-SiO_x Thin-Film Negative Electrodes for Lithium-Ion Batteries. *J. Electrochem. Soc.* **2019**, *166* (2), A258-A263. DOI: 10.1149/2.0861902jes.

(3) Li, H.; Li, H.; Yang, Z.; Yang, L.; Gong, J.; Liu, Y.; Wang, G.; Zheng, Z.; Zhong, B.; Song, Y.; et al. SiO_x Anode: From Fundamental Mechanism toward Industrial Application. *Small* **2021**, *17* (51), e2102641. DOI: 10.1002/smll.202102641 From NLM PubMed-not-MEDLINE.

(4) Chen, T.; Wu, J.; Zhang, Q.; Su, X. Recent advancement of SiO_x based anodes for lithium-ion batteries. *J. Power Sources* **2017**, *363*, 126-144. DOI: 10.1016/j.jpowsour.2017.07.073.

(5) Kim, T.; Park, S.; Oh, S. M. Solid-State NMR and Electrochemical Dilatometry Studyon Li^+Uptake Extraction Mechanism in SiO Electrode. *J. Electrochem. Soc.* **2007**, *154*. DOI: 10.1149/1.2790282.

(6) Takezawa, H.; Ito, S.; Yoshizawa, H.; Abe, T. Structural stabilization on SiO_x film anode with large areal capacity for enhanced cyclability in lithium-ion batteries. *J. Power Sources* **2016**, *324*, 45-51. DOI: 10.1016/j.jpowsour.2016.05.061.

(7) Kitada, K.; Pecher, O.; Magusin, P.; Groh, M. F.; Weatherup, R. S.; Grey, C. P. Unraveling the Reaction Mechanisms of SiO Anodes for Li-Ion Batteries by Combining in Situ ^{7}Li and ex Situ ^{7}Li/^{29}Si Solid-State NMR Spectroscopy. *J. Am.*

Chem. Soc. **2019**, *141* (17), 7014-7027. DOI: 10.1021/jacs.9b01589 From NLM PubMed-not-MEDLINE.

(8) Endo, R.; Ohnishi, T.; Takada, K.; Masuda, T. Electrochemical Lithiation and Delithiation in Amorphous Si Thin Film Electrodes Studied by Operando X-ray Photoelectron Spectroscopy. *J. Phys. Chem. Lett* **2022**, *13* (31), 7363-7370. DOI: 10.1021/acs.jpclett.2c01312 From NLM PubMed-not-MEDLINE.

(9) Putra, R. P.; Matsushita, K.; Ohnishi, T.; Masuda, T. Operando Nanomechanical Mapping of Amorphous Silicon Thin Film Electrodes in All-Solid-State Lithium-Ion Battery Configuration during Electrochemical Lithiation and Delithiation. *J Phys Chem Lett* **2024**, *15* (2), 490-498. DOI: 10.1021/acs.jpclett.3c03012 From NLM PubMed-not-MEDLINE.

(10) Rohrer, J.; Albe, K. Insights into Degradation of Si Anodes from First-Principle Calculations. *The Journal of Physical Chemistry C* **2013**, *117* (37), 18796-18803. DOI: 10.1021/jp401379d.

(11) Obrovacz, M. N.; Christensen, L. Structural Changes in Silicon Anodes during Lithium Insertion/Extraction. *Electrochem. Solid-State Lett.* **2004**, *7*, A93-A96. DOI: 10.1149/1.1652421.

(12) Obrovac, M. N.; Krause, L. J. Reversible Cycling of Crystalline Silicon Powder. *J. Electrochem. Soc.* **2007**, *154*, A103-A108. DOI: 10.1149/1.2402112.

(13) Avci, R.; Davis, B. H.; Wolfenden, M. L.; Kellerman, L. R.; Lucas, K.; Martin, J.; Deliorman, M. A practical method for determining pit depths using X-ray attenuation in EDX spectra. *Corros. Sci.* **2015**, *93*, 9-18. DOI: 10.1016/j.corsci.2014.12.018.

(14) Nguyen, C. C.; Choi, H.; Song, S.-W. Roles of Oxygen and Interfacial Stabilization

in Enhancing the Cycling Ability of Silicon Oxide Anodes for Rechargeable Lithium Batteries. *J. Electrochem. Soc.* **2013**, *160* (6), A906-A914. DOI: 10.1149/2.118306jes.

(15) Bell, F. G.; Ley, L. Photoemission study of $SiO_x(0\leq x\leq 2)$ alloys. *Physical Review B* **1988**, *37* (14), 8383-8393. DOI: 10.1103/physrevb.37.8383.

(16) Maeanchi, J. P.; Hepp, A. F.; Kumta, P. N. High Capacity, Reversible Silicon Thin-Film Anodes. *Electrochem. Solid-State Lett.* **2003**, *6*, A198. DOI: 10.1149/1.1596918.

(17) Ohara, S.; Suzuki, J.; Sekine, K.; Takamura, T. A thin film silicon anode for Li-ion batteries having a very large specific capacity and long cycle life. *J. Power Sources* **2004**, *136* (2), 303-306. DOI: 10.1016/j.jpowsour.2004.03.014.

(18) Endo, R.; Ohnishi, T.; Takada, K.; Masuda, T. In Situ Observation of Lithiation and Delithiation Reactions of a Silicon Thin Film Electrode for All-Solid-State Lithium-Ion Batteries by X-ray Photoelectron Spectroscopy. *J. Phys. Chem. Lett* **2020**, *11* (16), 6649-6654. DOI: 10.1021/acs.jpclett.0c01906 From NLM PubMed-not-MEDLINE.

(19) Chan, C. K.; Ruffo, R.; Hong, S. S.; Huggins, R. A.; Cui, Y. Structural and electrochemical study of the reaction of lithium with silicon nanowires. *J. Power Sources* **2009**, *189* (1), 34-39. DOI: 10.1016/j.jpowsour.2008.12.047.

(20) Loveridge, M. J.; Lain, M. J.; Johnson, I. D.; Roberts, A.; Beattie, S. D.; Dashwood, R.; Darr, J. A.; Bhagat, R. Towards High Capacity Li-ion Batteries Based on Silicon-Graphene Composite Anodes and Sub-micron V-doped $LiFePO_4$ Cathodes. *Sci Rep* **2016**, *6*, 37787. DOI: 10.1038/srep37787 From NLM PubMed-not-MEDLINE.

(21) Ogata, K.; Salager, E.; Kerr, C. J.; Fraser, A. E.; Ducati, C.; Morris, A. J.; Hofmann, S.; Grey, C. P. Revealing lithium-silicide phase transformations in nano-structured silicon-based lithium ion batteries via in situ NMR spectroscopy. *Nat Commun* **2014**, *5*, 3217. DOI: 10.1038/ncomms4217 From NLM PubMed-not-MEDLINE.

(22) Choi, G.; Kim, J.; Kang, B. Understanding Limited Reversible Capacity of a SiO Electrode during the First Cycle and Its Effect on Initial Coulombic Efficiency. *Chem. Mater.* **2019**, *31* (16), 6097-6104. DOI: 10.1021/acs.chemmater.9b01057.

(23) Takezawa, H.; Iwamoto, K.; Ito, S.; Yoshizawa, H. Electrochemical behaviors of nonstoichiometric silicon suboxides (SiO_x) film prepared by reactive evaporation for lithium rechargeable batteries. *J. Power Sources* **2013**, *244*, 149-157. DOI: 10.1016/j.jpowsour.2013.02.077.

(24) Cho, J. H.; Xiao, X.; Verbrugge, M. W.; Sheldon, B. W. Influence of Oxygen Content on the Structural Evolution of SiO_x Thin-Film Electrodes with Subsequent Lithiation/Delithiation Cycles. *ACS Applied Energy Materials* **2022**, *5* (11), 13293-13306. DOI: 10.1021/acsaem.2c01903.

(25) Endo, R.; Ohnishi, T.; Takada, K.; Masuda, T. Instrumentation for tracking electrochemical reactions by x-ray photoelectron spectroscopy under conventional vacuum conditions. *Journal of Physics Communications* **2021**, *5* (1), 015001. DOI: 10.1088/2399-6528/abd617.

(26) Philippe, B.; Dedryvère, R.; Allouche, J.; Lindgren, F.; Gorgoi, M.; Rensmo, H.; Gonbeau, D.; Edström, K. Nanosilicon Electrodes for Lithium-Ion Batteries: Interfacial Mechanisms Studied by Hard and Soft X-ray Photoelectron Spectroscopy. *Chem. Mater.* **2012**, *24* (6), 1107-1115. DOI: 10.1021/cm2034195.

(27) Miyachi, M.; Yamamoto, H.; Kawai, H.; Ohta, T.; Shirakata, M. Analysis of SiO Anodes for Lithium-Ion Batteries. *J. Electrochem. Soc.* **2005**, *152*, A2089-A2091. DOI: 10.1149/1.2013210.

(28) Key, B.; Morcrette, M.; Tarascon, J.-M.; Grey, C. P. Pair Distribution Function Analysis and Solid State NMR Studies of Silicon Electrodes for Lithium Ion Batteries: Understanding the (De)lithiation Mechanisms. *Journal of the American Chemical Society* **2010**, *133*, 503-512. DOI: 10.1021/ja108085d.

6. General conclusion

In this study, the electrochemical reactions of $LiCoO_2$-Li_3BO_3 (LCO-LBO) composite cathode, and lithiation and delithiation processes of amorphous SiO_x thin-film anode constructed on solid electrolytes were investigated mainly using *operando* hard x-ray photoelectron spectroscopy (HAXPES) and *in-situ* x-ray photoelectron spectroscopy (XPS), respectively, for application to high-performance all-solid-state lithium-ion batteries cathode and anode materials.

In Chapter 2, the fabrication process of LCO-LBO composite cathode and amorphous SiO_x thin-film anode with all-solid-state cell configuration, and the principles of the characterization techniques were described.

In Chapter 3, a laboratory-based HAXPES apparatus enabling bias application to a sample kept in vacuum conditions and angle-resolved measurements was presented. Then, demonstrations for confirming those functions using Au film and Si substrate with its oxide layer were performed.

In Chapter 4, oxidation and electronic state changes of LCO in LCO-LBO composite cathode during charge/discharge cycles were observed with stepwisely expanding the positive potential limit from 4.2 to 4.7 V vs. Li^+/Li using *operando* HAXPES system

shown in Chapter 3 for clarification of the electrochemical reactions of LCO including undesired irreversible processes. In the first charging, downshift of $Co2p_{3/2}$ peak corresponding to the change in valence state of LCO due to the transition from a p-type semiconducting to a metallic state induced by delithiation were observed. In a potential range of 3.0 – 4.4 V, Co^{3+} ions were oxidized to Co^{4+} after charging, and the oxidized Co^{4+} were reversibly reduced to Co^{3+} ions after discharging. This reversible redox reaction of Co ions in LCO were evidenced by the reversible increase/decrease of the full width half maximum (FWHM) of Co^{4+} ions after the charging/discharging, respectively. When the positive potential limit exceeded 4.5 V or higher, the Co^{3+} ions were irreversibly oxidized to Co^{4+}. On the other hand, in a potential range of 3.0 – 4.5 V, the decrease of energy gap between the Fermi level of LCO and energy levels of O^{2-} anions in LCO and/or the increase of screening effect of O^{2-} anions after the charging was suggested by the O^{2-} peak shift to a lower binding energy. The O^{2-} peak reversibly shifted to a higher binding energy after the discharging. When the positive potential limit for charging was extended to 4.7 V, the O^{2-} anions were irreversibly oxidized to electron deficient oxygen dimer $(O_2)^{n-}$. Those irreversible oxidation of Co^{4+} and O^{2-} ions under high-voltage cycling leads to structural disorder and O_2 gas release from LCO cathode, resulting in capacity fading.

In Chapter 5, compositional change of $SiO_{0.53}$ thin-film anode during lithiation/delithiation processes were dynamically observed using *in-situ* XPS. The charge integrations in the first lithiation and delithiation were around 3460 mAh g^{-1} and 1500 mAh g^{-1}, respectively, with a Coulombic efficiency of 43.9%, which was much smaller than pure Si. After the first lithiation, irreversible species such as Li_2O, Li_2CO_3, and lithium silicates (Li silicates) formed in addition to reversible lithium silicide (Li_ySi). According to the quantitative analysis conducted using charge densities and XPS, 34% of Li^+ ions were consumed for the formation of such irreversible species, leading to the irreversible capacity loss. In the dynamic observation, $SiO_{0.53}$ peak remained unchanged until the capacity density reached around 1700 mAh g^{-1} in the first lithiation. When the capacity density exceeded 1750 mAh g^{-1}, Li_ySi, Li silicates, and Li_2O appeared simultaneously. In the capacity range from 1750 to 1970 mAh g^{-1}, $SiO_{0.53}$, Li_ySi, Li silicates, Li_2O coexisted. When the capacity density exceeded 2000 mAh g^{-1}, $SiO_{0.53}$ disappeared. The lithiation reaction of SiO_x proceeded in a layer-by-layer manner from the bottom side of $SiO_{0.53}$ thin film in contact with the LLZT, although uniform lithiation took place in amorphous Si thin film sputtered deposited on a LLZT, According to the linear correlation between the position of Si 2p peak due to the Li_ySi and Li content y in Li_ySi,[1] the resulting Li silicide species should be $Li_{\sim 2.4}Si$.

This limited lithiation into SiO_x due to the trapping Li^+ ions in Li silicates and Li_2O suppresses the formation of crystalline $Li_{3.75}Si$ (c-$Li_{3.75}Si$) during lithiation and phase transformation from c-$Li_{3.75}Si$ to a-Li_ySi during the successive delithiation, which result in capacity fading due to the severe volume change, leading to the superior cycle performance.

6.1 Future research prospects

6.1.1 Toward improving performance of $LiCoO_2$ cathodes under high-voltage operations

Based on the foregoing conclusions, the following guidelines are proposed for overcoming the challenge of LCO cathodes, i.e., irreversible oxidation of O^{2-} anions. O^{2-} anions were irreversibly oxidized to the electron deficient oxygen dimer $(O_2)^{n-}$ under high-voltage charging because upshift of energy level of O^{2-} anions including O 2p band induced by stronger hybridization between Co 3d states and O 2p band, leading to release of O_2 gas,[2] and capacity fading. One approach to suppress the irreversible oxidation is to enlarge the energy gap between Co 3d states and O 2p band by elemental doping with stronger electronegativity than O.[2]

6.1.2 Toward improving performance of SiO_x anodes

Based on the foregoing conclusions, the following guidelines are proposed for overcoming the challenge of SiO_x anodes, i.e., the large irreversible capacity loss in the initial cycle compared with pure Si. In the first lithiation, Li^+ ions are consumed for the formation of irreversible species such as Li_2CO_3, Li silicates, and Li_2O, as well as reversible lithium silicides (Li_ySi). In the present study using $SiO_{0.53}$ thin film, $Li_{\sim 2.4}Si$ was formed, and 34% of Li^+ ions were consumed for the formation of such irreversible

species. On the other hand, this limited amount of Li^+ ions insertion into Si due to the trapping Li^+ ions in Li_4SiO_4 and Li_2O suppresses the formation of crystalline $Li_{3.75}Si$ (c-$Li_{3.75}Si$) during lithiation and phase transformation from c-$Li_{3.75}Si$ to a-Li_ySi during the successive delithiation, leading to improvement of cycle performance of SiO_x thin-film anodes. Therefore, controlling the number of oxygen species is quite important for the compatibility of high-capacity density and superior cycle performance.

6.1.3 *Operando* HAXPES measurements

The developed *operando* HAXPES system is suitable for highly reactive battery materials because it enables us to perform chemical analysis under operating conditions without disassembling batteries. That system enables us to observe deeper region including interface between electrode/electrolyte in thin-film cell, but also to obtain depth profile including electrolyte, its interface with electrode, and electrode during battery operation, which are the major bottleneck impeding the development of all-solid-state batteries.[3, 4]

Reference

(1) Endo, R.; Ohnishi, T.; Takada, K.; Masuda, T. Electrochemical Lithiation and Delithiation in Amorphous Si Thin Film Electrodes Studied by Operando X-ray Photoelectron Spectroscopy. *J. Phys. Chem. Lett* **2022**, *13* (31), 7363-7370. DOI: 10.1021/acs.jpclett.2c01312 From NLM PubMed-not-MEDLINE.

(2) Kong, W.; Zhang, J.; Wong, D.; Yang, W.; Yang, J.; Schulz, C.; Liu, X. Tailoring Co3d and O2p Band Centers to Inhibit Oxygen Escape for Stable 4.6 V $LiCoO_2$ Cathodes. *Angew. Chem. Int. Ed. Engl.* **2021**, *60* (52), 27102-27112. DOI: 10.1002/anie.202112508 From NLM PubMed-not-MEDLINE.

(3) Yamamoto, K.; Iriyama, Y.; Hirayama, T. Visualization of Electrochemical Reactions in All-Solid-State Li-Ion Batteries by Spatially Resolved Electron Energy-Loss Spectroscopy and Electron Holography. *Materials Transactions* **2015**, *56* (5), 617-624. DOI: 10.2320/matertrans.M2015014.

(4) Haruyama, J.; Sodeyama, K.; Han, L.; Takada, K.; Tateyama, Y. Space–Charge Layer Effect at Interface between Oxide Cathode and Sulfide Electrolyte in All-Solid-State Lithium-Ion Battery. *Chem. Mater.* **2014**, *26* (14), 4248-4255. DOI: 10.1021/cm5016959.

Acknowledgements

本論文は、北海道大学大学院総合化学院、博士後期課程在籍中に増田卓也教授のもとで行った研究内容により構成されています。増田卓也教授には、本論文作成はもとより、研究や実験の指針、データの解釈、投稿論文の執筆に至るまで、ご指導ご鞭撻を賜りました。加えて、国内だけでなく国際学会で研究成果を発表する機会を幾度も頂きました。また、研究以外の私生活においても多大なるご支援ご配慮頂きましたことを、心より御礼申し上げます。

ご多用の中、本論文の審査をして頂いただけでなく、博士後期課程の中間報告会、予備審査、本審査において貴重なご助言を賜りました主査の村越敬教授、副査の忠永清治教授、山浦一成教授、白幡直人教授に、心より御礼申し上げます。

充放電下における電池試料の電気化学反応を観察するための充放電オペランド硬X線光電子分光装置を開発するにあたって、私の要望に最大限応えてくださったシエンタオミクロン株式会社、バキュームプロダクツ株式会社、アルバック・ファイ株式会社、株式会社松浦製作所のスタッフの方々に心より感謝申し上げます。

コバルト酸リチウム（$LiCoO_2$）の電極反応の観察を行うにあたって、共同研究を快く引き受けてくださり、試料作製・評価および投稿論文について貴重なご助言を賜りました、物質・材料研究機構、エネルギー・環境材料研究センターの大西剛博士に心より

感謝申し上げます。

シリコン酸化物（SiO_x）薄膜電池試料の特性評価を行うにあたり、試料をご提供頂き、貴重なご意見を賜りました、同志社大学理工学部の土井貴之教授に深く感謝申し上げます。

電池試料の分析・評価のためにNIMS蓄電池基盤プラットフォームの機器を使用させて頂くにあたり、丁寧に技術的なご指導をしてくださった支援スタッフの方々に感謝申し上げます。

最後に、今日に至るまでの長い間、円滑に研究を行うことができるよう経済的、精神的に支援してくださり、いつも私を信頼して温かく見守ってくださった両親に対して、心より御礼申し上げます。

2025年3月　岩間　司